DESIGN OF A COMPUTERIZED DYNAMIC POSTUROGRAPHY MACHINE

A THESIS SUBMITTED TO
THE GRADUATE SCHOOL OF NATURAL AND APPLIED SCIENCES
OF
MIDDLE EAST TECHNICAL UNIVERSITY

AHMET UFUK ÇUVALCI

IN PARTIAL FULFILLMENT OF THE REQUIREMENTS
FOR
THE DEGREE OF MASTER OF SCIENCE
IN
MECHANICAL ENGINEERING

NOVEMBER 2019

Approval of the thesis:

DESIGN OF A COMPUTERIZED DYNAMIC POSTUROGRAPHY MACHINE

submitted by **AHMET UFUK ÇUVALCI** in partial fulfillment of the requirements for the degree of **Master of Science in Mechanical Engineering Department, Middle East Technical University** by,

Prof. Dr. Halil Kalıpçılar _____
Dean, Graduate School of **Natural and Applied Sciences**

Prof. Dr. M. A. Sahir Arıkan _____
Head of Department, **Mechanical Engineering**

Assoc. Prof. Dr. Ergin Tönük
Supervisor, **Mechanical Engineering Department, METU** _____

Examining Committee Members:

Prof. Dr. Zafer Dursunkaya
Mechanical Engineering Department, METU _____

Assoc. Prof. Dr. Ergin Tönük
Mechanical Engineering Department, METU _____

Assoc. Prof. Dr. M. Bülent Özer
Mechanical Engineering Department, METU _____

Assist. Prof. Dr. Bilsay Sümer
Mechanical Engineering Department, Hacettepe University _____

Assist. Prof. Dr. Ali Emre Turgut
Mechanical Engineering Department, METU _____

Date: _____

I hereby declare that all information in this document has been obtained and presented in accordance with academic rules and ethical conduct. I also declare that, as required by these rules and conduct, I have fully cited and referenced all material and results that are not original to this work.

Name, Last Name: AHMET UFUK ÇUVALCI

Signature :

ABSTRACT

DESIGN OF A COMPUTERIZED DYNAMIC POSTUROGRAPHY MACHINE

Çuvalcı, Ahmet Ufuk
M.S., Department of Mechanical Engineering
Supervisor : Assoc. Prof. Dr. Ergin Tönük

November 2019, 171 pages

The need of the objectivity in medical diagnostics is a common problem. The developments in sensor electronics and software packages besides the theoretical progress in understanding human physiology or anatomy at all opens new gates for measurements of human systems. Relation between human sensory input and motor control to certain stimulations was unveiled in the past. Based on this fact a method to diagnose human balance disorders was developed, named Computerized Dynamic Posturography (CDP). Statistically classifying the reason of balance disorder, this method reduces the amount of time and effort in diagnostics. Moreover, having objective data at the end, it is also possible to compare the patient's past and present balance score to observe his/her progress. All that is done by so called CDP-Device. In this study a new-third motion axis to the standard 2-axis CDP-device was presented, which is a new contribution to literature. Moreover, the design, production and the preliminary tests of a multiaxis force plate which is also alone a whole product was studied. On the

whole, a new medical product was developed having national, economic and research value.

Keywords: Balance, Concussion, Dynamic, Posture, Posturography, Computer, Human, Disorder, Device, Force Plate, Mechanism, Design, Loadcell, Transducer, Crosstalk

ÖZ

BİLGİSAYARLI DİNAMİK POSTÜROGRAFİ CİHAZI TASARIMI

Çuvalcı, Ahmet Ufuk
Yüksek Lisans, Makina Mühendisliği Bölümü
Tez Yöneticisi : Doç. Dr. Ergin Tönük

Kasım 2019 , 171 sayfa

Medikal alanda tanılama sırasında nesnellik yaygın bir ihtiyaç olarak durmaktadır. Elektronik sistemler, sensörler ve yazılım alanındaki gelişmelerin yanında, insan fizyolojisi ve anatomisinin anlaşılmasındaki teorik ilerleme, insan üzerinde ölçüm yapılmasına yeni olanaklar sunmaktadır. Geçmişte, belli uyaranlara karşı duyusal girdilerle motor kontrol arasında doğrudan bir ilişkinin olduğu açığa çıkarılmıştır. Buna dayanarak, insanda denge hastalıklarının tanısında Bilgisayarlı Dinamik Postürografi (BDP) isminde bir yöntem geliştirilmiştir. Bu metot istatistiksel olarak denge hastalığını sınıflandırarak, tanılama sırasında harcanan zamanı ve eforu önemli ölçüde düşürmektedir. Ayrıca, uygulama sonunda elde edilen objektif verilerle, geçmişteki ve mevcut denge skoruna bakılarak hastaların gelişimi hakkında karşılaştırma yapılabilmektedir. Tüm bunlar BDP-Cihazı ile gerçekleştirilmektedir. Bu çalışmada, standart 2-eksenli BDP-cihazına ek olarak literatürde bulunmayan üçüncü yeni bir hareket ekseni tasarımı da yapılmıştır. Ayrıca kendi başına ayrı bir ürün olan çok eksenli bir kuvvetölçer yüzey tasarımı,

üretimi ve ilk denemeleri gerçekleştirilmiştir. Genel olarak, ulusal, ekonomik ve araştırma değerleri olan yeni bir medikal ürün geliştirilmiştir.

Anahtar Kelimeler: Denge, Sarsıntı, Dinamik, Postür, Bilgisayar, İnsan, Hastalık, Cihaz, Kuvvetölçer Yüzey, Mekanizma, Tasarım, Yük Hücresi, Sensör, Çapraz Duyarlık

for my father

ACKNOWLEDGMENTS

I would like to express to my supervisor Dr. Ergin Tönük my deepest, sincere gratitude for his long-term guidance, advice, criticism, encouragement and insight throughout this study.

I would also like to express my greatest thanks to LİMATEK Inc., focued on this project and build a nice team. Here I would thank Garip Utku Demir, Emin Şen and Ezgi Sümbül for their contribution and friendship throughout this work.

I would also thank to Dr. Bilsay Sümer and his team for their support by applying the transducer class strain gages.

I owe special thanks to my dearest wife E. Selin for her kind support and presence in all phases of my life.

Finally, I am deeply thankful to my family, my brother M. Onur, my mother Serpil and my father Hasan Ali Çuvalcı for their constant love and compassion throughout my life.

This project was supported by KOSGEB-1239 and TÜBİTAK-1507 7150668 as research, development and innovation programs.

TABLE OF CONTENTS

LIST OF TABLES

TABLES

LIST OF FIGURES

FIGURES

LIST OF ABBREVIATIONS

ADT	Adaptation Test
AP	Anterior-Posterior
BDP	Bilgisayarlı Dinamik Postürografi
CDP	Computerized Dynamic Posturography
CoP	Center of Pressure
cm	centimeter
in	inch
FEA	Finite Element Analysis
FL	Forward-Left
FR	Forward-Right
GUI	Graphical User Interface
kg	kilogram
LoS	Limits of Stability
MCT	Motor Control Test
ML	Medial-Lateral
mm	millimeter
ms	millisecond
MPa	Mega Pascal
N	Newton
N.m	Newton-meter
PD	Parkinson's Disease
RL	Rear-Left
RR	Rear-Right
rpm	revolution per minute
RWS	Rhythmic Weight Shift
WBS	Weight Bearing Squat
SOT	Sensory Organization Test
TM	Trademark

CHAPTER 1

INTRODUCTION

1.1 Human Posture

Studies on human posture are not rare, indeed it has a very long history. Still, giving a clear definition is difficult because posture mechanisms are not understood all with its comprehension, yet. Beginning with the ancient Greek, interest on human posture can be seen in drawings, where human figures are standing in a stable manner in the gravity field. In 17th century, with the foundation of biomechanics, after studies of Giovanni Alfonso Borelli (1608-1679), posture began to be observed in a mechanical point of view. Till 20th century it had not gone beyond the mechanical expression that the projection of the center of mass has to be within the support area. In 20th century, together with the involvement of other disciplines, different theories started to evolve. Creatures with external skeletons and vertrebrates having internal skeletons were compared, stressing the importance of the evolution of central nervous system[18]. Here, any voluntery action was related to posture and the type of the skeleton gave information about the postural control problem. Posture discussions face with the problem that how to distinguish the control mechanism of posture-stabilization system between voluntary movement and the response to external perturbations. For animals with external skeletons there is not much to discuss on, as their postural control include minimal neural effort and are already stable when they are on their legs. Whereas in the internal skeleton example a continuity in the muscle activity is required for keeping stability. After 1950s, Von Holst and Mittelstaedt proposed that there is no posture-stabilizing mechanism responding to voluntery

actions, but only to external perturbations[19]. In 1960s, Feldman introduced the equilibrium-point hypothesis which investigates posture and movement as different peripheral results of the single neurophysiological process was asserted [19]. Eventually, there are two main hypothesis in field that are being recognised. One approach is being studied in engineering field, where vertical posture is modeled as an inverted pendulum and classical mechanics and control theories are used for the solution of the stabilization problem. The second one is related to the equilibrium-point hypothesis where postural operations are assumed to be controlled specifying referent body configurations.

In brief, there is no exact agreement on the definition of posture, more research on human body is still required to understand and define the phenomenon. Nevertheless, two major terms come to light, which are joint configuration and stability. According to the joint configuration definition, posture is considered as a component of body position, besides body location and orientation. Other studies on human movement; on the other hand, give a broader meaning to posture. Going beyond joint configuration, body orientation, maintaining the state for a certain time, resistance to external perturbations are included[20].

One big term to be remembered related to posture is "Postural Sway". It is not possible to stand like a statue, so it can be defined as small displacements of the center of mass of the body within support area when standing quietly. There are two main opinions about the existance of postural sway. First is evaluated as noise of the neoromotor system or imperfection of human body (Peterka et al., 2011) whereas the second view considers it as a natural result of the physiological system of the design of the human body [19]. Postural sway is analyzed in two modes, the directions which are defining the modes are Anterior-Posterior (AP) Sway and Medio-lateral (ML) Sway presented in Figure 1.1.

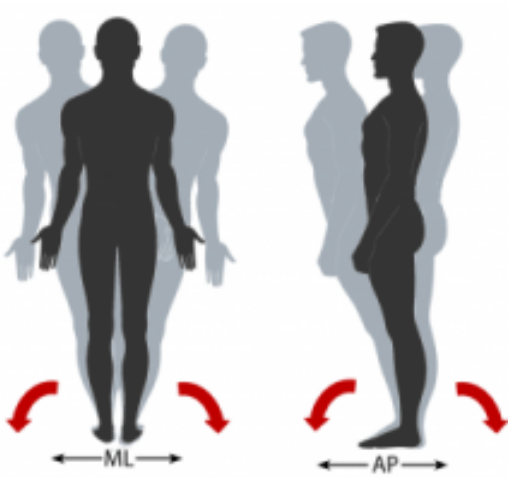

Figure 1.1: Postural Sway[1]

1.2 Balance and Postural Control

Technically defined, balance is the ability to maintain the body's center of mass over its base of support [21]. The center of mass is approximately at the 55% of the height of a human and the gravitational direction of the mass center has to fall on the supporting area as presented in Figure 1.2.

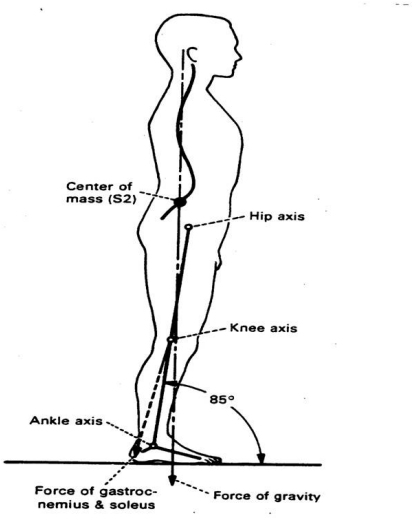

Figure 1.2: Human Posture [2]

Balance is a need while moving, standing, sitting or lying. Posture on the other hand is the stereotypical alignment of body/limb segments, when standing, sitting, lying or lifting etc. in static case and walking or running in the dynamic case. There is an obvious close relationship between balance and posture: It is the postural alignment, in other words the changes or adjustments made due to perturbations, which is the way balance is maintained. As can be seen from Figure 1.3 balance is achieved as a result of the interaction of many variables [22].

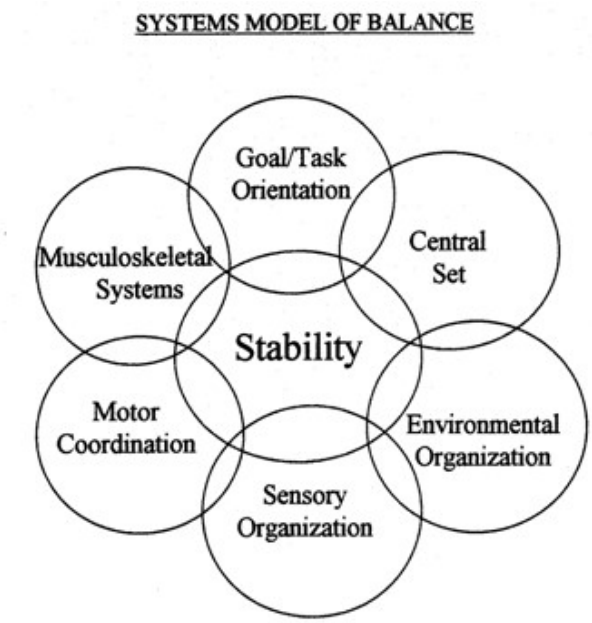

Figure 1.3: Systems Model of Posture (Sandra Rader, 2018)

There is naturally a limit that a subject can lean away from the mid-line without losing balance, stepping, or reaching for assistance. As shown in Figure 1.4 the stability limits can be defined with a cone. Where a normal sway envelope is 12.5 degrees anterior/posterior of which 8 degrees is anteriorly and 4.5 degrees is posteriorly, and 16 degrees in lateral direction, 8 degrees on the right and 8 degrees on the left side [21].

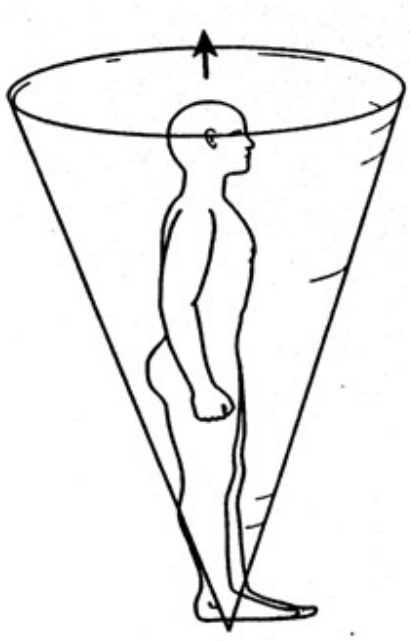

Figure 1.4: Limits of Stability [3]

To keep the center of gravity in these limits, avoiding a fall or collapsing of joints is achieved by various stabilizing systems. The musculoskeletal system, certainly, plays an important role. It is the main system that gives the human body the ability to move, the form, support, and stability. It is composed of the bones, joints, tendons and ligaments etc. The bones building up the skeleton provide the shape and form for the body, where muscles, providing the power, have the duty of movement of the bones and keeping them in place. Joints giving the degree of freedom allow motion to occur.

In this study, emphasis is laid on the "Sensory Organization" of postural control. Here visual, vestibular, and somatosensory systems play the major important role in control of the balance system. However, besides sensory inputs, balance is established with the integration of those sensory inputs, and motor output to the eye and muscles.

1.3 Sensory Input

1.3.1 The Somatosensory System

The somatosensory (soma=body, somatosensory: "touch sense") system is the dominant sensory system. Various specialized receptors have been associated with the somatosensory system which are in joints and muscles, skin, hair follicles. The receptors transduce mainly mechanical and thermal energy. [23] The somatosensory sense is a combination of sensory experiences, including touch, vibration, pressure, hair movement, joint position, warmth, cooling and pain. Here, the mechanoreceptors are sensitive to mechanical disturbances on skin or hair. These receptors supply information about the objects in the environment through physical contact. Information about the position and movement of the body or body parts (proprioception) are obtained through the stimulation of muscle and joints. These proprioceptive stimuli are internal forces which occur by the position or during the movement of the body part. The information of the position of the limb is obtained through the static forces on the joints, muscles and tendons. The movement of the limb is indicated by changes in the forces in muscles, tendons and joints. This outcome, proprioception, has critical importance on posture and balance as it affects motor responses. Senses from muscles and joints form the proprioceptive infromation. Sensory receptors in these related tissues of human body are sensistive to pressure. These signals help the brain to perceive the spatial position of the human body wholely or the part of the body in action.

Moreover, somatosensory system include cutaneous thermoreceptors. As their name implies, these receptors response to temperature change. It gives the information about the temperature of the body, external objects and environment. In addition, the system provides data about painful, itchy and tickling stimuli [24].

1.3.2 The Visual System

Vision is the key system giving information about the position, velocity and orientation of the body in space relative to other objects in the environment. The sensory receptors in the eye are rods and cones. Rods are providing to see the shapes of the surrounding and help to see when there is low light. Cones, on the other side, help to see the colors. Studies show that, there is a specific advantage of the visual input in balancing compared to having no visual cues [25].

1.3.3 The Vestibular System

Another important system is the vestibular system. The vestibular organ consists of the utricle, saccule and the semicircular canals which are in ears. The task of the utricle and saccule is to get the vertical orientation information i.e detect gravity and linear motion. The semicircular canals are sensing the rotational movements. On the whole, this system senses information about motion, equilibrium and spatial orientation [4].

1.3.4 The Brain

Certainly, all the events, the gathering of information, evaluations and a creation of the output action happens in the brain. Especially, the brain stem and cerebellum are important junctions in the control of balance. Moreover, cerebral cortex controls the conscious actions of balance and movement. The mechanisms of the control balance by the brain is very complicated, any disorder of the balance control areas on the brain might result in severe damages [4].

1.3.5 Motor Output

All the sensory inputs, the eyes, muscles and joints, vestibular organs send information to the brain, where all the signals are combined and evaluated. The cerebellum and the cerebral cortex sorts the data and compares them with

learned information. Eventually, after sensory integration, the brain stem sends signals to the muscles of the eyes, legs, head, neck etc. allowing to maintain balance. Figure 1.5 summarizes the balance process in terms of the tasks in each step.

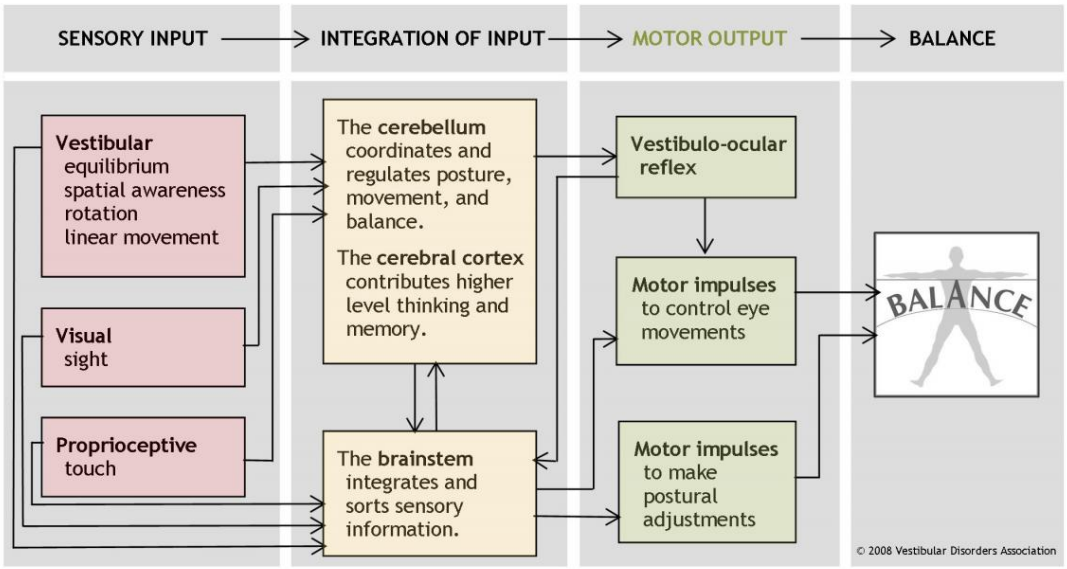

Figure 1.5: Balance Control Systems [4]

An important feature of the motor output to muscles and joints is pathway facilitation. It is basically the process of learning the pathway of the impulses to travel along the nerve. The golden rule here is repetition of the activity, resulting the impulses to travel easier, thus leading to a faster and more confident control.

The vestibular apparatus has also direct control over the eyes. With the Vestibulo-Ocular Reflex eye movements are controlled and the gaze is stabilized when the head is moving.

Comprising a complex, interlacing sensory-motor control, human balance system functioning might be hindered by injuries, diseases or aging. This complexity also creates difficulties in the diagnosis, and the determination of the real reason of the balance problem remains as a problem. [4]

1.3.6 Balance Disorders

As discussed in the previous sections, there are many variables that the brain and the body deals to achieve balance. Any malfunction, damage or disease of the system may result in balance problems. Balance disorders are situations where people feel unsteady or dizzy. It is a condition in which there is the feeling of moving or spinning while standing, sitting or lying. When balance is impaired such symptoms like dizziness, blurred vision, confusion, falling, faintness etc. may occur. Some balance disorders are "Benign paroxysmal positional vertigo (BPPV), Labyrinthitis, Meniere's Diesase, Vestibular neuronitis, Perilymph fistula, Mal de Debarquement syndrome (MdDS)

1.4 Diagnostics of Balance Disorders

The diagnosis of balance disorder is a difficult process. Firstly, it is because of the complexity of the balance system itself, and many types of the disorders. In addition, other health problems, like ear infections, blood pressure instabilities, vision problems etc. may lead to balance disorders, too. Therefore, different opinions exist about which tool to choose in the assessment of balance [26]. There are some important views on the quality and coverage of the assessment. Accordingly, balance assessments should take into account the change of balance strategies which may vary with the change of sensory conditions, support base, changes of the person's behaviour and experience etc. . Furthermore, the assessment has to differentiate the balance control type between the response to external perturbations and voluntery actions. Because of the many aspects of balance control, there is no unique assessment method. There are three main approaches in the assessment which are the functionl approach, system approach and quantitative posturography [27].

1.4.1 Functional Approach to Balance Assessment

In this case there is the need to know whether or not there exists a balance disorder. Revealing the functional restrictions in everyday life is aimed, like having stability problems while standing or walking, facing with problems when standing up from a chair. In general, functional balance tests analyze a set of motor tasks for specific postures. Rating the performance of the patient is done by scoring up to a five point scale or recording the amount of time balance is maintained.

Rehabilitation therapists commonly use various types of functional scales; however, these scales are not able to predict the risk of falls for neurological patients. Furthermore, these scales lack the effect of sensory environmental context and cognitive effects [27].

One commonly used functional balance test developed by Tinnetti has nine items. Tasks are perturbations on the chest, sit to stand and turning 360 degrees. Evaluation is done on a three point scale which are able/safe to unable/unsafe. Tinnetti's assessment method lacks the environmental effects but predicts spontaneous falls [27].

The most known assessment method of balance disorders is the Berg Balance Scale. This method consists of 14 items, testing patients competency in static and dynamic conditions. Tests take place in sitting, standing, leaning, turning and on one leg positions. In addition, other scenarios like chaning positions, reaching forward, turning around, picking up an object from the floor and stepping on a stool are tested, too[26]. The Berg Balance Scale scores from zero to four, measuring the clinical status and fall risk of the patients. The scenario items are developed to represent common daily life. Similar to Tinnetti's test, Berg's test does not score the performance of altered sensory context or attentional distracters.

1.4.2 System Approach to Balance Assessment

This approach is used when the reason of the balance disorder is to be determined. So, the subcomponents of balance control are investigated. As can be seen from Figure 1.6, the system approach handles the problem by dividing it into three main categories which are biomechanical, motor coordination and sensory organization constraints.

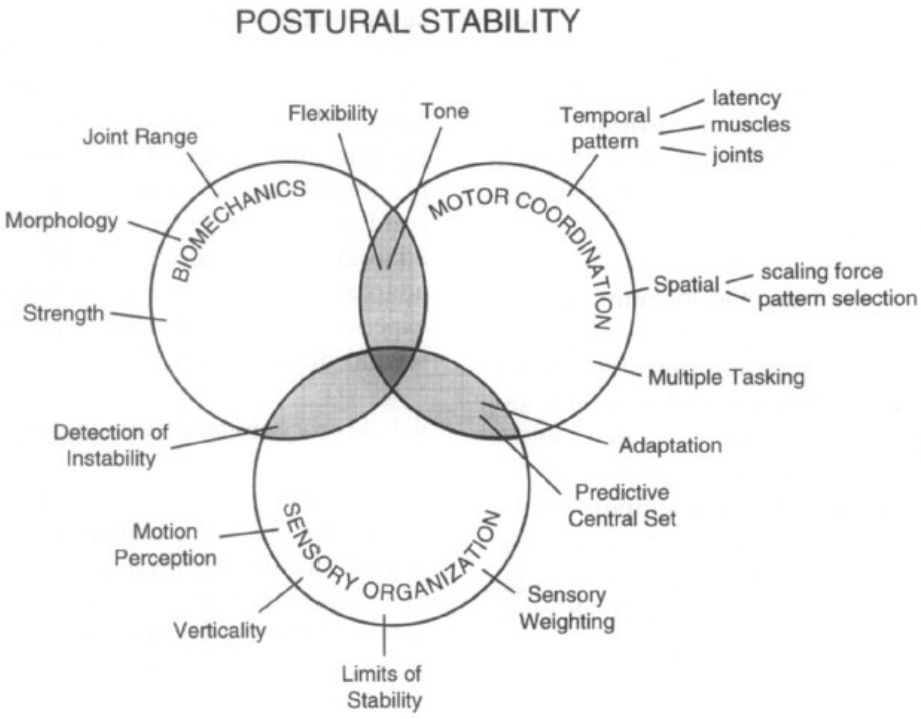

Figure 1.6: System Assessment (Horak, 1997)

In biomechanical subcomponents joints, muscles functionality, strength, flexibility, range and alignment in different postures are evaluated.

For the case in motor coordination subcomponents postural movement strategies of the patient are analyzed for three main scenarios. One is the evaluation of maintaining stability to external perturbations like suface displacement or a nudge. Second one is the stability performance in the anticipation of voluntary movement of the arm or raising the leg and the third is the ability when moving the whole body, when leaning, walking or swaying [27].

The assessment of sensory system includes visual, vestibular and somatosensory systems. This assessment evaluates the performance of maintaining stability and orientation for changing sensory conditions where eyes are closed, open, for moving or stationary surfaces and visual surrounds. To find how the sensory system is used, a clinical test for sensory interaction in balance, or CTSIB in short, is designed by Cook and Horak. In this test, for different conditions the presence and accuracy of senses are altered. With the help of a viscous foam, somatosensory information is isolated, and an inaccurate input is given. Vision is directly excluded by closing the eyes. Hence, with various tasks and test conditions the problematic sensory system can be identified through the analysis of the responses of the patients [28].

1.4.3 Instrumental Approach to Balance Assessment

Functional clinical assessment methods have the disadvantage that the results may differ from one examiner to other as the conductance of the test and scoring involves too much subjectivity. To overcome this problem, the use of instruments replaces manuel methods, giving quantitative measurement results.

Mostly used instruments in this field are force plates, stereophotogrammetric devices and wearable inertial sensors. Force plates are platforms that measure reaction forces and moments acting on them. The swaying motion or the center of pressure (CoP) can be tracked and recorded with these devices. Stereophotogrammetric devices are useful when the movements of the whole body needs to be recorded. Here, retroreflective markers are used for the detection of motions. Wearable inertial sensors are clothings or other wearable tools which are comprising of high technologies for motion or force measurements.

1.4.3.1 Static Posturography

In this method, subjects stand on a force plate which does not move. The CoP displacements of the patient on the platform are measured by the force transducers of the plate and postural control assessment is obtained. To give a clear

explanation, CoP is the projection of the center of mass (CoM) on the base of support, which is the force plate in this case. The CoP data give ideas about the muscle activity on balance control mechanisms. The swaying motion, i.e. the displacements of the CoM, is the key parameter in posturography. In biomechanical point of view, it is the controlled variable of balance system and shows the net neuromuscular responses. In short, comments can be made through the measurements of CoP with the static posturography method as it is directly reflecting the sway motion. However, when considering the overall system, although it is accepted that postural sway is a great measure in commenting on the health state, it does not give information about the underlying reason of the disorder.

1.4.3.2 Dynamic Posturography

Dynamic posturography is the method where patients are exposed to external perturbations. The perturbations can be directly applied to the body like giving a pulling or pushing force to the shoulders or pelvis. Another option to create the perturbation is using a viscous foam or the platform which the patient stands on can be moved, controlled by a computer. Giving motion inputs to the supporting base platform or changing visual conditions the Dynamic Posturography method exposes patients to different controlled inputs. At the end it quantifies the responses of the patient, identifying the state of the balance system. In Dynamic Posturography tests, patients are standing on a movable force plate, enclosed by a visual surround. With the help of computer control, the movable force platform either rotates about a fixed point or translates, horizontally. However, another freedom to the movable platform was not added in order to reach a result in the analysis as otherwise would be too complex. Here, the forward-backward sway motion of human was represented as critical [29]. Moreover, having the ability to move the visual surround or changing the visual scene, it is possible to manipulate each sensory input of the human balance system. Actually, Dynamic Posturography (or CDP) is the only accepted method which is able to isolate the functional contributions of each sensory (visual, somatosensory, vestibular) input, central integrating mechanisms and neuromuscular system outputs for

postural and balance control [30].

Computerized Dynamic Posturography (CDP) : It is possible with Computerized Dynamic Posturography to get a differential assessment of disorders by three sensory and motor protocols which are the Sensory Organization Test (SOT), the Motor Control Test (MCT) and the Adaptation Test (ADT). So CDP can identify and differentiate the functional impairments associated with the pathological processes, but CDP cannot diagnose pathology or site-of-lesion [31].

The Sensory Organization Test, which is theorized by Lewis Michael Nashner in his doctoral thesis in 1970, identifies postural control disabilities by looking at patients utilization or suppressing the sensory systems as presented in Figure 1.7.

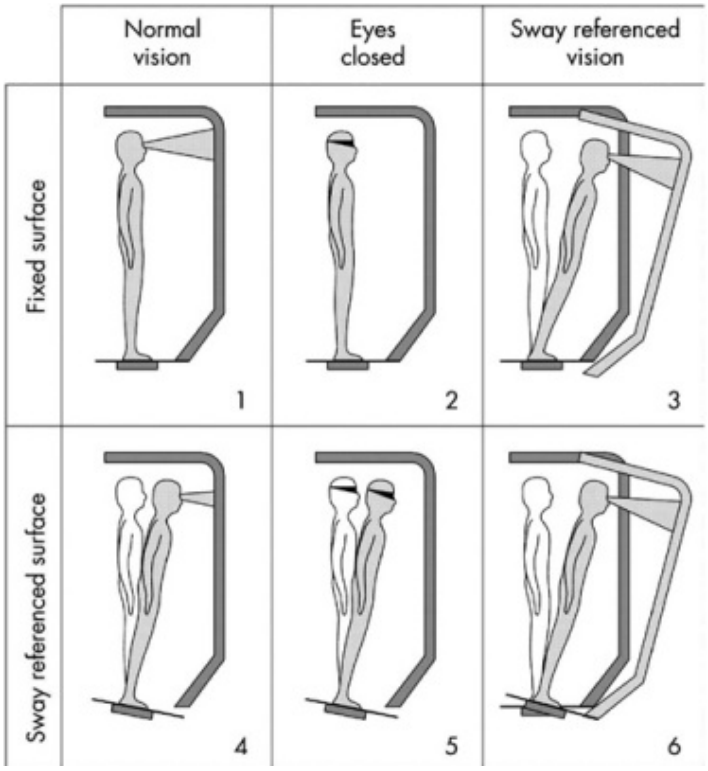

Figure 1.7: Sensory Organization Test [5]

During the test, the measured body sway motion is fed to the support platform

and visual surround, to eliminate patient's eye, feet and joint informations. So the "Sway Referenced" motions, the tilt of the base platform and the visual surround, are directly following the patient's anteroposterior body sway, thus, the orientation information is eliminated. With the help of controlling the support base and visual surround, and also by changing the conditions of the subjects' eyes as open and closed, this test may control visual and support surface information, besides it may create sensory conflict situations. To sum up, the Sensory Organization Test aims to isolate the vestibular system for balancing, and make patients be disabled to use sensory information and respond unadaptively.

The Motor Control Test is applied with platform translational motion in forward and backward directions as presented in Figure 1.8. This test analyzes the patient's responses to sudden/unexpected external perturbations. The ability of the patients to recover automatically is measured by onset time, strength and lateral symmetry of their responses.

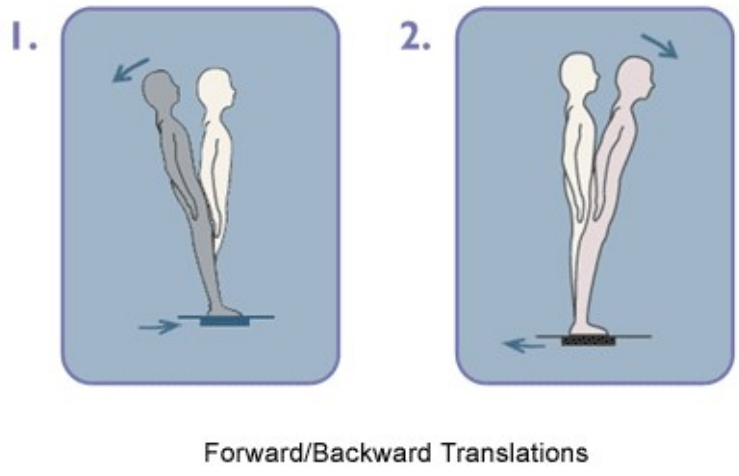

Figure 1.8: Motor Control Test [5]

The Adaptation Test is done to resemble daily life situations like facing with irregular surfaces. The support base rotates in toes-up and toes-down directions as presented in Figure 1.9, but without the patient's knowledge of which direction and what exact time the perturbation takes place. This test assesses the ability of patients to adapt motor reactions and minimize swaying motion with

the unpredicted base support motions. Quantification is done with the measurements of reaction forces, which are applied to overcome the perturbation.

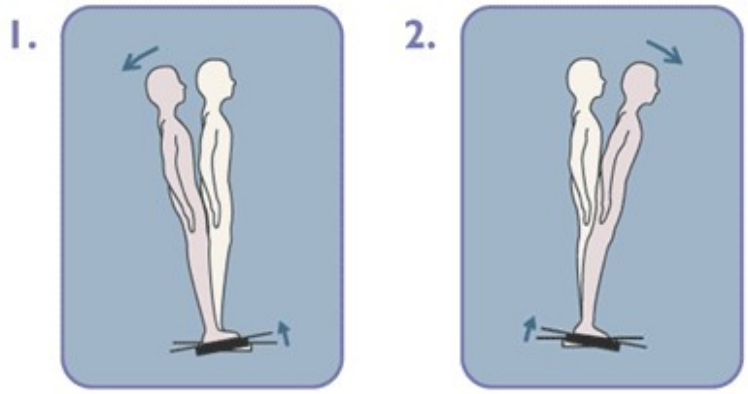

Figure 1.9: Adaptation Test [5]

1.5 Aim of the study

The aim of this study is offering a new device that runs the standard CDP-protocol tests; moreover, an additional rotation axis about the ankle joint was designed which does not exist on standard posturography devices, so far. The new motion which is the rotation about lateral axis; thus, opens new gates for medical investigations. Hence, a controlled movable platform having three degrees of freedom was designed together with an integrated force plate and a controlled movable visual surround. Another aim was to develop a six axis force transducer which may also be a totally independent device for the purpose of obtaining more detailed ground reaction force data during CDP measurements for research purposes.

CHAPTER 2

LITERATURE & MARKET SURVEY

2.1 Introduction

Quantification of balance, realised by Computerized Dynamic Posturography is an accepted important tool. The studies done on the CDP device showed its distinctive contribution in the objective diagnosis of balance in cilinics, so far [31]. On the other hand, the CDP method is based on anterior-posterior response about the ankle joint disregarding the lateral effects and responses. However, studies show that lateral stability is also an important parameter in human balance system. Lateral stability was investigated for seated patients in dynamic environments using a servo-controlled tilt platform as can be seen in Figure 2.1 and Figure 2.2 [7]. In these studies postural control mechanisms were analysed in response to vehicle turning and breaking, stressing lateral balance.

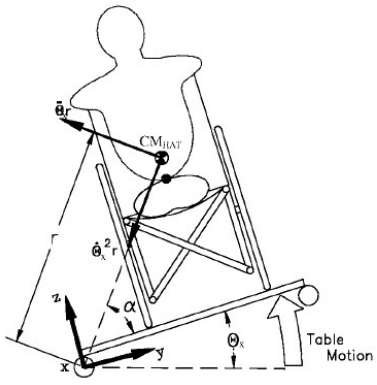

Figure 2.1: Schematic of platform tilt rotation [6]

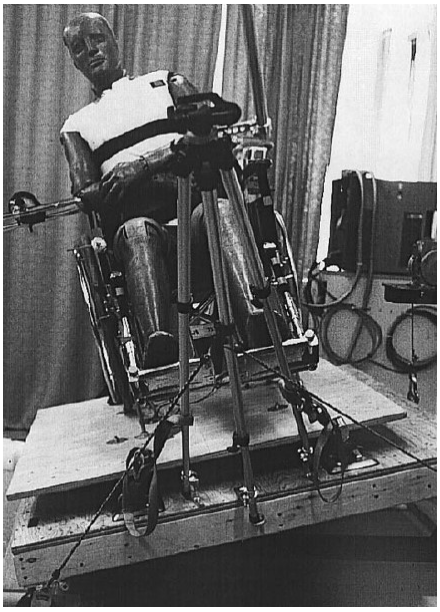

Figure 2.2: Tilt platform with test dummy rolled to right [7]

Another study related with lateral stability was done on patients with Parkinson's disease (PD). In this study, lateral stepping responses for postural adjustments were investigated with the use of a translating platform in lateral directions, it was found that lateral stability was an important parameter in the rate of falls in PD patients, thus, improving lateral weight shifts and step strategies were suggested in rehabilitation programs [32].

In addition to these studies, a recent study focused on the vestibular signals of head movement in maintaining upright posture. A multi degree of freedom moving platform was used to generate illusions for the vestibular system. (Forbes et al., 2016) Especially, anterior-posterior and medio-lateral rotations of the platform about the ankle joints, presented in Figure 2.3, were studied. It was found that there was a relation between the direction of vestibular disturbance, the head yaw angle and lateral stability. Hence, ML rotation about the midpoint between the ankles was studied [8].

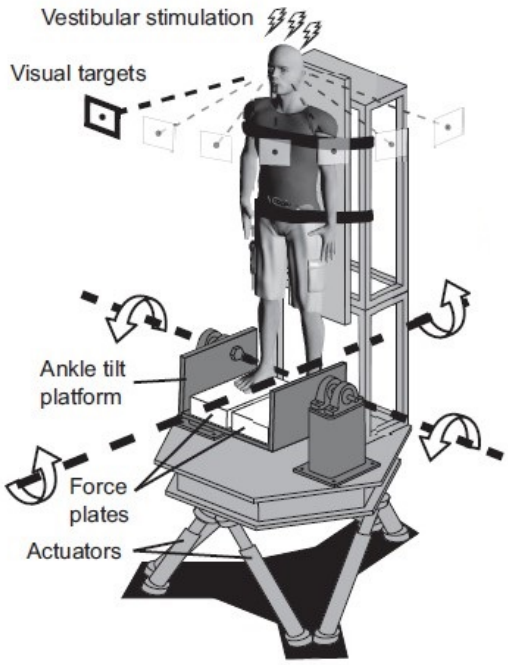

Figure 2.3: Experimental setup of two-rotation axis platform [8]

2.2 CDP Device

In this section a closer look to the device is given, moving away from the physiological point of view. Devices with CDP-protocol available in some hospitals and physical therapy centers over the world are presented below.

2.2.1 Neurocom - SMART EquiTest System TM

This was the commercialised and patented system in 1988 by Lew M. Nashner who also developed the CDP protocol. Besides the main CDP Tests (SOT, ADT and MCT) other tests like the Limits of Stability (LoS), Rhythmic Weight Shift (RWS) and Weight Bearing Squat (WBS) can be applied. This system, shown in Figure 2.4 has a step height of 15 *cm* platform, in which a force plate is also integrated.

Figure 2.4: SMART EquiTest CDP [9]

The force plate mainly measures the Center of Pressure (CoP), which is essential for tracking the postural sway and measuring the responses of the patient subjected to the external perturbations. The platform has the ability to translate in forward/backward direction +/-6.35 cm, performing a maximum velocity of 15 cm/s. Rotational platform motion is about the ankle joint in range +/-10 deg, with a maximum speed of 50 deg/s. Furthermore, the visual surround also rotates in the Anterior-Posterior direction +/-10 deg, having a maximum rotational speed of 15 deg/s. The maximum subject height and weight for the device to be used are 203 cm and 200 kg, respectively. In this device the patient is protected from a fall with the harness set attached to the overhead supporting bar. All the commands are given by the operator through the system computer. The basic important information are also given as inputs to the computer like the age and height of the patients. These data are then used during and at the end of the diagnosis in calculating balance scores and in making comparisons

with normative data that are in the memory of the computer. In addition, to give the commands also visually to the patient, a flat LCD monitor is used, embedded to the visual surround.

In Figure 2.5, from the patent document published in 1993, the concept design of the system is shown. The platform motions are simply controlled by different actutators where the axes are interbedded. Actuators are placed below the supporting force platform base. In this design at the outest core, translational motion takes place where the rotational motion mechanism and the force plate are also in the translational moving assembly. AP rotational motion; on the other hand, is an inner layer between the force plate and the translational mechanism. Finally, the force plate is placed in the innest part of the entire platform design. All platform motions are performed by linear actuators, where one end of the actuator is attached to the fixed part and other end is attached to the moving part [9].

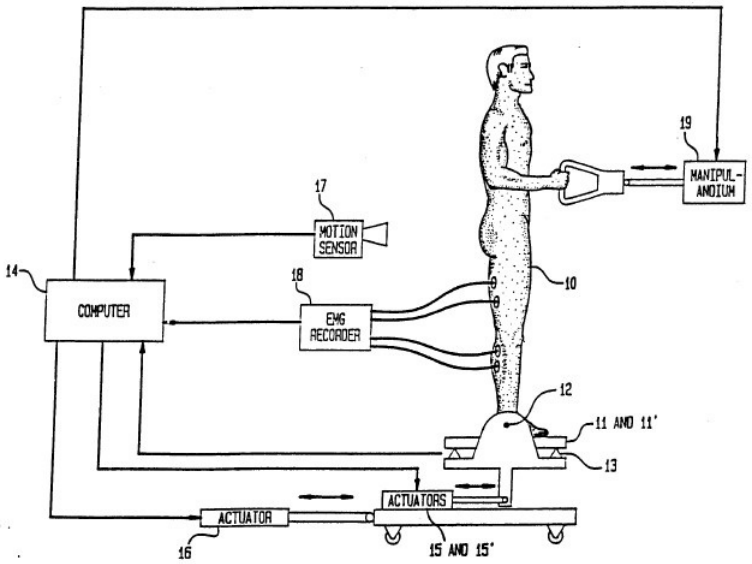

Figure 2.5: Neurocom Patent US 5,269,318

The visual surround is also rotated with the help of a linear actuator as can be seen from Figure 2.6.

Figure 2.6: SMART EquiTest CDP [10]

2.2.2 Bertec - Balance Advantage Dynamic CDP TM

Having announced as the second generation CDP device, Bertec developed a new device with recent technology including high virtual reality applications. As shown in Figure 2.7 the device has a low step height of about 10 cm.

Figure 2.7: Balance Advantage Dynamic CDP [11]

A force plate having about 225 kg load capacity is integrated to the base platform. All tests that run on Neurocom is available in this product, too. The platform motions are also like the Neurocom ones, it rotates about the ankle joint and translates in forwards/backwards directions. However, there is no visual surround rotation, but the visual scene changes with the help of the projector which is placed above the patient. The images are genereated and controlled with the system computer. Due to its programmable visual scene projection option, there is no limit in giving different visual inputs. This feature is also very useful in rehabilitaion purposes, as games and daily-life scenes can be applied, easily. Also in this system the patient is protected with a harness set similar to Neurocom-EquiTest device.

In Figure 2.8 form the patent document which is published in 2014, it can be seen that Bertec tried to get a low step height design by placing the rotational

platform motion mechanism above the supporting surface. The claims of the patent indicate the positions of the actuation mechanisms; hence, as it is a recent patent the claimed items in the patent were tried not to be violated in the design. Like the Neurocom design, the force plate is placed at the most inner position and the translastional motion mechanism is at the outest part[11].

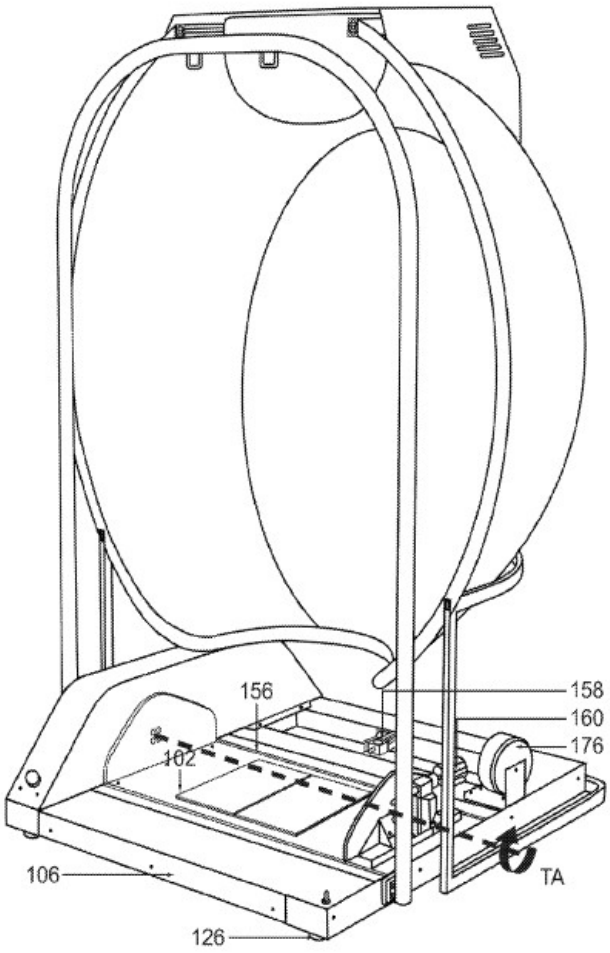

Figure 2.8: Bertec Patent US 8,704,855 B1

Considering both devices by Neurocom and Bertec, the design of the CDP device in question, including a further motion axis and having a similar conceptual design like Neurocom Smart Equitest, does not violate any patent.

2.2.3 Synapsys - Synapsys Posturography System (SPS) TM

As can be seen from Figure 2.9 the Synapsys Posturography System has two steps to get on the platform. It is asserted that the system is able to do the SOT test; however there is only translational platform motion having +/- 8 cm range with maximum 10 cm/s speed. This system also utilizes a projector for visual support.

Figure 2.9: Dynamic SPS [12]

2.2.4 Balance Quest - Computerized Dynamic Posturography TM

Micromedical Technologies Inc. also developed a device asserting the device applies the CDP-protocol. To get on the platform it is neccessary to climb three steps as presented in Figure 2.10. Visual input is given by "Virtual Environment Glasses". There is one actuator moving the platform. In this system it is possible

to float the platform over the spring suspensions when released. This enables to move the platform randomly in any direction having 6 DoF of movement. Again in this system it is not clear how the system applies the entire CDP-protocol.

Figure 2.10: Micromedical Balance Quest - CDP

2.3 Force Plate Technology

Force plates are instruments that measure and record the ground reaction forces and moments exerted on the platform. In biomechanical field force plates are used mainly for gait and human locomotion analysis, balance and posture studies and in sports sciences researches. Depending on the application, this device may be a balance plate, force platform, jumping plate or an instrumented treadmill. Among these systems force plates are special designs for sensitive force measurements.

The most common and simplest force plates are bathroom scales, only the vertical force acting on it is measured where the one sensor is at the geometric center or the sensors are at the four corners of the plate. Besides the weight

of the subject on it, force plates also measure the exact application point of the resultant vertical force. In the typical usage, the force plate measures the subject's Center of Pressure (CoP) and with the sway of the subject the change in the CoP is also indicated. CoP is found by calculating the simplest resultant of the vertical forces acting on the platform; moreover, there exist other two force components in the horizontal plane of the platform. In order to measure the horizontal forces, transducers which are sensitive in those directions are required [33]. There are different techniques for force measurement and various commercial products as presented. In order to measure a force, an indirect way for sensing of the response of the magnitude of the force has to be provided. In general all force plate designs are based on the deflection of a sensing element, indicating the applied force. Here the sensing element is selected so that the applied force is directly proportional to the displacement of the element. Generally the displacements are relatively small; therefore, very sensitive devices are required. Four transducing methods are used in force plate applications; mechanical springs and pointers, piezoelectric crystals, linear variable differential transformers, and electric resistance strain gages [34]. Today, two of the four techniques are mostly used in field which are piezoelectric crystals and electric resistance strain gages.

2.3.1 Piezoelectric Crystals

Some materials like quartz respond shape change under force by generating electric charge, which is called the piezoelectric effect. With the use of electrodes attached to the crystal surface shear or thickness changes can be sensed. In the design of a piezoelectric crystal based force platform, four quartz crystals are placed at the corners of the platform consisting of a rigid upper and lower plate. The upper plate is supported by the crystals at the corners which are measuring vertical forces. Horizontal forces can be measured by other two piezoelectric crystals in fore-aft and lateral shear directions. Piezoelectric crystal based Kistler (TM) product is presented in Figure 2.11. Piezoelectric sensor based platforms are suitable for dynamic force measurement applications, but are not convenient for static applications as the charge developing on the sensor

by the applied force leaks to zero, in time.

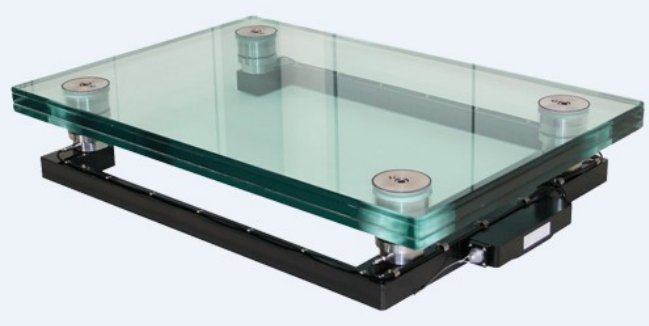

Figure 2.11: Kistler Force Plate [13]

2.3.2 Electric Resistance Strain Gages

Electric resistance strain gages are the most widely used elements for force measurement. A strain gage as can be seen in Figure 2.12 is a short length wire that is glued to the deforming fixture part. Under load, the change in the resistance proportional to the deformation can be used as a measure of the applied force on the element.

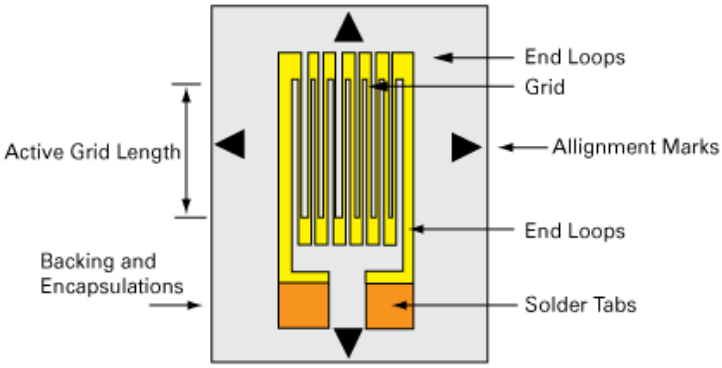

Figure 2.12: Strain Gage Drawing [14]

There are various types of strain gages depending on the requirement, sensitivity, range, dynamic characteristics etc. Strain gage based AMTI (TM) and Bertec

(TM) products can be seen in Figure 2.13 and Figure2.14.

Figure 2.13: AMTI Force Plate [15]

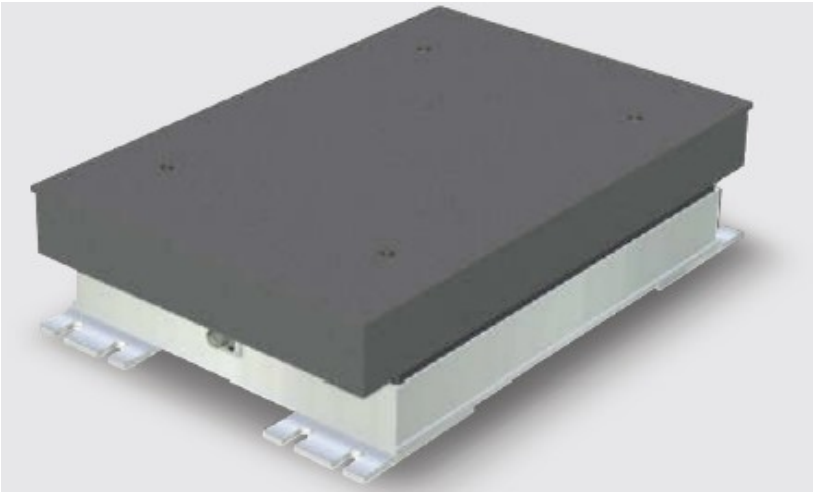

Figure 2.14: Bertec Force Plate [11]

Load Cells: Load cells are special structures designed for measuring force and torque. Strain gages are bonded on elastic materials like metals having specific geometrical design optimized for the application. Some types of load cells are; Bending Beam Cells, S Beam Cells, Load Button Cells, Shear Beam Cells, etc. For a low profile design a bending type load cell as presented in Figure 2.15 would be suitable.

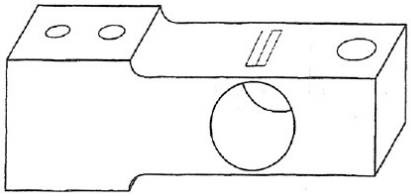

Figure 2.15: Bending Beam Cell [16]

Compared to specifically developed force plates, loadcells are cheaper, easier to integrate to designs and are a more available solution for force measurements. However, at the end, a design dependent on commercial product geometry would be obtained.

CHAPTER 3

DESIGN OF A CDP DEVICE

3.1 General Considerations

In previous chapters commerical CDP-devices that are available in field were explained. Retrieving some useful data from those systems, some basic capabilities that the device has to accomplish was determined. According to those systems, the design for a standart CDP-Device has to include at least:

- A force plate which is embedded in the moving base platform, measuring the CoP and shear force in forwards-backwards (AP) direction,
- Tilting motion of the base platform where the patient stands on and where the rotation is about the ankle joint in AP direction,
- Forwards-backwards translational motion of the base platform,
- Change in the visual surround; either by a tilting motion of the surround-view or by the change of the view itself with the aid of an instrument like a projector,
- An operating computer.

The performance requirements of each criterion are listed in Table 3.1.

Moreover, it was planned to be a modular design: The device was thought to be designed so that taking out any platform motion mechanism should not affect the whole design too much. In fact, if desired later by the customer, it was

Table3.1: Performance Requirements

Function	Range	Speed	Tolerance
Force Plate	140 kg	-	+/-1 % CoP Error
AP Rotation	+/-10 deg	50 deg/s	+/-5 %
Forwards/Backwards Translation	+/- 8 cm	15 cm/s	+/-5 %
Visual Surround Rotation	+/-10 deg	15 deg/s	+/-5 %
ML Rotation	+/-10 deg	50 deg/s	+/-5 %

planned to add the requested platform motion mechanisms without changing the whole system, easily.

As mentioned before, as a motivation of this study, a third motion axis which can be accepted as a new contribution in posture analysis studies was realised. To clarify, a servo-controlled rotational motion about foot ankle in ML direction was designed and implemented.

At the end contributing all these aspects, a final product having low step height was aimed in order not to forget patients' disabilities.

3.2 System Design

Before beginning with mechanism and structural design the architecture was studied. Physical architecture, electrical and digital interfaces of the whole system are presented in Figure 3.1 and Figure 3.2. The whole system can be divided into four main subsystems. The perturbing system gives the patient distorting inputs with platform and visual surround motions and measures the responses of the patient with the aid of the force plate. The harness secures the patient from falling. The power system supplies and distributes the required electrical energy to the whole system. Finally, interfaces are added for the operator to manage the system and the patient to navigate throughout the diagnosis.

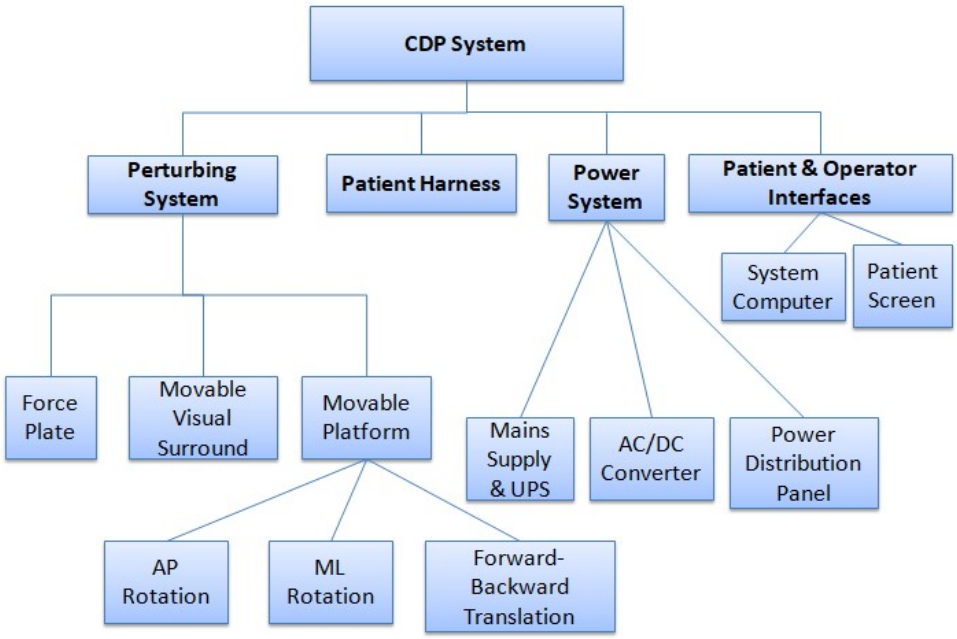

Figure 3.1: Physical Architecture

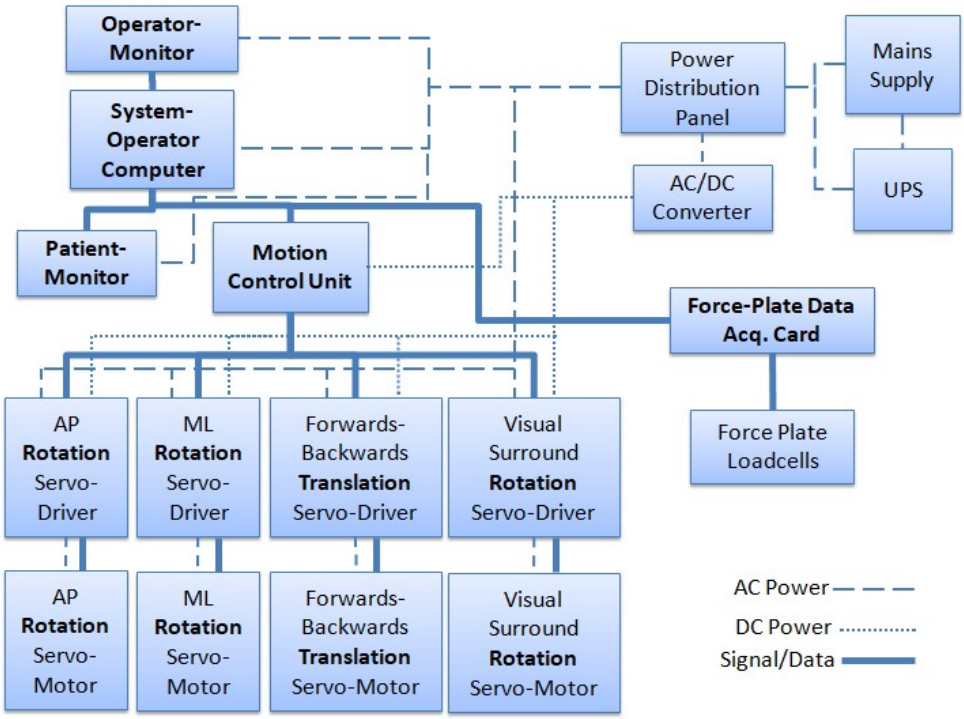

Figure 3.2: Interfaces of the System

In the following sections design details are explained.

3.3 Force Plate Design

As discussed in the previous chapters, CoP is the essential data needed for posturography evaluations. In balance tests, the patient may be guided through the patient screen. So, as the patient sways on the platform, the CoP point has to be monitored on the screen to show the patient his or her actual CoP position. Hence, the force plate should measure especially the vertical forces applied on it for CoP calculations and send the data to the operating system computer with very low latency. Moreover, for the Motor Control Test (MCT) the time instant at which the patient responses to the platform motion in horizontal direction has to be determined. Considering these requirements the suggested force plate design consists of the transducing component measuring vertical forces and horizontal force in AP direction and the data acquisition card. In the market, low cost force plates to be used for biomechanical purposes are present. Mostly, the structure is consisting of two rigid plates where one is above the other and the transducing element is placed between them. In general, the transducing element is the electric resistance strain gage based load cell. Load cells may take variety of shapes as explained in the previous chapter. In this study, as low step height size at the end of the design was set as a goal, low profile load cells were preferred.

Depending on the load cell position there are three main force plate configurations. First is the basic force plate where a single sensor at the center of the plate is placed. Second is a platform with a triangular shape where three load cells are placed at the corners. Lastly, the most common force plate is the rectangular one with sensors at the four corners. Depending on the requirement the load cells may be selected as multi-component to measure vertical and horizontal forces, but in this study uniaxial load cells are sufficient. However, a solution for measuring the shear force in AP direction for MCT test has to be developed.

The data acquisition card shown in Figure 3.3 consists of five amplifiers for the

load cells and a 24 bit analog to digital converter. The sampling frequency was set to be 200 Hz. With a USB interface the measured signals were logged to the system computer.

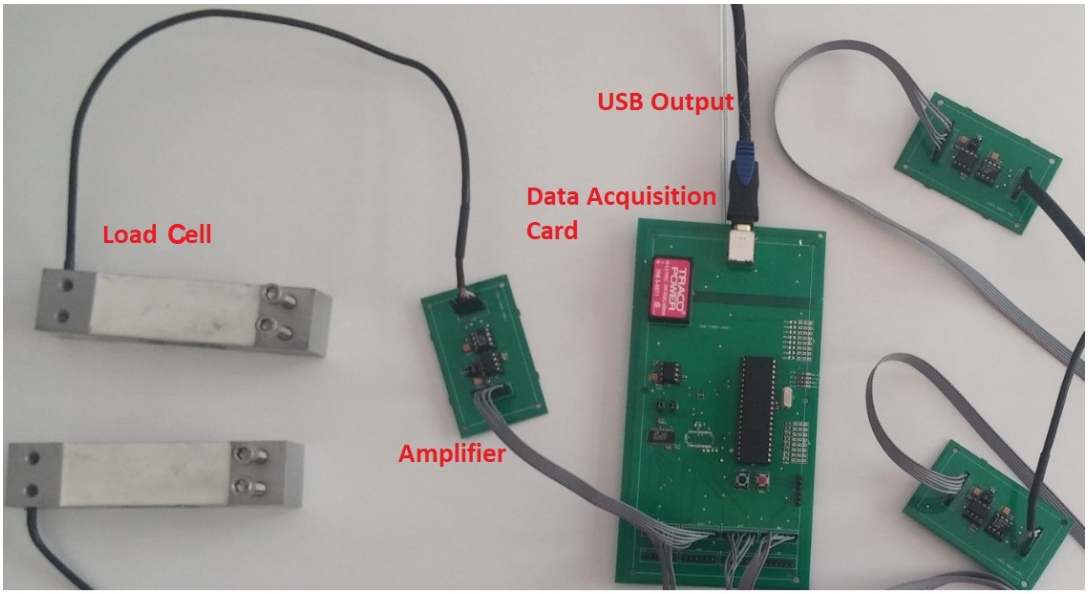

Figure 3.3: Force Plate Data Acquisition Card

3.3.1 Transducer selection

As presented in Table 3.1 the force plate has to be capable to make measurements for patients weighing up to 140 kg. The selected load cell is presented in Figure 3.4 where the properties of the product is shown in Table 3.2. It can be inferred from the table that the selected component is a uniaxial load cell, that means it is only sensitive to measure loads in one direction.The selected loadcell is built for loads up to 80 kg with a 160 kg overload capacity. Using four of these load cells in the platform the force plate will have a total capacity of 320 kg. However, it is thought that a 140 kg force may be applied on a single corner during the placement of the patient on the platform; therefore, a load cell with a overload capacity bigger than 140 kg was selected. Hence, for any scenario the load cell will not be deformed plastically and will not be damaged.

Figure 3.4: Esit SPA80 Loadcell

Table3.2: ESİT SPA 80 Loadcell Specifications

Specification	Unit	Value
Maximum Capacity (Emax)	kg	80
Total Error	%	0.006
Minimum Load	kg	0
Safe Overlaod	%Emax	150
Safe Side Load	%Emax	150
Ultimate Overload	%Emax	200
Operating Temperature	C	-10°C to +40°C
Recommended Excitation	V	10
Output Sensitivity	mV/V	2+/-10%
Weight	kg	0.17

3.3.2 Structural Design of the Force Plate

The suggested Force Plate structure is in rectangular configuration and the load cells are placed at the corners. The upper surface of the force plate was specified to be 500 x 500 mm considering the foot size of adult people. As uniaxial load cells were selected, three layers of aluminum plates were designed to measure the required vertical and horizontal force components. In Figure 3.5 the bottom layer of the force plate which is mounted to the subassembly rotating in AP direction can be seen. So with this layer the Force Plate is mechanically integrated to the moving subsystems. The details of this integration will be explained in later sections.

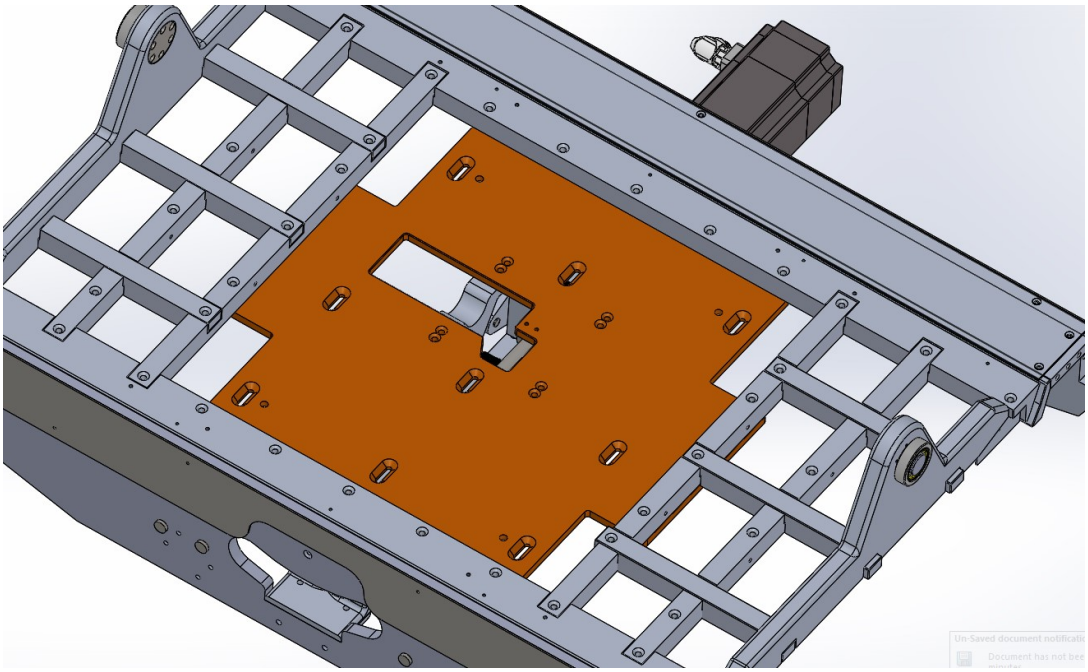

Figure 3.5: Base Layer of Force Plate

The bottom layer includes nine V-grooves for the placement of steel balls for bedding the mid layer plate to the bottom layer. In Figure 3.6 the placement of the shear sensor is shown. The load cell that is thought to measure shear force was attached to the bottom layer at one end and to the mid layer at the other end. It was rotated so that the load cell can be able to measure the forces

applied in horizontal plane in AP direction. In order to have the freedom to make measurements in that direction the unique bearing design with steel balls and V-grooves in the corresponding direction was applied.

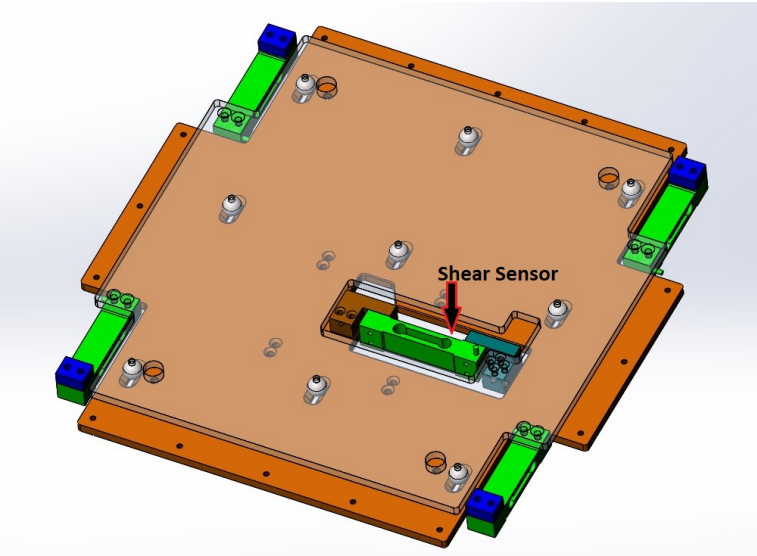

Figure 3.6: Shear Sensor Placement

Moreover, the mid layer also includes the mechanical interfaces to the load cells placed at the corners. In Figure 3.7 it is presented how load cells that are constructed to measure vertical forces are placed between upper and mid layer plates. Finally, in Figure 3.8 the upper surface of the Force Plate where the patients will stand is presented.

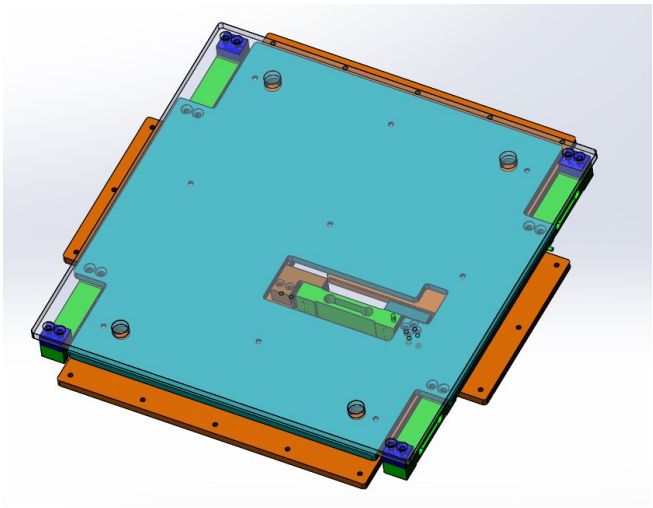

Figure 3.7: Mid Layer of Force Plate

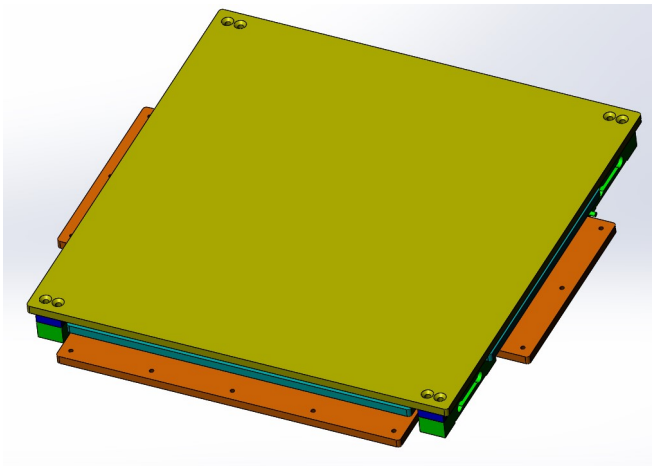

Figure 3.8: Force Plate Upper Surface

3.3.3 CoP Calculation

The method for calculating the center of pressure is straight-forward. All the required information is the force values of the load cells at the corners. As can be seen from Figure 3.9 the load cells are named as FL (Forward-Left), FR (Forward-Right), RL(Rear-Left) and RR (Rear-Right). The equation for calculating the CoP is presented in Equation 3.1 and 3.2. The results CoP_x and CoP_y are the distances from the geometric centre of the upper plate in "x" and

"y" direction.

$$CoP_x = \frac{(RF + RR) - (LF + LR)}{RF + RR + LF + LR} \cdot 226.5 \ \ mm \tag{3.1}$$

$$CoP_y = \frac{(RF + LF) - (LR + RR)}{RF + RR + LF + LR} \cdot 234 \ \ mm \tag{3.2}$$

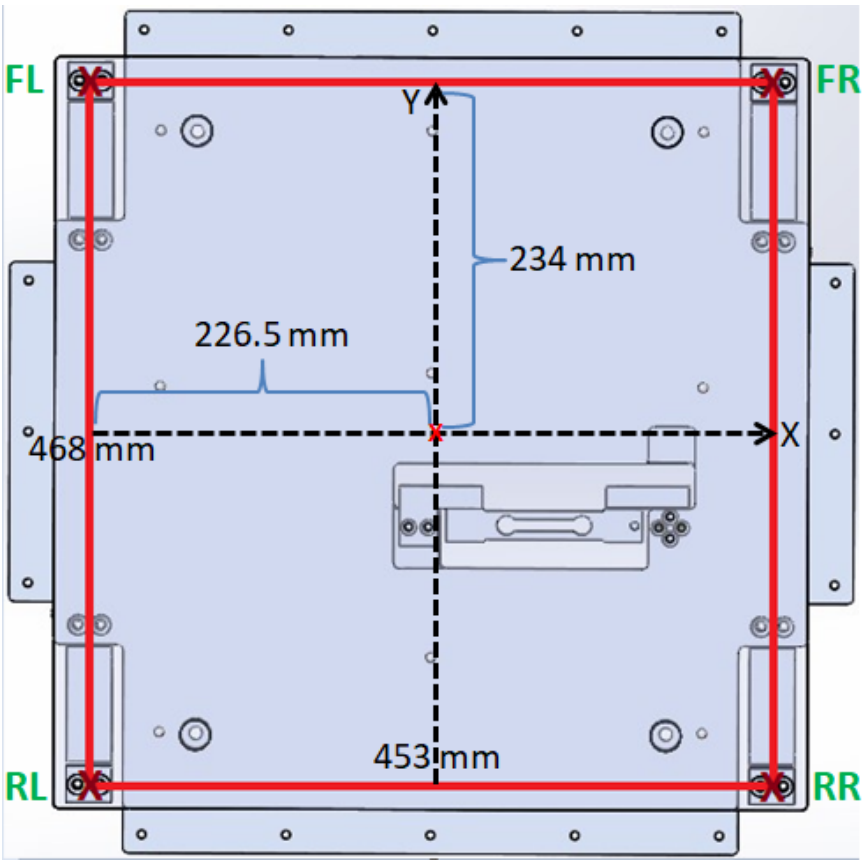

Figure 3.9: Force Plate Loadcell Positions

3.4 Mechanism Design

The requirements of the platform was determined in previous chapter. The ranges and speeds of each motion axes was specified. In order to satisfy these conditions alternative concepts were analysed. The studied concepts were Stewart platform having three degrees of freedom, four-bar mechanism, slider-crank

mechanism and geared mechanism. The details of each concept are described below.

i. Stewart Platform: The Stewart Platform that can be seen in Figure 3.10 is a special mechanism that can be used for platform motions having 6-DoF, three translational freedom and three rotational freedom in space. Less than 6-DoF platforms also exist for various applications. Three, four or five DoF platforms are available which are similar to the Stewart Platform. However, it is not easy to control these mechanisms, special algorithms have to be developed and complex kinematic analysis have to be performed. Moreover, the CDP-Device has to have a modular design where in this case the concept is not suitable.

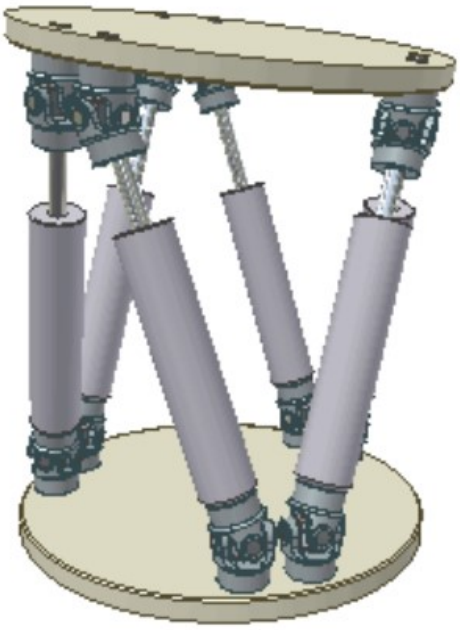

Figure 3.10: Stewart Platform Mechanism

ii. Four-bar Mechanism: A four-link mechanism with four revolute joints is in common called a four-bar mechanism. With this mechanism, platform rotational motions can be obtained. Moreover, with three revolute and one prismatic joint, called the slider-crank mechanism which is another four-link mecahnism, can be used for the translational motion. The conceptual design

can be seen in Figure 3.11 The red encircled area is the four-bar mechanism for the rotational motion of the platform. This block is put inside the translational block where the motion mechanism is encircled in green showing the slider-crank mechanism. The whole structure rests on rollers so that the translational motion can occur. For the rotational motion, in Figure 3.12 the resembling model is presented in 2D.

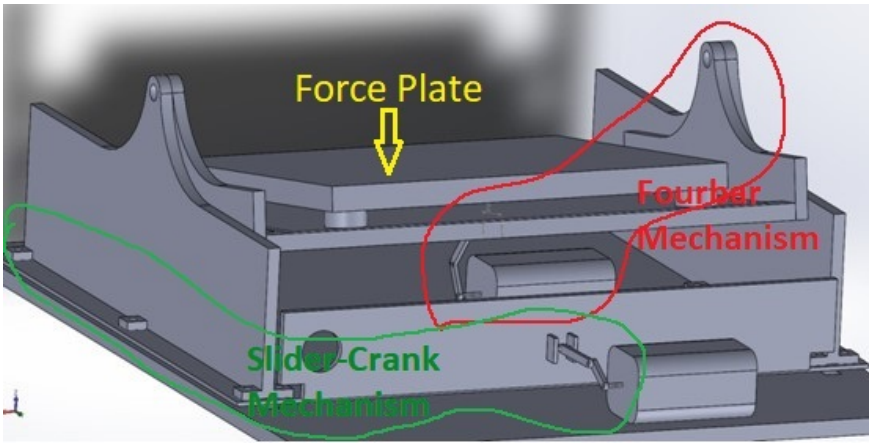

Figure 3.11: Fourbar Mechanism-Conceptual Platform Motion Design

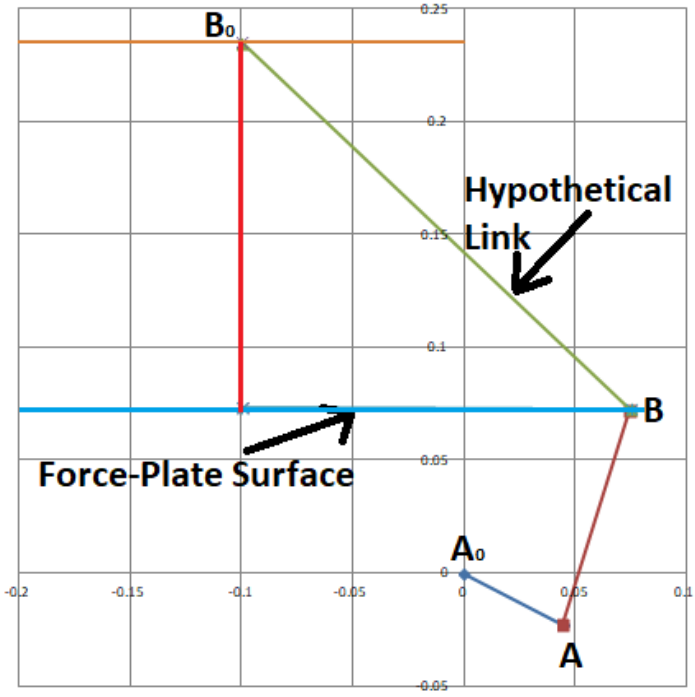

Figure 3.12: Fourbar Mechanism Kinematic Pre-Analysis-1

The derivation of the equations will not be explained in detail as it is only conceptual analysis. After writing the loop closure equation according to the defined points given in Figure 3.12,

$$\boldsymbol{A_0A} + \boldsymbol{AB} = \boldsymbol{A_0B_0} + \boldsymbol{B_0B} \tag{3.3}$$

the relation between input link A_0A and output link B_0B was obtained. A_0 is the point at which the prime mover supplies the motion input to the system and point B is the point where the coupler link is fixed to the output link, in this case to the base of the rotating platform or the force plate. Point B_0 is the fixed axis which the force plate is rotating about. As the angles are fixed with the output link and force plate surface, the relation between input angle and output platform rotation angle can be calculated, directly. Figure 3.13 shows the results of a prestudy of kinematic analysis of the four-bar mechanism between input link and force plate surface angle. Also, the linearity was sought in the analysis. The correlation coefficient shows a highly linear system. The required actuation torque was also calculated after performing the dynamic force analysis of the mechanism. The graph in Figure 3.14 shows that without a gearbox it is not feasable to move the platform with a patient on it.

Similar analysis was performed for the translational motion mechanism. The 2D model resembling the motion is presented in Figure 3.15.

The loop closure equation for the slider crank mechanism was written as;

$$\boldsymbol{A_0A} + \boldsymbol{AB} = \boldsymbol{s} \tag{3.4}$$

The relation between the input link A_0A and ouput link s was obtained and the following results were obtained. Figure 3.16 shows the results of a prestudy of kinematic analysis of the slider-crank mechanism between input link and platform translation. Also, the linearity was sought in the analysis. The correlation coefficient shows less linearity than the rotating mechanism. The required actuation torque was also calculated after performing the dynamic force analysis of the mechanism. Here a 140 kg (patient weight) load was assumed to be applied at the tip of the moving platform. So, for the worst scenario the required torque

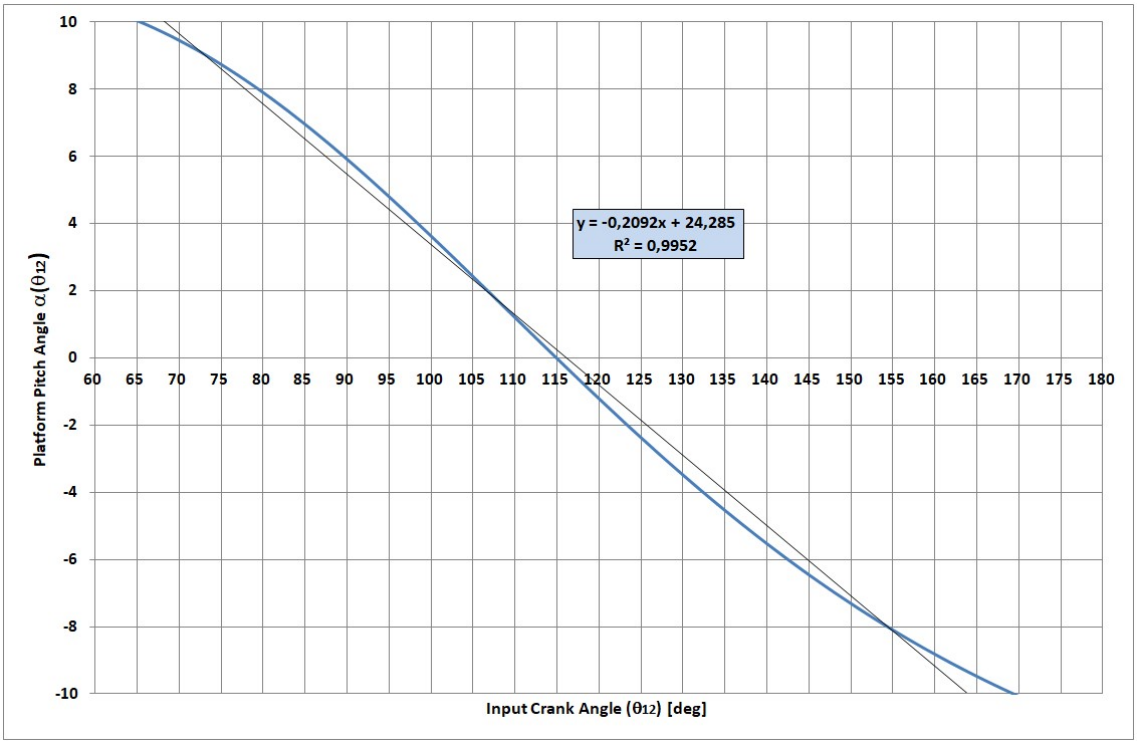

Figure 3.13: Fourbar Mechanism Kinematic Pre-Analysis-2

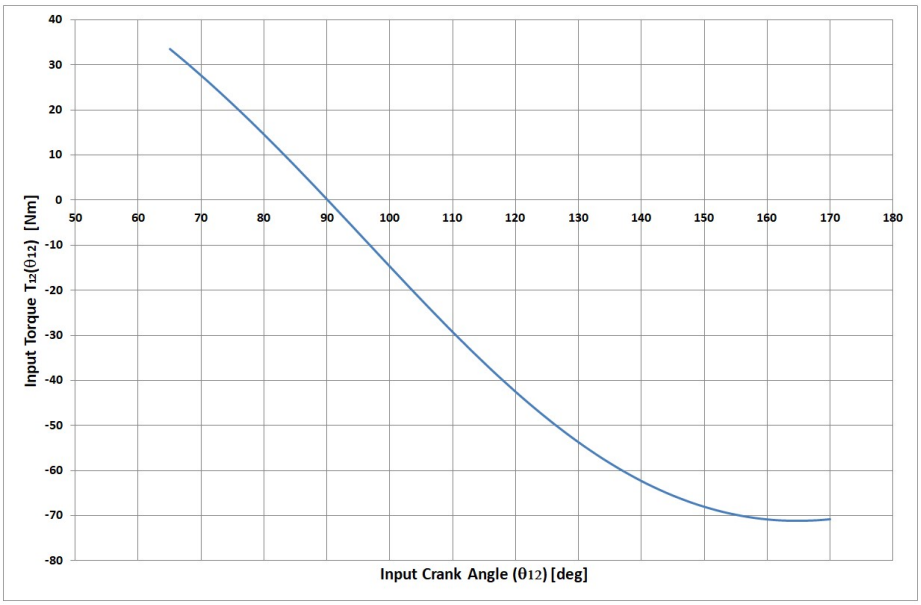

Figure 3.14: Fourbar Mechanism Kinematic Pre-Analysis-3

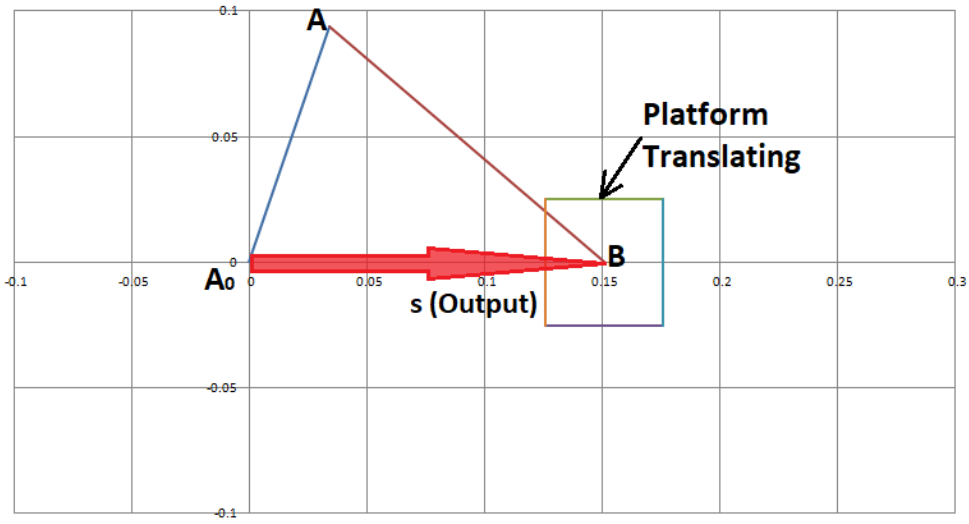

Figure 3.15: Slider-Crank Mechanism Kinematic Pre-Analysis-1

was found. Here, although the inertial forces for the crank and the coupler links were relatively small compared with the output link inertia, all the inertial forces were included in the computation. The graph in 3.17 shows that without a gearbox it is not feasable to move the platform with a patient on it.

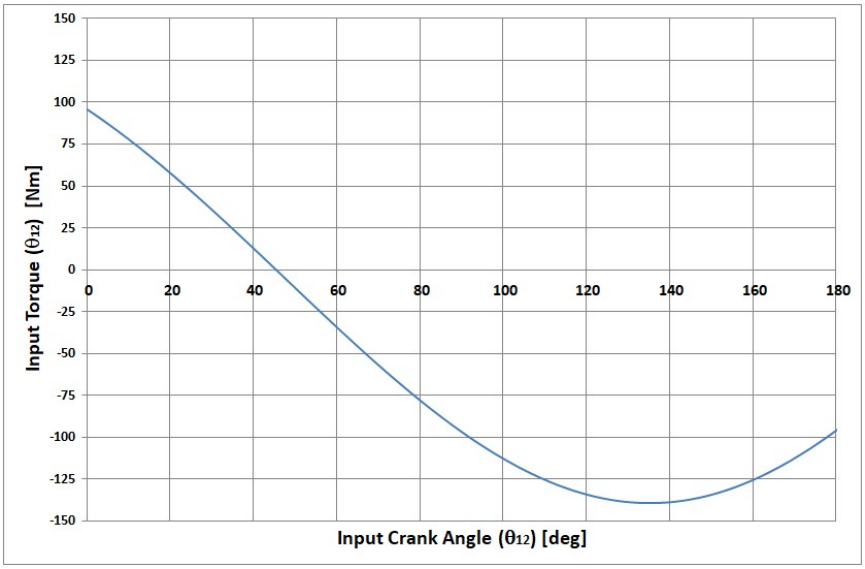

Figure 3.17: Slider-Crank Mechanism Kinematic Pre-Analysis-3

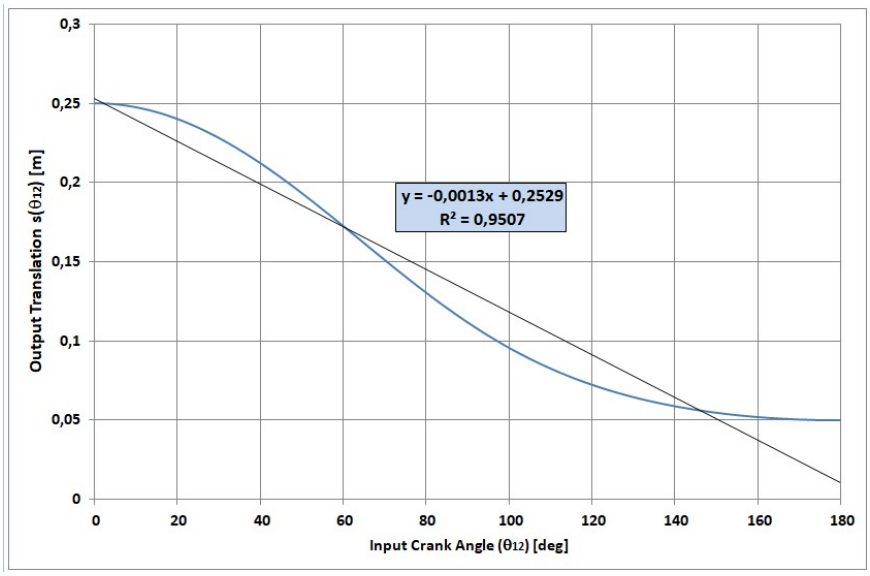

Figure 3.16: Slider-Crank Mechanism Kinematic Pre-Analysis-2

iii. Slider-Crank & Linear Motion Mechanism: In this concept the slider-crank mechanism is used for rotation and the linear actuator for translation of the platform. In Figure 3.18 the conceptual design can be seen. As this concept will be the best solution among others, the reason will be explained in next section, detailed analysis will be explained in the following sections.

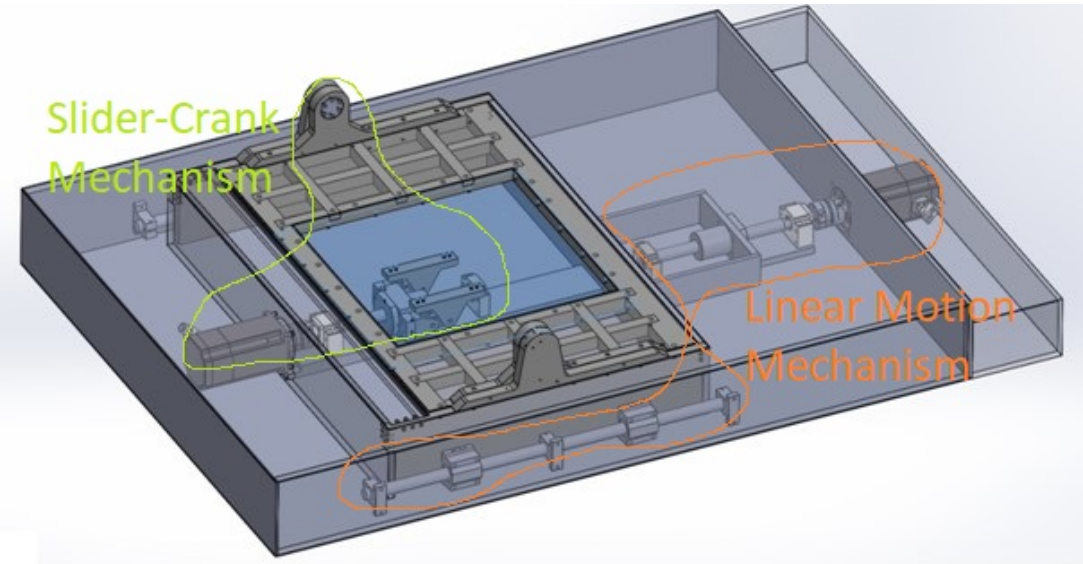

Figure 3.18: Slider-Crank & Linear Motion Mechanism Conceptual Design

iv. Gear Mechanism: In this concept the platform rotation is supplied by a geared power transmission. The motion is produced by a worm gear actuated by an electric motor as given in Figure 3.19. The worm gear drives a large spur gear which is mounted at the bottom of the force plate. This concept has no nonlinearity as only rotating elements are used. However, custom spur gear design is needed for this concept so that the desired rotational motion, in as small as possible volume is achieved. The translating mechanism for this concept was not studied, as the same solution explained in the previous concept, use of linear actuator, was suitable for this one, too.

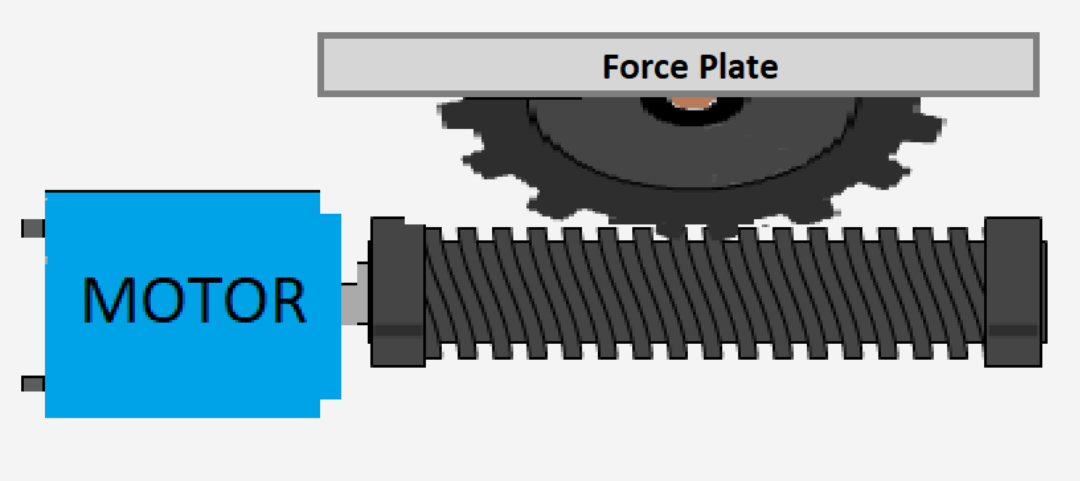

Figure 3.19: Gear Mechanism Conceptual Design

As it is noticeable, the concepts except the Stewart Platform has only one rotational freedom. It was assumed to use the same type mechanism for the other rotatinal axis design. Considering modularity, it was evaluated as more practical.

Comparison criteria were selected as modularity, reliability, cost and height of the design at the end. The evaluation was made according to Pugh's selection method and weighted decision matrix [35].

Before evaluating the concepts, in order to weight the criteria, each criterion was compared with other criteria as presented in Table 3.3. Here, the criterion

Table3.3: Critaria Evaluation

Criteria	Height	Modularity	Reliability	Cost	Design Effort
Height	*	-	-	+	+
Modularity	+	*	+	-	-
Reliability	+	-	*	-	-
Cost	-	+	+	*	-
Design Effort	-	+	+	+	*
Score	2	2	3	2	1
Weight	**0.2**	**0.2**	**0.3**	**0.2**	**0.1**

which is thought to be more important was get a "+" score whereas the less important gets a "-" score. Summing all "+" values at the end the weight of each was determined.

After determining the values of each criterion, the concepts can be evaluated. In Table 3.4 the scores of each concept are presented. The concepts were compared and rated over 3, where 3 is the most desirable score. The "Weighted Score" line expresses the total weighted values for each concept.

The evalutaion suggests to continue with the Slider-Crank Mechanism Concept. The next sections will analyse in detail the design of this concept. As design is an iterative process, the method presented in Figure 3.20 was followed. Here, in finalizing the design, main issue was to end up with a low step height.

All the mechanism analysis were performed in Microsoft Excel.

Table3.4: Concept Evaluation

Criteria/ Concept	Stewart Platform	Four-bar Mechanism	Slider-Crank Mechanism	Gear Mechanism
Height	0	2	3	1
Modularity	0	1	2	1
Reliability	1	2	3	2
Cost	1	3	2	1
Design Effort	1	2	3	2
Weighted Score	**0.6**	**2**	**2.6**	**1.4**

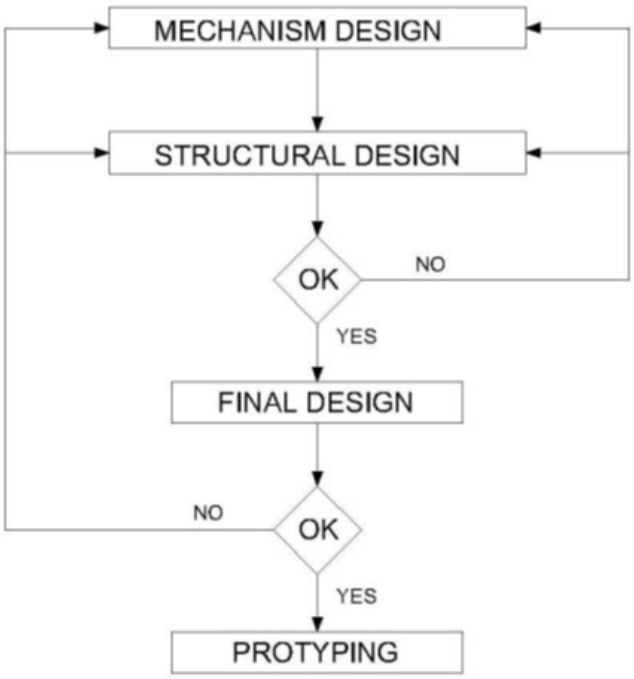

Figure 3.20: Design Method

3.4.1 Platform Tilt/Pitch (AP) Rotation Mechanism

In contrast to the general use of the slider crank mechanism, in this study the slider was used as input link and the crank as the output link. Figure 3.21 shows the general view of the structure.

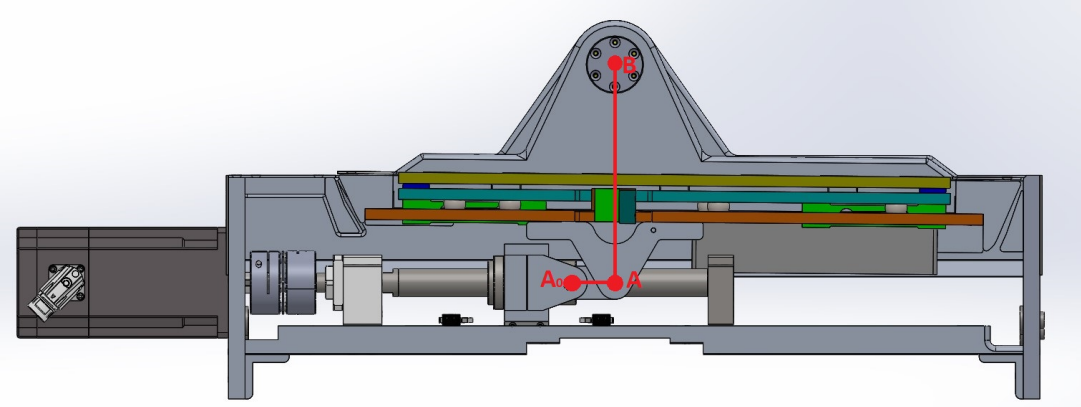

Figure 3.21: Level Position of AP mechanism

3.4.1.1 Kinematic Analysis of Tilt/Pitch (AP) Rotation Mechanism

For kinematic analysis, the links are shown in 2D in Figure 3.22.A_0A is the coupler link, A_0 is the sliding point at which input force is given to the mechanism. AB is the crank link of the mechanism where point B is the fixed pivot point.

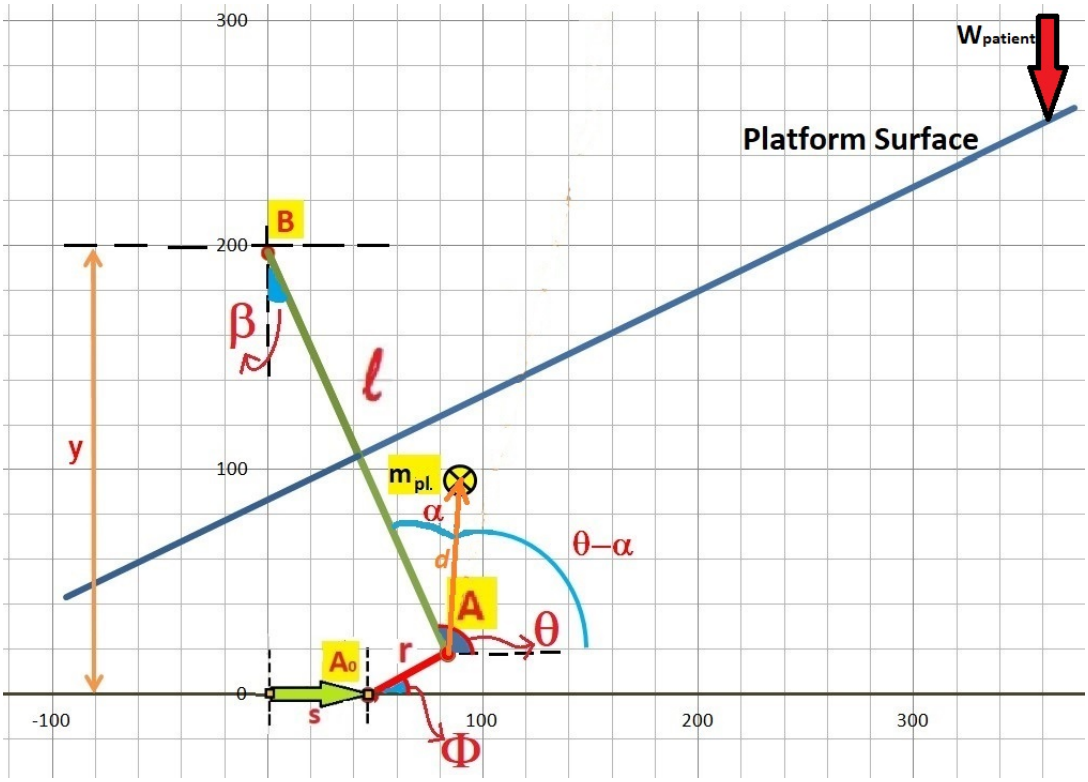

Figure 3.22: 2D view of AP mechanism in Excel

The loop closure equation can be written as;

$$\boldsymbol{A_0A} + \boldsymbol{AB} = \boldsymbol{A_0B} \tag{3.5}$$

The loop closure equation in complex form is;

$$r \cdot e^{i\phi} + l \cdot e^{i\theta} = -s + yi \tag{3.6}$$

where the real part will be;

$$r \cdot \cos(\phi) + l \cdot \cos(\theta) = -s \tag{3.7}$$

and the imaginary part will be;

$$r \cdot \sin(\phi) + l \cdot \sin(\theta) = y \tag{3.8}$$

Taking the square of the real and the imaginary parts and summing them, the following equation can be obtained;

$$Z = s^2 + 2 \cdot s \cdot l \cdot \cos(\theta) = r^2 - y^2 - l^2 + 2 \cdot y \cdot l \cdot \sin(\theta) \tag{3.9}$$

and solving for s;

$$s = \pm\sqrt{Z + l^2 \cdot \cos^2(\theta)} - l \cdot \cos(\theta) \tag{3.10}$$

Eventually, "s" the displacement input of the slider can be calculated for desired angle θ. It should be noticed that the platform rotation angle is directly related to θ, as the link AB is fixed to the rotating platform. The platform inclination or sway angle "β" is then,

$$\beta = 90 - \theta \tag{3.11}$$

The graph in Figure3.23 shows the relation between "s" and "θ". Also it should be noted that there is high linearity between input and output. The equation on the graph is the trendline fitted linearly, and R^2 is the correlation coefficient.

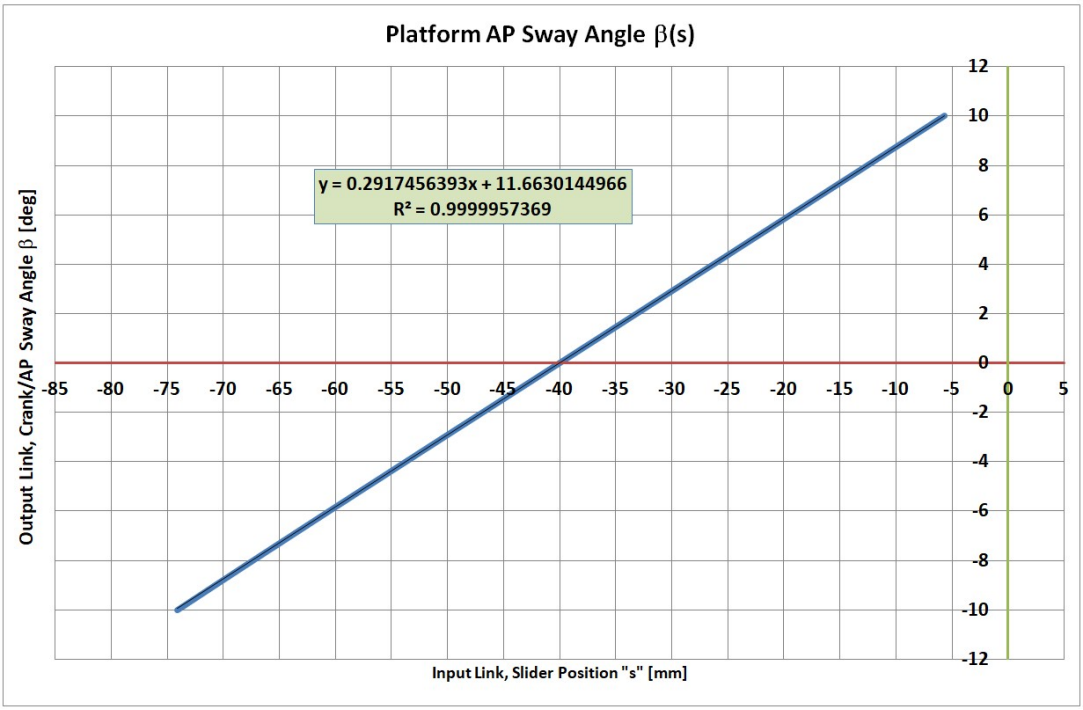

Figure 3.23: Platform Inclination as a Function of Slider Displacement "s"

From Figure 3.23 it has to be noted that for the initial position the slider is at $s = -40\ mm$ where the platform angle $\beta = 0°$. To move the platform in both directions covering the whole range, sliding input $s = \pm 35$ mm has to be given.

The other variable ϕ can also be expressed in terms of θ using the imaginary part of the loop closure equation.

$$\phi = \arcsin\left[\frac{y - l \cdot \sin(\theta)}{r}\right] \tag{3.12}$$

3.4.1.2 Kinetic Analysis of Tilt/Pitch (AP) Rotation Mechanism

In order to continue with the force analysis, motion profiles of the mechanism has to be defined. In this system for AP rotation, the most critical scenario was the Adaptation Test. In this test, the platform has to rotate in AP direction for 8 degrees toes up and 8 degrees toes down. The whole motion, either toes up or toes down, has to take place in 400 ms and the acceleration has to last maximum 50 ms. According to these values, the motion profiles can be drawn as shown in Figure 3.24 and in Figure 3.25.

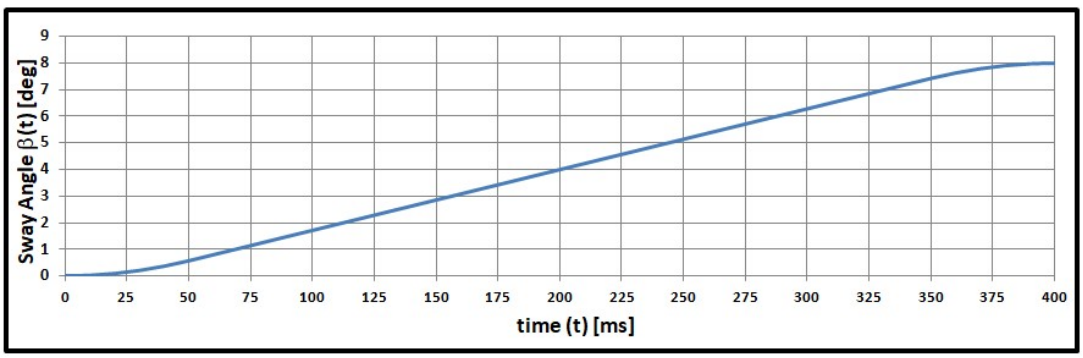

Figure 3.24: Platform AP Sway Angle as a Function of time, "t" [ms]

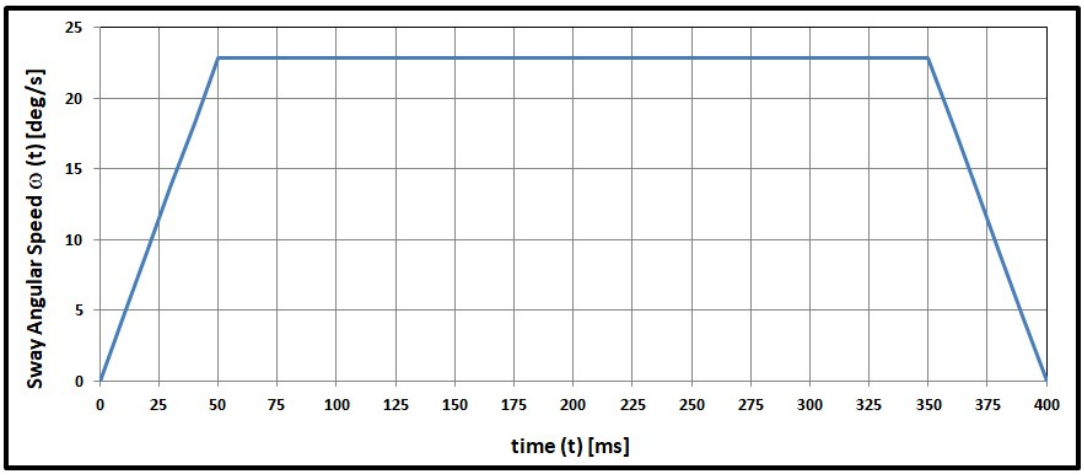

Figure 3.25: Platform AP Sway Angle Speed as a Function of time, "t" [ms]

Now, as the motion profiles are defined, dynamic force analysis can be performed. The loop closure equations were defined earlier, now the velocity and acceleration equations can also be written.

Taking the derivative of function "s" the velocity term "$\dot{s}$" is obtained.

$$s = -\sqrt{r^2 - y^2 - l^2 + 2 \cdot y \cdot l \cdot \sin(\theta) + l^2 \cdot \cos^2(\theta)} - l \cdot \cos(\theta) \tag{3.13}$$

$$\dot{s} = -\frac{1}{2} \cdot \frac{1}{\sqrt{r^2 - y^2 - l^2 + 2 \cdot y \cdot l \cdot \sin(\theta) + l^2 \cdot \cos^2(\theta)}} \cdot (2 \cdot y \cdot l \cdot \cos(\theta) \cdot \dot{\theta} + ...$$

$$... + l^2 \cdot (-2 \cdot \sin(\theta) \cdot \cos(\theta) \cdot \dot{\theta}))) + l \cdot \sin(\theta) \cdot \dot{\theta}$$

$$\dot{s} = -\frac{2 \cdot y \cdot l \cdot \cos(\theta) \cdot \dot{\theta} + l^2 \cdot (-2 \cdot \sin(\theta) \cdot \cos(\theta)) \cdot \dot{\theta}}{2 \cdot \sqrt{r^2 - y^2 - l^2 + 2 \cdot y \cdot l \cdot \sin(\theta) + l^2 \cdot \cos^2(\theta)}} + l \cdot \sin(\theta) \cdot \dot{\theta}$$

In simple form the equation becomes,

$$\dot{s} = -\frac{2 \cdot y \cdot l \cdot \cos(\theta) \cdot \dot{\theta} - l^2 \cdot \sin(2\theta) \cdot \dot{\theta}}{2 \cdot \sqrt{r^2 - y^2 - l^2 + 2 \cdot y \cdot l \cdot \sin(\theta) + l^2 \cdot \cos^2(\theta)}} + l \cdot \sin(\theta) \cdot \dot{\theta} \qquad (3.14)$$

$$\dot{s} = -\frac{N}{D} + l \cdot \sin(\theta) \cdot \dot{\theta}$$

where N and D refers to the numerator and the denominator part of the first term of equation " $\dot{s}$ " .

Taking the derivative of function " $\dot{s}$ " the acceleration equation " $\ddot{s}$ " is obtained.

$$\ddot{s} = -\frac{-2 \cdot y \cdot l \cdot \sin(\theta) \cdot \dot{\theta}^2 + 2 \cdot y \cdot l \cdot \cos(\theta) \cdot \ddot{\theta} - l^2 \cdot \cos(2\theta) \cdot 2 \cdot \dot{\theta}^2}{4 \cdot [r^2 - y^2 - l^2 + 2 \cdot y \cdot l \cdot \sin(\theta) + l^2 \cdot \cos^2(\theta)]} + ...$$

$$... - \frac{l^2 \cdot \sin(2\theta) \cdot \ddot{\theta} \cdot D + N \cdot 2\frac{N}{D}}{4 \cdot [r^2 - y^2 - l^2 + 2 \cdot y \cdot l \cdot \sin(\theta) + l^2 \cdot \cos^2(\theta)]} + ...$$

$$... + l \cdot \cos(\theta) \cdot \dot{\theta}^2 + l \cdot \sin(\theta) \cdot \ddot{\theta} \qquad (3.15)$$

Taking the deraivative of function "ϕ" the angular rate can be expressed.

$$\phi = \arcsin\left[\frac{y - l \cdot \sin(\theta)}{r}\right] \qquad (3.16)$$

$$\dot{\phi} = \left[\frac{\frac{-l}{r} \cdot \cos(\theta) \cdot \dot{\theta}}{\sqrt{1 - (\frac{y - l \cdot \sin(\theta)}{r})^2}}\right] \qquad (3.17)$$

$$\dot{\phi} = \left[\frac{U}{V}\right]$$

Now the acceleration term of the angle "ϕ" can be derived for U and V the numerator and the denominator part of the "$\dot{\phi}$" equation as;

$$\ddot{\phi} = \frac{\left[\frac{l}{r} \cdot \sin(\theta) \cdot \dot{\theta}^2 - \frac{l}{r} \cdot \cos(\theta)\ddot{\theta}\right] \cdot V + ...}{1 - (\frac{y - l \cdot \sin(\theta)}{r})^2}$$

$$\ldots \frac{-U \cdot \frac{1}{2} \cdot \left(1 - (\frac{y - l \cdot \sin(\theta)}{r})^2\right)^{(\frac{-1}{2})} \cdot \left(-2 \cdot (\frac{y - l \cdot \sin(\theta)}{r}) \cdot (\frac{-l}{r}) \cdot \cos(\theta) \cdot \dot{\theta}\right)}{1 - (\frac{y - l \cdot \sin(\theta)}{r})^2} \tag{3.18}$$

With this equation all the motion parameters have been solved. Besides s, $\dot{s}$, $\ddot{s}$ and ϕ, $\dot{\phi}$, $\ddot{\phi}$ from Figure 3.25 maximum value of $\dot{\theta}$ and $\ddot{\theta}$ can be taken as;

$$\dot{\theta} = 30 \ deg/s$$

$$\ddot{\theta} = 600 \ deg/s^2$$

Referring to Figure 3.22 the CoG points of the links have to be determined. For the slider and the coupler it is trivial, the CoG is at the geometric center of the links. But the CoG of the crank link is not at the geometric center of it. After the detailed design process the CoG of the subassembly rotating in AP direction was found.

Lastly, before force analysis, for the crank and the coupler links, the position, velocity and acceleration equations of their CoG can be written.

For the coupler;

$$r_{coupler} = s + \frac{r}{2}[e^{i \cdot \phi}] \tag{3.19}$$

$$v_{coupler} = \dot{s} + \frac{r \cdot i \cdot \dot{\phi}}{2}[e^{i \cdot \phi}] \tag{3.20}$$

$$a_{coupler} = \ddot{s} + \frac{r \cdot i \cdot \ddot{\phi}}{2}[e^{i \cdot \phi}] - \frac{r \cdot \dot{\phi}^2}{2}[e^{i \cdot \phi}] \tag{3.21}$$

$$a_{x,coupler} = \ddot{s} - \frac{r \cdot \ddot{\phi}}{2}[\sin(\phi)] - \frac{r \cdot \dot{\phi}^2}{2}[\cos(\phi)] \tag{3.22}$$

$$a_{y,coupler} = \frac{r \cdot \ddot{\phi}}{2}[\cos(\phi)] - \frac{r \cdot \dot{\phi}^2}{2}[\sin(\phi)] \tag{3.23}$$

For the crank;

$$r_{crank,CG} = s + r \cdot e^{i \cdot \phi} + d \cdot e^{i \cdot (\theta - \alpha)} \tag{3.24}$$

$$v_{crank,CG} = \dot{s} + r \cdot i \cdot \dot{\phi} \cdot e^{i \cdot \phi} + d \cdot \dot{\theta} \cdot i \cdot e^{i \cdot (\theta - \alpha)} \tag{3.25}$$

$$a_{crank,CG} = \ddot{s} + r \cdot i \cdot \ddot{\phi} \cdot e^{i \cdot \phi} - r \cdot \dot{\phi}^2 \cdot e^{i \cdot \phi} + d \cdot \ddot{\theta} \cdot i \cdot e^{i \cdot (\theta - \alpha)} - d \cdot \dot{\theta}^2 \cdot e^{i \cdot (\theta - \alpha)} \tag{3.26}$$

$$a_{x,crank,CG} = \ddot{s} - r \cdot \ddot{\phi} \cdot \sin(\phi) - r \cdot \dot{\phi}^2 \cdot \cos(\phi) - d \cdot \ddot{\theta} \cdot \sin(\theta - \alpha) - d \cdot \dot{\theta}^2 \cdot \cos(\theta - \alpha) \tag{3.27}$$

$$a_{y,crank,CG} = r \cdot \ddot{\phi} \cdot \cos(\phi) - r \cdot \dot{\phi}^2 \cdot \sin(\phi) + d \cdot \ddot{\theta} \cdot \cos(\theta - \alpha) - d \cdot \dot{\theta}^2 \cdot \sin(\theta - \alpha) \tag{3.28}$$

Now, drawing the Free Body Diagrams of each link will show the forces acting on the joints. Friction is neglected.

For the slider an external axial force F_a will be applied by the prime mover. The inertial force $F_{1,inertial}$, ground reaction force G_1 and joint reactions $R_{1,x}$ and $R_{1,y}$ are shown in Figure 3.26.

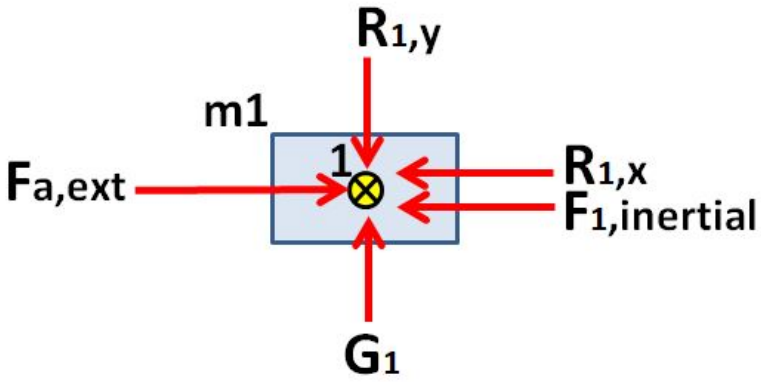

Figure 3.26: Free Body Diagram of The Slider Link

Writing the dynamic equilibrium equations;

For $\sum \boldsymbol{F}_x = 0$;

$$F_a - R_{1,x} - F_{1,inertial} = 0 \tag{3.29}$$

where; $F_{1,inertial} = m_1 \cdot \ddot{s}$.

Then the required force to move the slider will become,

$$F_a = R_{1,x} + m_1 \cdot \ddot{s}$$

In order to find the required external force F_a the value of $R_{1,x}$ has to be known, which will be derived in the following equations of other links.

For $\sum \boldsymbol{F}_y = 0$;

$$R_{1,y} - G_1 = 0 \tag{3.30}$$

And $\sum \boldsymbol{M}_z = 0$. There is no moment acting on the slider.

The Free Body Diagram for the coupler link can be seen in Figure 3.27

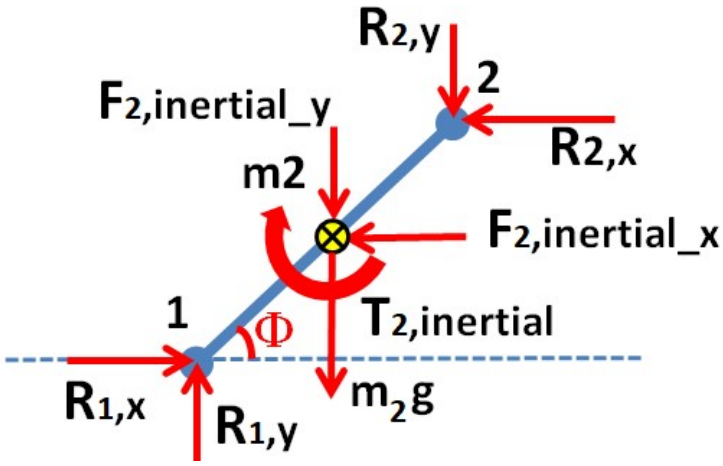

Figure 3.27: Free Body Diagram of The Coupler Link

Writing the dynamic equilibrium equations for the coupler of length $|r|$;

For $\sum \boldsymbol{F}_x = 0$;

$$R_{1,x} - R_{2,x} - F_{2,ix} = 0 \tag{3.31}$$

where; $F_{2,ix} = m_2 \cdot a_{2x}$.

Then,

$$R_{1,x} = R_{2,x} + m_2 \cdot a_{2x}$$

In order to find the value of $R_{1,x}$, $R_{2,x}$ has to be known, which will be derived in the following equations.

For $\sum \boldsymbol{F}_y = 0$;

$$R_{1,y} - R_{2,y} - F_{2,iy} - m_2 \cdot g = 0 \tag{3.32}$$

where $F_{2,iy} = m_2 \cdot a_{2y}$. and $F_{2,ix} = m_2 \cdot a_{2x}$.

Writing the moment equation about joint 1; $\sum \boldsymbol{M_1} = 0$

$$R_{2,x}{\cdot}\sin(\phi){\cdot}r + F_{2,ix}{\cdot}\sin(\phi){\cdot}\frac{r}{2} - F_{2,iy}{\cdot}\cos(\phi){\cdot}\frac{r}{2} - R_{2,y}{\cdot}\cos(\phi){\cdot}r - m_2{\cdot}g{\cdot}\cos(\phi){\cdot}\frac{r}{2} - T_{2,i} = 0 \tag{3.33}$$

where

$$T_{2,i} = I_2 \cdot \ddot{\phi}$$

and

$$I_2 = \frac{1}{12} \cdot m_2 \cdot r^2$$

then solving for $R_{2,y}$;

$$R_{2,y} = -\frac{T_{2,i} + m_2 \cdot g \cdot \cos(\phi) \cdot \frac{r}{2} + F_{2,iy} \cdot \cos(\phi) \cdot \frac{r}{2} - F_{2,ix} \cdot \sin(\phi) \cdot \frac{r}{2} - R_{2,x} \cdot \sin(\phi) \cdot r}{\cos(\phi) \cdot r} \tag{3.34}$$

Finally, the Free Body Diagram for the crank link can be seen in Figure 3.28

Lastly, writing the dynamic equilibrium equations for the crank link of length $|l|$;

For $\sum \boldsymbol{F}_x = 0$;

$$R_{3,x} + R_{2,x} - F_{3,ix} = 0 \tag{3.35}$$

where; $F_{3,ix} = m_{pl} \cdot a_{crank,x}$

For $\sum \boldsymbol{F}_y = 0$;

$$R_{3,y} + R_{2,y} - F_{3,iy} - m_{pl} \cdot \boldsymbol{g} = 0 \tag{3.36}$$

where $F_{3,iy} = m_{pl} \cdot a_{crank,y}$

Writing the moment equation about joint 3;

$$\sum \boldsymbol{M_3} = 0$$

$$R_{2,x}\cdot l\cdot\cos(\theta-\frac{\pi}{2})+R_{2,y}\cdot l\cdot\sin(\theta-\frac{\pi}{2})-F_{3,ix}\cdot\cos(\theta-\frac{\pi}{2})\cdot 120+F_{3,ix}\cdot\sin(\theta-\frac{\pi}{2})\cdot 70+...$$

$$...-(F_{3,iy}+m_{pl}\cdot g)\cdot\cos(\theta-\frac{\pi}{2})\cdot 70-(F_{3,iy}+m_{pl}\cdot g)\cdot\sin(\theta-\frac{\pi}{2})\cdot 120-W_{pt}\cdot\sin(\theta-\frac{\pi}{2})\cdot 100+...$$

$$... - W_{pt} \cdot \cos(\theta - \frac{\pi}{2}) \cdot 370 - T_{3,i} = 0 \tag{3.37}$$

where

$$T_{3,i} = I_3 \cdot \ddot{\beta}$$

and

$$I_3 = m_{pl} \cdot z^2$$

Here z is the distance of m_{pl} to the pivot point.

$$z = \sqrt{[120]^2 + [70]^2}$$

The angle α can be expressed as;

$$\alpha = \arctan\Big[\frac{70}{|l - 120|}\Big]$$

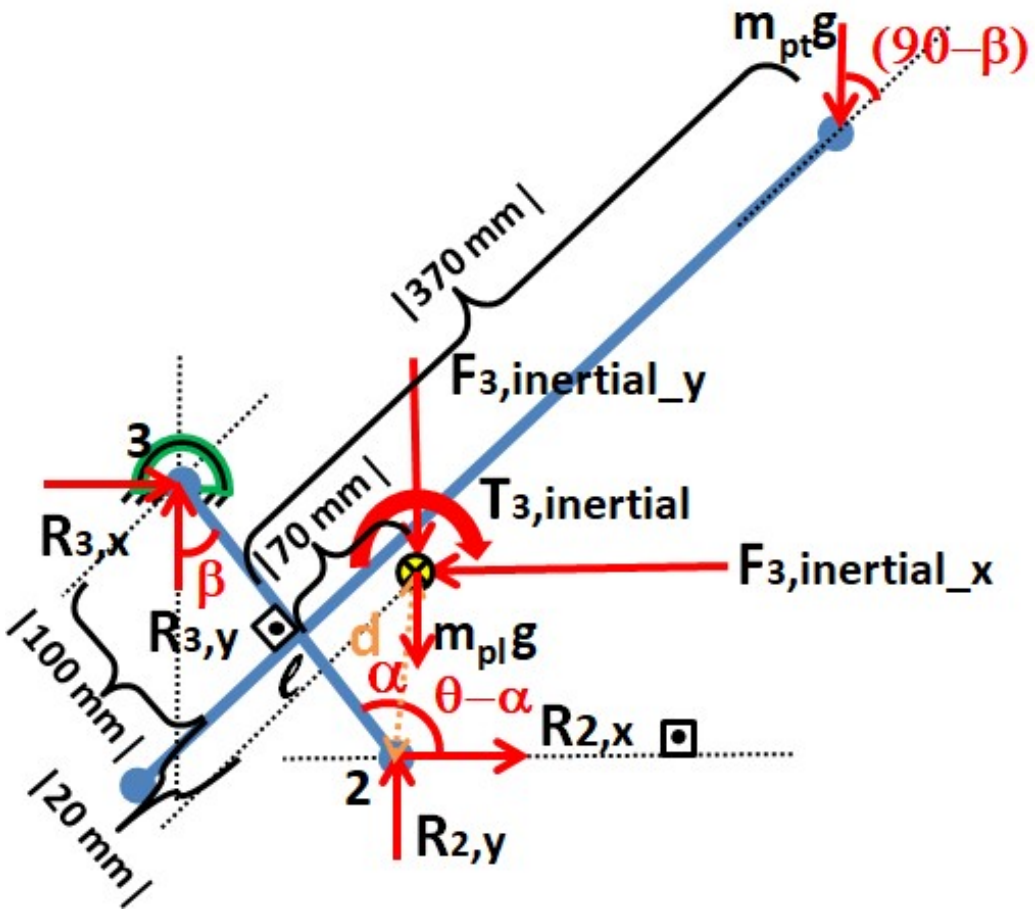

Figure 3.28: Free Body Diagram of The Crank Link

From previos derivations $R_{2,y}$ was found, putting it in the moment equation of the crank link, $R_{2,x}$ can be found; consequently $R_{1,x}$ and finally F_a can be calculated.

3.4.1.3 Machine elements and actutator selection

In previous section all the required equations were derived for force analysis. For the worst scenario, which comes from the design requirements, it was thought that a 140 kg patient with 210 cm height was standing at the tip of the force plate. This scenario will result in the maximum required force input to the mechanism. The specified inputs for the calculations were used and the follow-

ing results were obtained. Figure 3.29 shows the required input force for the accelerating motion in AP direction at any initial angular position i.e. for the whole range, whereas Figure 3.30 expresses the torque required for the motor to supply to the system with a ballscrew lead 10 mm.

The required torque of the electric motor can be found from the following relations.

$$T_{motor} = \frac{h_s \cdot F_{axial}}{2 \cdot \pi \cdot \eta} \tag{3.38}$$

where F_{axial} is the force acting on the slider shown in Figure 3.29, η is the efficiency of the ballscrew and h_s is the lead of the ballscrew.

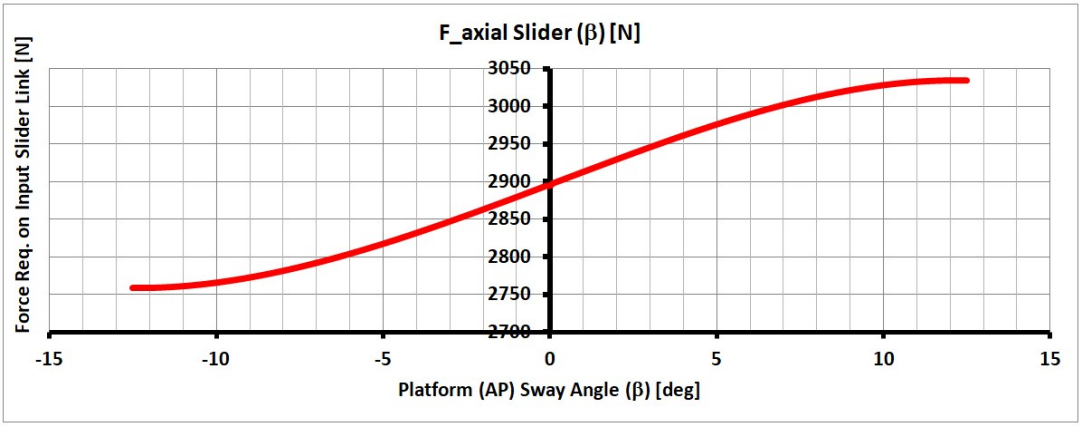

Figure 3.29: Force on the Slider link as a function of Platform Inclination Angle

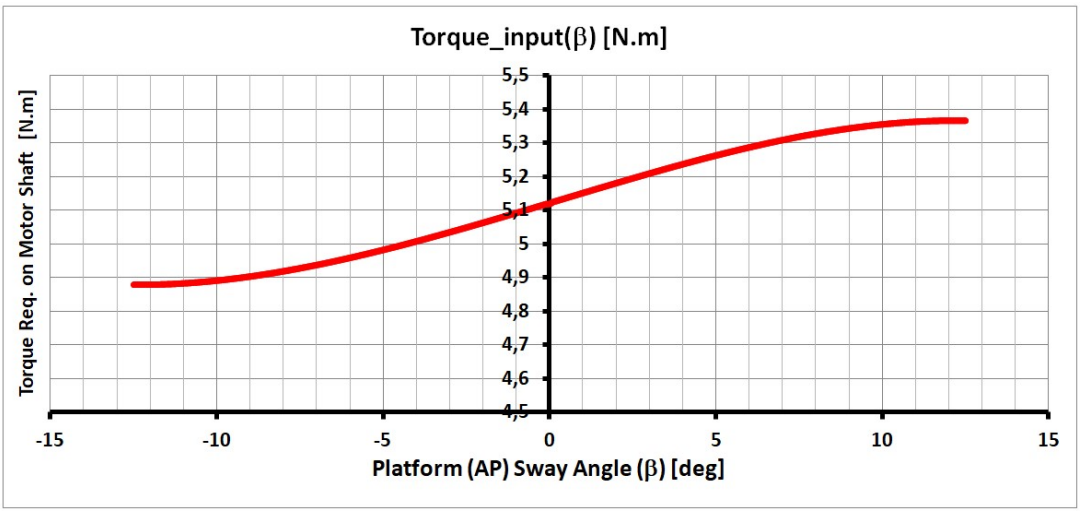

Figure 3.30: Required Torque on Motor Shaft as a function of Platform Inclination Angle

Earlier the sliding input to move the platform over the whole range was determined. With a ballscrew lead $h_s = 10\ mm$, the slider can be moved $s = \pm 35\ mm$ for the following speed;

The maximum speed can be calcuted by;

$$v_{max} = \frac{s}{\frac{1}{2} \cdot t_{acc} + t_{constant} + \frac{1}{2} \cdot t_{dec}} \tag{3.39}$$

where s is the travelled distance, t_{acc} is the acceleration duration, t_{dec} is the deceleration duration, $t_{constant}$ is the time duration for constant speed.

For $s = 35\ mm$, $t_{acc} = 50\ ms$, $t_{dec} = 50\ ms$ and $t_{constant} = 300\ ms$,

$$v_{max} = 0.1 m/s$$

Using the selected ballscrew the rotational speed N_{motor} will be;

$$N_{motor} = \frac{v_{max}}{h_s} = 10 rev/s$$

$$N_{motor} = 600 rpm$$

According to the results a motor supplying at least a 5.5 $N.m$ output nominal torque with 1600 rpm was selected.

After the detailed design, a selection problem arose for the rotation axis points which are supported by pins and bearings presented in Figure 3.31.Considering all the loads that the mechanism carries for all scenarios, a tapered roller bearing was selected. As the AP mechanism subassembly may also rotate in roll direction when ML mechanism is active, the bearings of AP rotation mechanism face with combined loads, i.e. radial and axial. Therefore tapered roller type of bearing was chosen. The load analysis of the pin carrying the mechanism will be shown in next sections.

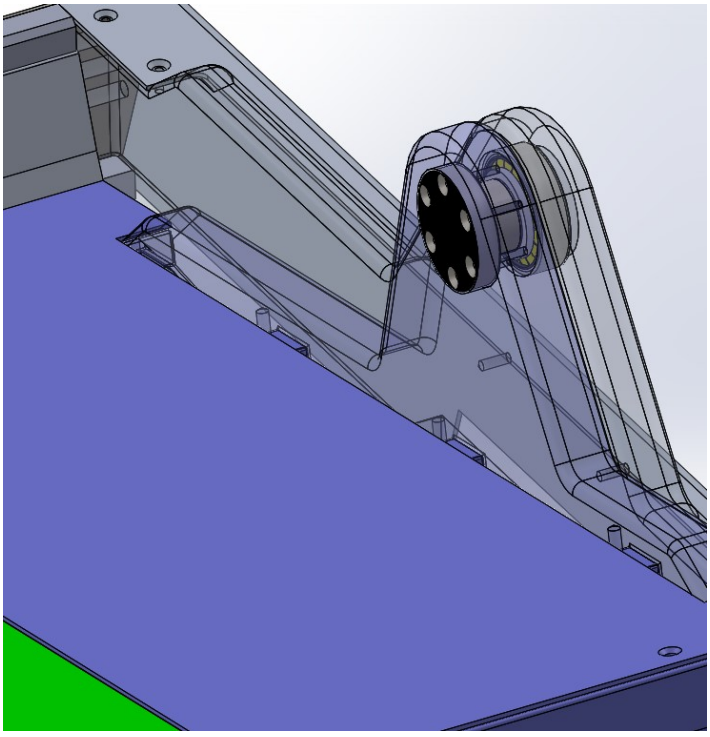

Figure 3.31: AP Rotation Axis, Supported by Pins & Bearings

3.4.2 Platform Roll (ML) Rotation Mechanism

The roll (ML) mechanism of the system is the same as the pitch (AP) rotation mechanism. The slider crank mechanism design was implemented so that, the rotary (ML) motion subassembly (in green) was located on the outer frame of

the pitch mechanism subassembly (in yellow), as presented in Figure 3.32. In Figure 3.33 the designed parts for the second rotation (ML) axis can be seen. In green, the outer frame of the design is presented. The other parts form the driving mechanism with linkages, bearings, ballscrew and motor. The yellow (AP subassembly) structure was mounted to the uncolored parts of the ML structure where these parts form the motion freedom.

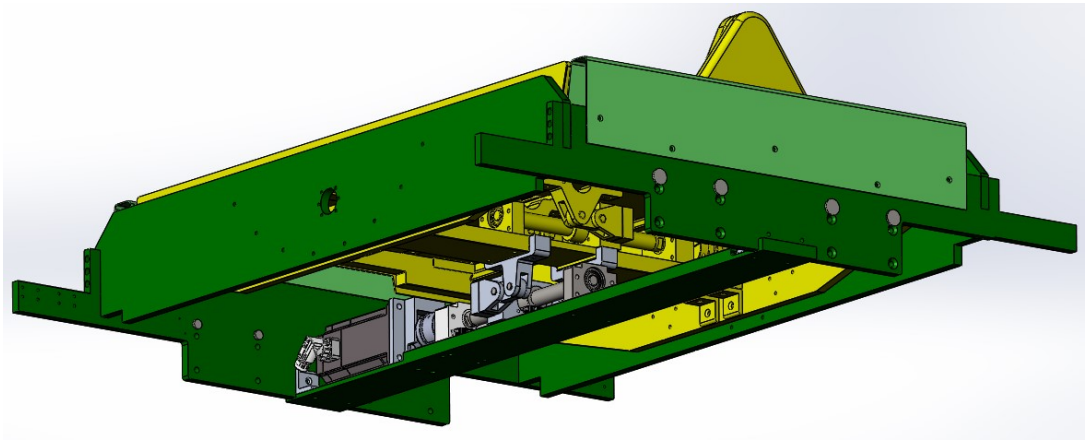

Figure 3.32: ML Rotation Mechanism CAD Model

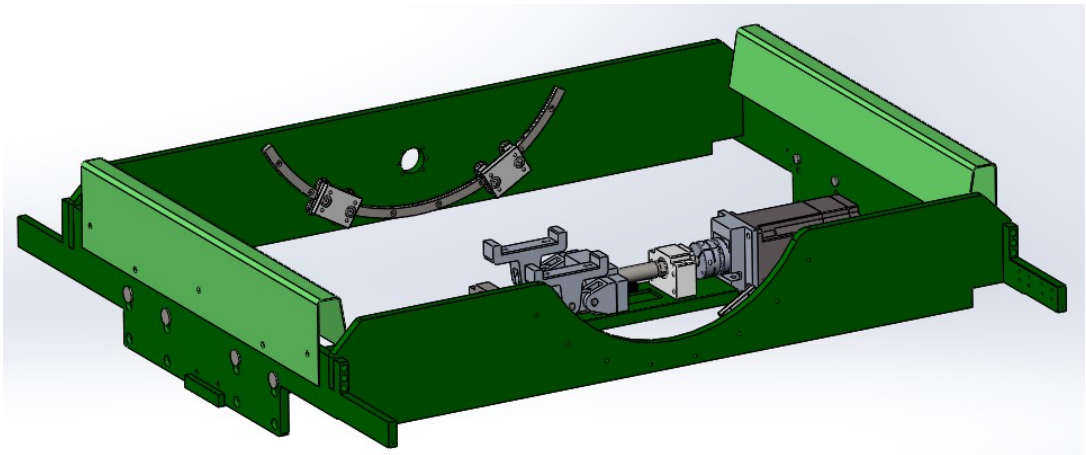

Figure 3.33: ML Rotation Mechanism CAD Model

One important feature of the ML rotation mechanism is that, compared to the AP rotation mechanism, there is no apparent mechanical part related to the

ML rotation axis like pins and bearings on the outside of the platform. In fact, the rotation axis is above the platform but thanks to a special design it can not be identified from outer view. Here, curved guides were used to achieve to locate the rotation axis above the platform. This was also needed considering the scenario while the patient is getting on the platform. Otherwise a bump above the platform could cause the patient to stagger. This is not the case for AP rotation mechanism, as the bearings are placed on two sides of the platform they are not a threat to the patient when stepping onto the platform.

In Figure 3.34 the details of the rotation axis in ML direction can be seen. The center of the circle form the ML rotation axis. It should be noted that the ML rotation axis is at the same height as the AP rotation axis. The curved guides are placed between the outer frame of the ML (in green) structure and the yellow (AP) subassembly.

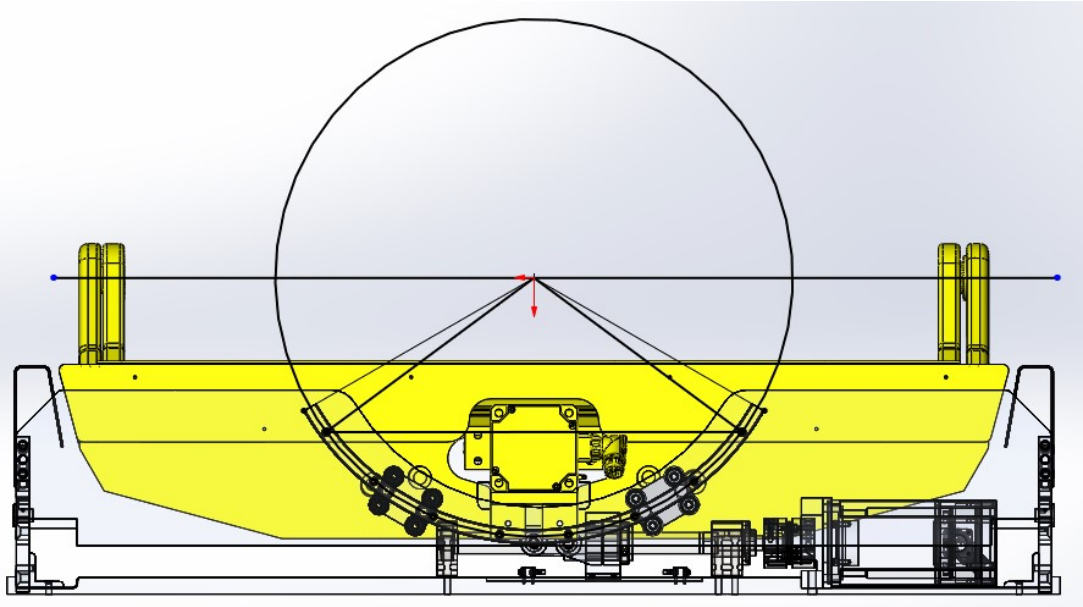

Figure 3.34: ML Rotation Axis

3.4.2.1 Kinematic Analysis of Roll (ML) Rotation Mechanism

In Figure 3.35 the links of the mechanism are shown.

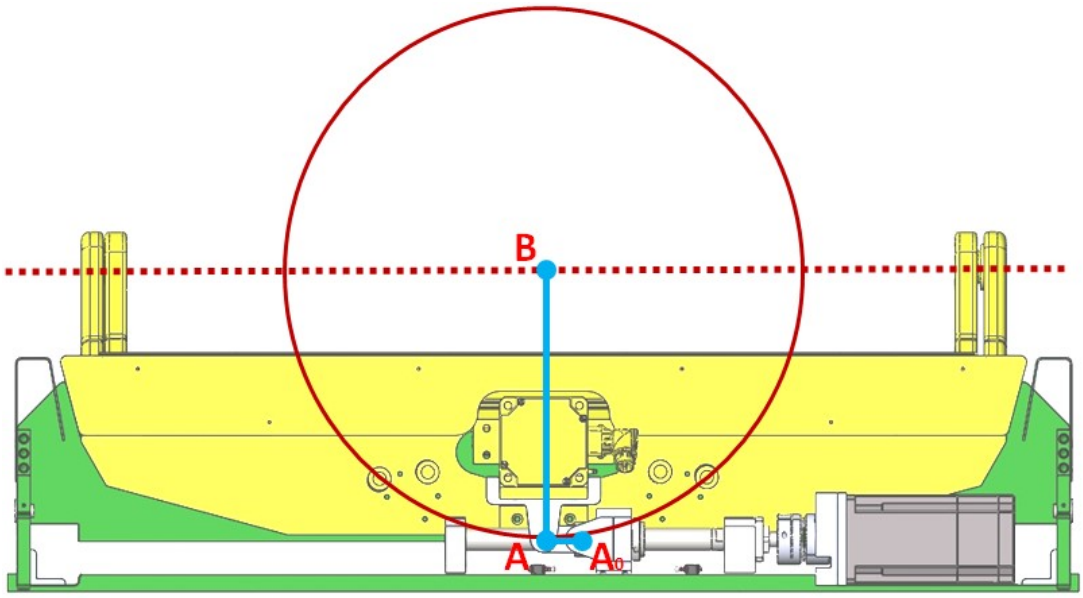

Figure 3.35: ML Rotation Mechanism Links

For kinematic analysis A_0A is the coupler link, A_0 is the sliding point at which input force is given to the mechanism. AB is the crank link of the mechanism where point B is the fixed pivot point. The loop closure equation can be written as;

$$\boldsymbol{A_0A} + \boldsymbol{AB} = \boldsymbol{A_0B} \tag{3.40}$$

It is the same mechanism configuration as in AP rotation; therefore, the kinematic analysis details are not given. However, the dimensions for this solution are not same as the AP rotation mechanism; hence, differences exists in results. The change in the inclination angle as a function of the slider input for ML rotation in both directions is given in Figure 3.36. It can be inferred from the graph that, the slider has to be displaced $\pm 55\ mm$ to rotate the platform in ML direction for the required range.

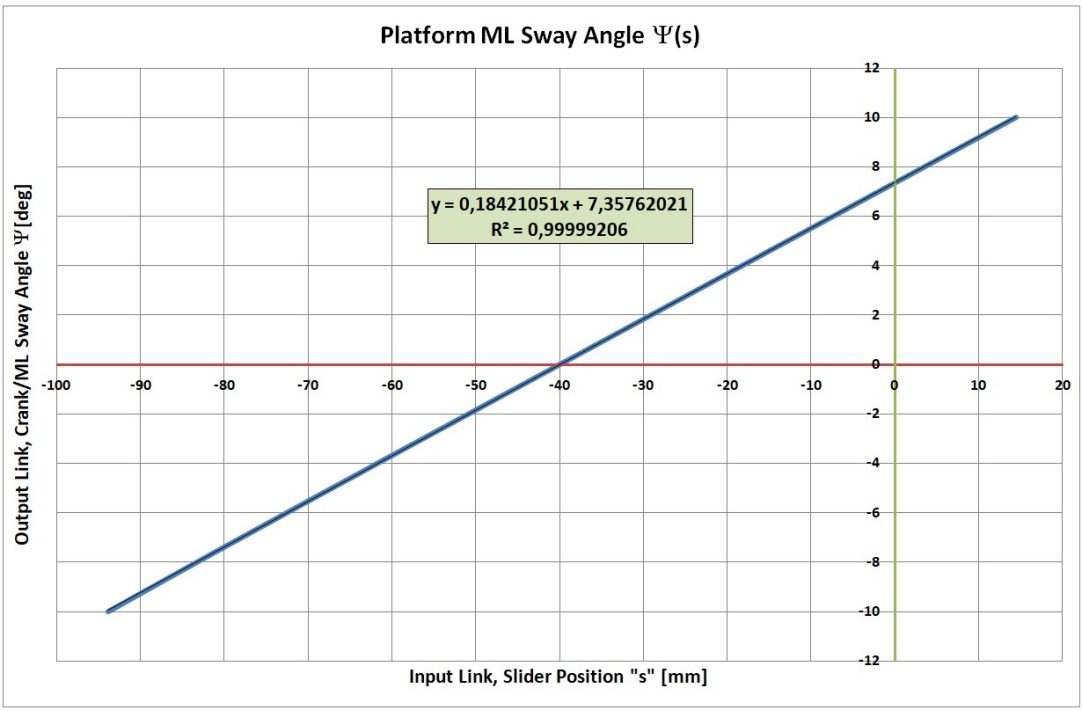

Figure 3.36: ML Inclination Angle as a Function of Slider Displacement "s"

3.4.2.2 Kinetic Analysis of Roll (ML) Rotation Mechanism

It is the same mechanism configuration as in AP rotation; therefore, the kinetic analysis details are not given. Results are explained in the following sections.

3.4.2.3 Machine elements and actutator selection

In previous sections all the required equations were derived for AP mechanism, as it is the same mechanism the same relations can be used for ML rotation mechanism, too. However, the position of the patient standing on the platform will act differently on ML mechanism. Moreover, the link lenghts are also different but the use of Excel enables to modify the results, easily.

For the worst scenario, which comes from the design requirements, it was thought that a 140 kg patient with 210 cm height was standing at the side edge of the

platform as shown in Figure 3.37. This scenario will result in the maximum required force input to the mechanism. The specified inputs for the calculations were used and the following results were obtained:

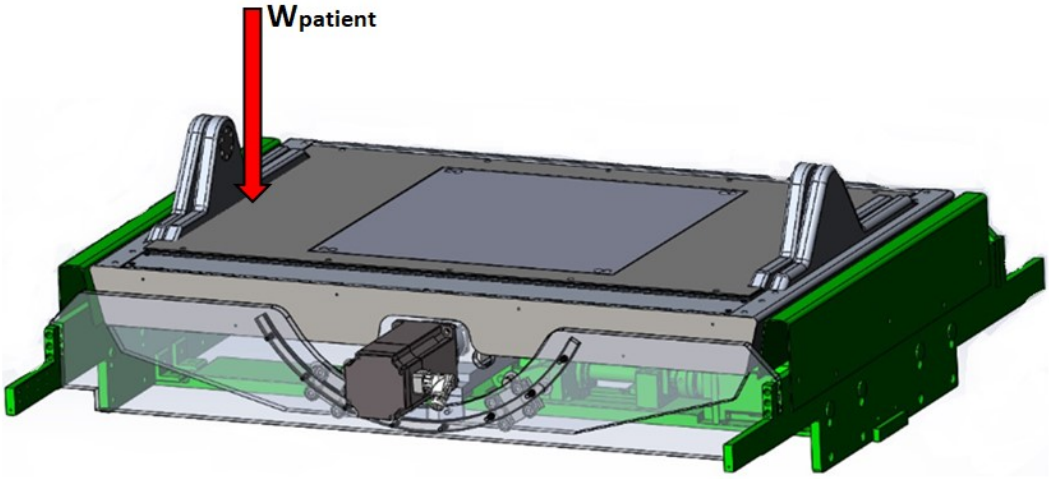

Figure 3.37: Force on the Side Edge of the Platform

Figure 3.38 shows the required input force for the accelerating motion in ML direction at any angular position i.e. for the whole range, whereas Figure 3.39 expresses the torque required for the motor to supply to the system with a ballscrew lead 10 mm.

The required torque of the electric motor can be found from the following relations. It has to be remembered that the computed value is the required input torque where an accelerating motion over the whole motion range was assumed. Different from the motion profiles defined earlier, this assumption enables a wider use for the device for further developments of the device.

$$T_{motor} = \frac{h_s \cdot F_{ML}}{2 \cdot \pi \cdot \eta} \tag{3.41}$$

where F_{ML} is the force acting on the slider shown in Figure 3.38, η is the efficiency of the ballscrew and h_s is the lead of the ballscrew.

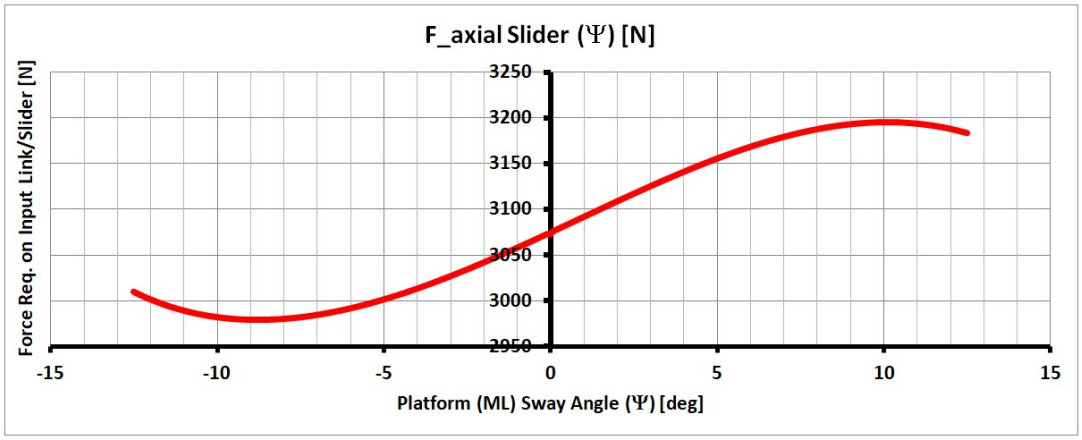

Figure 3.38: Force on the Slider link as a function of Platform Inclination Angle

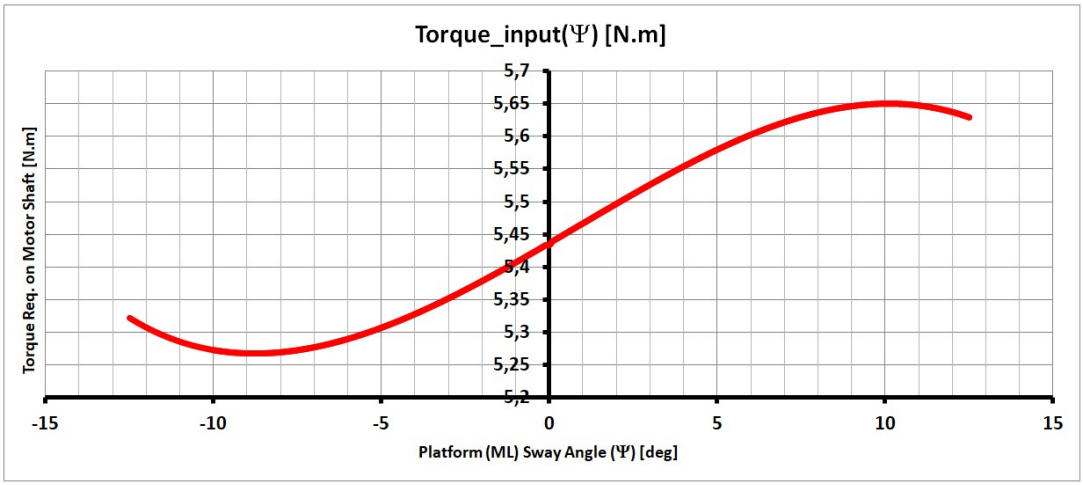

Figure 3.39: Required Torque on Input Shaft of the motor as a function of Platform Inclination Angle

A ballscrew with a 10 mm lead was chosen so that there is a servo motor that can give the required torque and speed.

Earlier the sliding input to move the platform over the whole range was determined. With a ballscrew lead $h_s = 10\ mm$, the slider can be moved $s = \pm 55$ mm with the following speed;

The maximum speed can be calcuted by;

$$v_{max} = \frac{s}{\frac{1}{2} \cdot t_{acc} + t_{constant} + \frac{1}{2} \cdot t_{dec}} \tag{3.42}$$

where s is the travelled distance, t_{acc} is the acceleration duration, t_{dec} is the deceleration duration, $t_{constant}$ is the time duration for constant speed.

For $s = 55$ mm, $t_{acc} = 50$ ms, $t_{dec} = 50$ ms and $t_{constant} = 300$ ms,

$$v_{max} = 0.157\ m/s$$

Using the selected ballscrew the rotational speed N_{motor} will be;

$$N_{motor} = \frac{v_{max}}{h_s} = 15.7\ rev/s$$

$$N_{motor} = 943\ rpm$$

According to the results a motor supplying at least a 5.8 $N.m$ output nominal torque with 1600 rpm was selected.

After the detailed design, considering all the loads that the mechanism carries for all scenarios and the condition where the patient steps on the platform, a bearing that is embedded inside the platform was selected. However, it has to be noted that there are limited options for this component. One reason is that in order to have the swaying ML rotation axis above the platform the bearing has to be curved as presented in Figure3.40. The other limitation is that there are only specific curved guides, having intermittent radius options. So, as one of the goals of the design was getting a low profile platform at the end, the selection of the curved guide was not trivial.

Among the options, tempered curved guides having incresed load capacity was selected. With a 300 mm radius two guides each with two rollers in vertical were placed on the two sides of the platform as shown in Figure 3.37. So, the four rollers on the curved guides carry all the loads including the force plate, the AP rotation subassembly and the patient. For the worst scenario a total load of 2650 N acts on the rollers in radial direction.

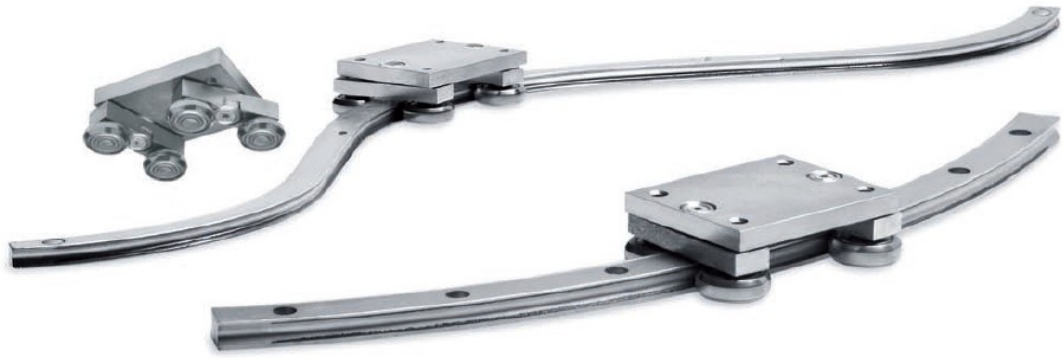

Figure 3.40: Rollon (TM) Curviline Guide

3.4.3 Platform (AP) Translation Mechanism

The translation mechanism was simply formed by a linear actuation system. All the inner subassemblies, the force plate, the AP and ML rotation mechanisms were designed to be placed on the translating linear bearings. Figure 3.41 shows the general view of the subassembly.

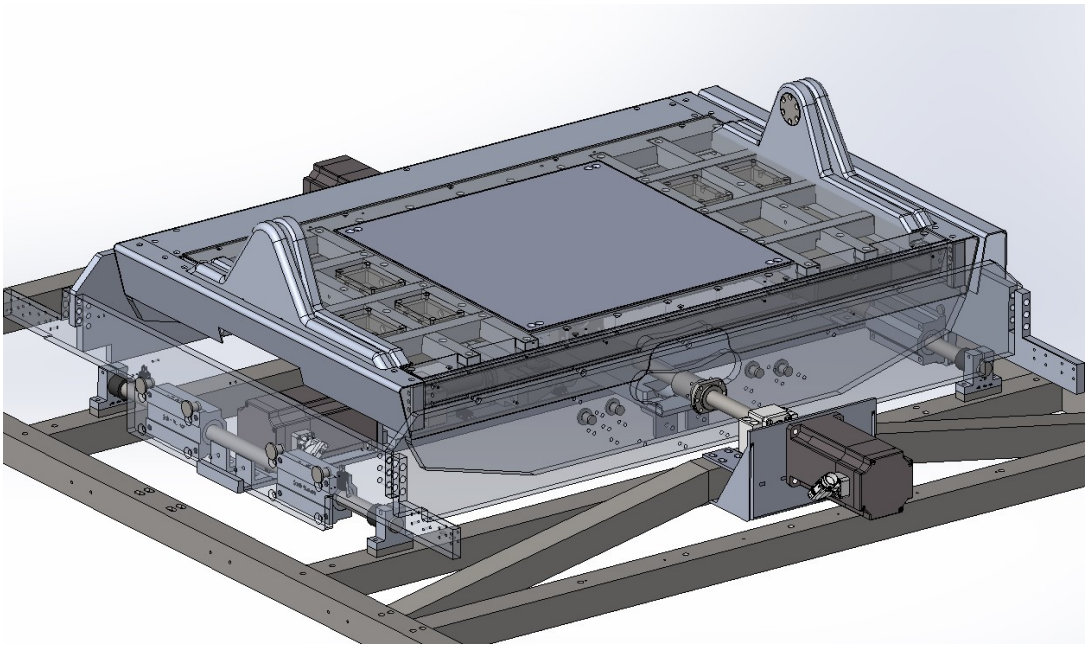

Figure 3.41: Translational Mechanism

The forwards and backwards motion is driven by a ballscrew powered by the servo motor and the whole platform rests on bearings giving the freedom to move, linearly.

3.4.3.1 Kinematic Analysis of (AP) Translation Mechanism

The motion mechanism is simply the ballscrew, driven by an electric motor as shown in Figure 3.42 .

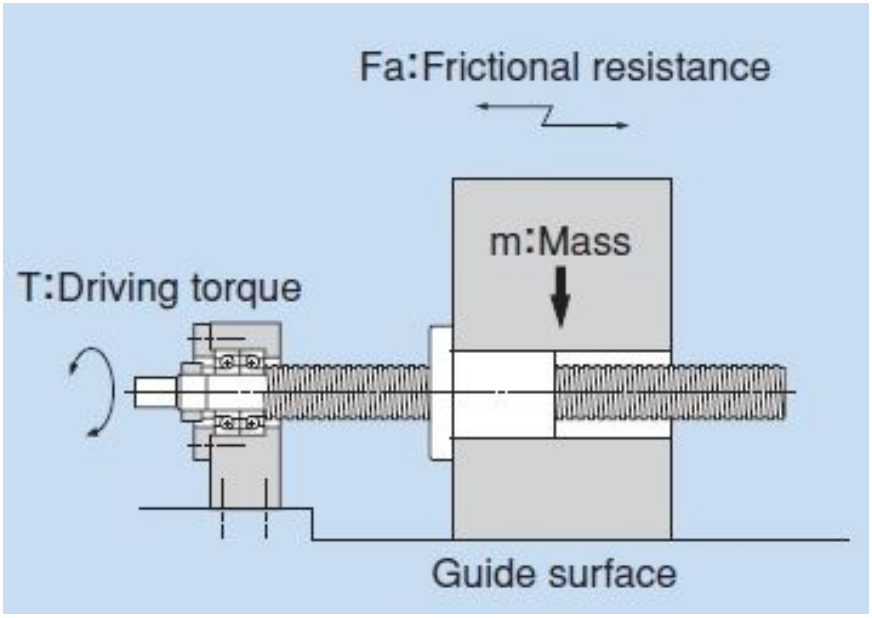

Figure 3.42: Translational Mechanism in 2D

Hence, besides the specific motion profiles which are shown in Figure 3.43 and in Figure 3.44, all the neccessary information to calculate the required torque is the magnitude of mass and friction.

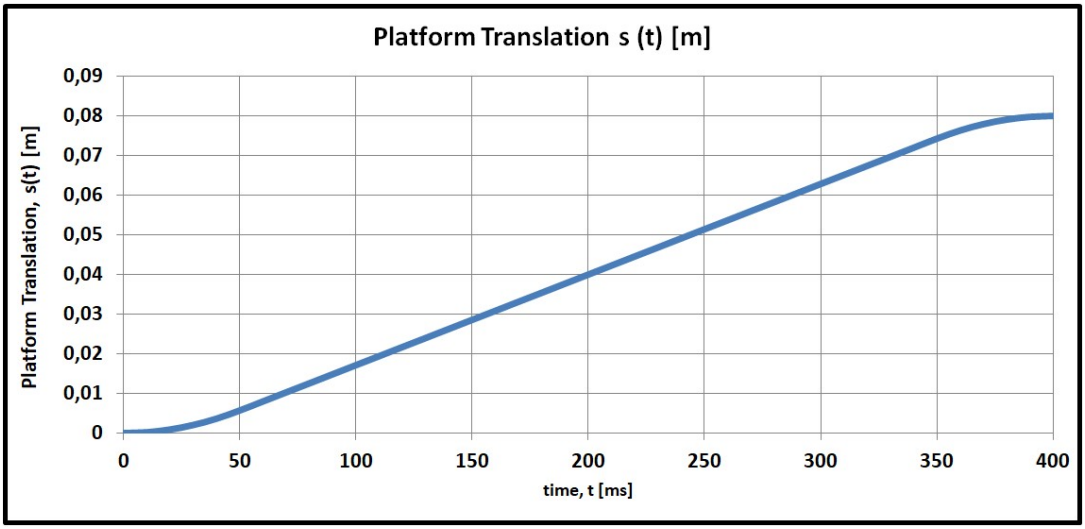

Figure 3.43: Translational Displacement Curve

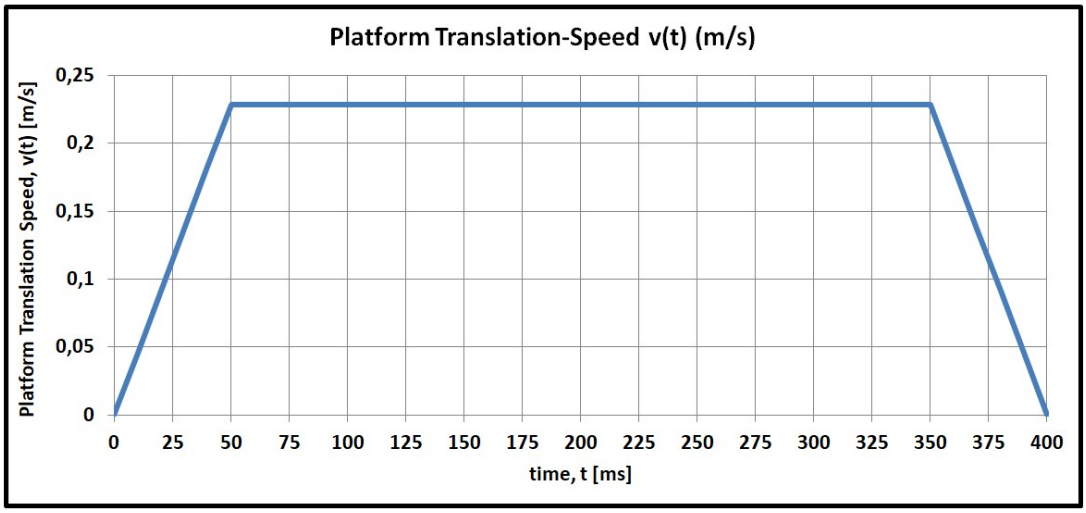

Figure 3.44: Translational Speed Curve

The required motion input can be found from the following relations.

$$s_{displacement} = \frac{\theta_{motor} \cdot h_s}{2 \cdot \pi} \tag{3.43}$$

and for s displacement the required motor rotation can be found from;

$$\theta_{motor} = \frac{s_{displacement} \cdot 2 \cdot \pi}{h_s} \tag{3.44}$$

where θ_{motor} is the magnitude of motor shaft rotation and h_s is the lead of the ballscrew. Hence,

$$\dot{s}_{displacement} = \dot{\theta}_{motor} \cdot \frac{h_s}{2 \cdot \pi} \tag{3.45}$$

and the motor speed can be found from the following relation;

$$\dot{\theta}_{motor} = \dot{s}_{displacement} \cdot \frac{2 \cdot \pi}{h_s} \tag{3.46}$$

3.4.3.2 Kinetic Analysis of (AP) Translation Mechanism

The required torque of the electric motor can be found from the following relations.

$$T_{motor} = \frac{h_s \cdot F_{tr}}{2 \cdot \pi \cdot \eta} \tag{3.47}$$

where F_{tr} is the inertial and friction forces, η the efficiency of the ballscrew.

The maximum power input will be required for forward or backward acceleration. During forward acceleration F_{tr} will be;

$$F_{tr} = m_{translating} \cdot a_{translation} + \mu \cdot m_{translating} \cdot g \tag{3.48}$$

3.4.3.3 Machine elements and actutator selection

After the detailed design process the total mass of the translating assembly came out to be 180 kg, considering the patient on the platform with 140 kg, total mass that translates will be 320 kg. So, each bearing has to carry about 785 N. An analysis on the carrying rod was done which will be shown in next sections. According to the analysis the inner diameter of the bearing came out to be 25 mm. Hence, looking at the load ratings of the linear bearing, compared to the worst scenario with 785 N load capacity, the selected bearing can carry a dynamic 1560 N load which is about two times higher than the requirement.

For the selected ballscrew with a 10 mm lead, load analysis can be done to specify the requirements of the motor. In Figure 3.44 the speed profile was shown. The maximum speed can be calcuted by;

$$v_{max} = \frac{s}{\frac{1}{2} \cdot t_{acc} + t_{constant} + \frac{1}{2} \cdot t_{dec}} \tag{3.49}$$

where s is the travelled distance, t_{acc} is the acceleration duration, t_{dec} is the deceleration duration, $t_{constant}$ is the time duration for constant speed.

For $s = 8\ cm$, $t_{acc} = 50\ ms$, $t_{dec} = 50\ ms$ and $t_{constant} = 300\ ms$,

$$v_{max} = 0.23\ m/s$$

Using the selected ballscrew the rotational speed N_{motor} will be;

$$N_{motor} = \frac{v_{max}}{h_s} = 22.86\ rev/s$$

$$N_{motor} = 1372\ rpm$$

As during acceleration it will be maximum, using the equations derived earlier the required torque came out to be $T_{motor} = 3.65\ N.m$.

The electric motor was selected for minimum $T_{motor} = 3.65\ N.m$ and minimum $N_{motor} = 1372\ rpm$. An AC servo motor with 3000 rpm speed and 5 $N.m$ torque was selected satisfying the requirements. For motion control, the 18-bit encoder was thought to be suffiecent, conveniently.

3.4.4 Visual Surround (AP) Rotation Mechanism

The visual input to the patient was given by rotating the surround. The rotation motion was given by a linear actuator positioned behind the scene. As shown in Figure 3.45 the whole visual surround structure (in orange) is rotated about a point in line with the AP rotation axis, only at a higher position. Two small

pins, extending from the harness bars build the rotating axis. The rotary motion is given by the linear actuator (in blue) which has also the ability to rotate about its fixture points.

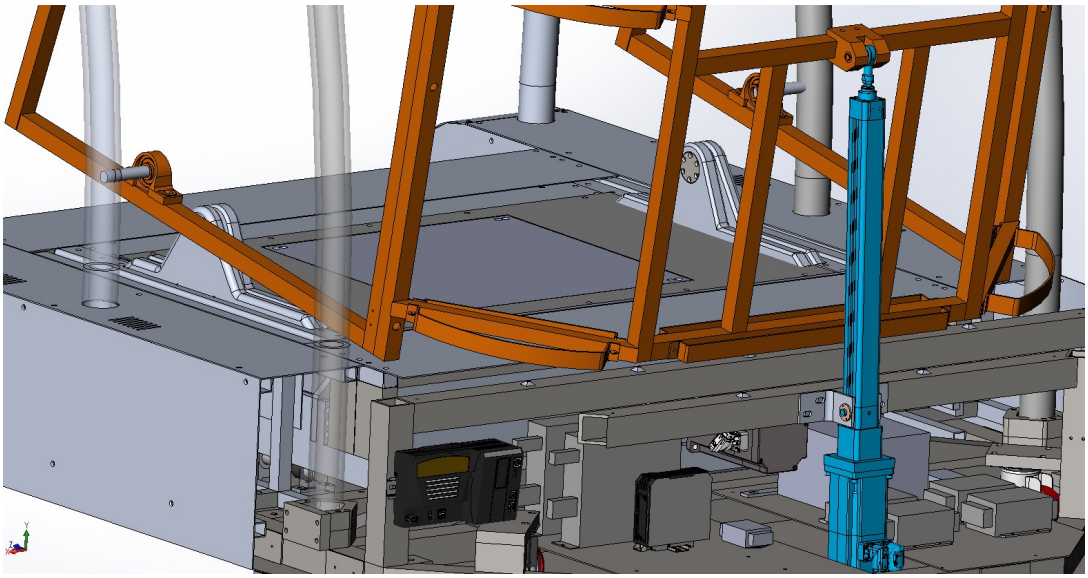

Figure 3.45: Back View of the Visual Surround Mechanism

3.4.4.1 Kinematic Analysis of Visual Surround (AP) Rotation Mechanism

For the motion mechanism, Figure 3.46 shows the 2D sketch of the linkages. The loop closure equation can be written as;

$$\boldsymbol{A_0A} = \boldsymbol{A_0B} + \boldsymbol{BA} \tag{3.50}$$

in complex form;

$$r \cdot e^{i\theta} = -yi + x + s \cdot e^{i\phi} \tag{3.51}$$

where the real part will be;

$$r \cdot cos(\theta) = x + s \cdot cos(\phi) \tag{3.52}$$

and the imaginary part will be;

$$r \cdot sin(\theta) = -y + s \cdot sin(\phi) \tag{3.53}$$

"s" can be solved by taking the square of the real and imaginary parts and summing them. The following relation can be calculated for "s" for desired visual surround rotation θ.

$$s = \sqrt{[y \cdot sin(\theta) - x \cdot cos(\theta)] \cdot 2 \cdot r + r^2 + x^2 + y^2} \tag{3.54}$$

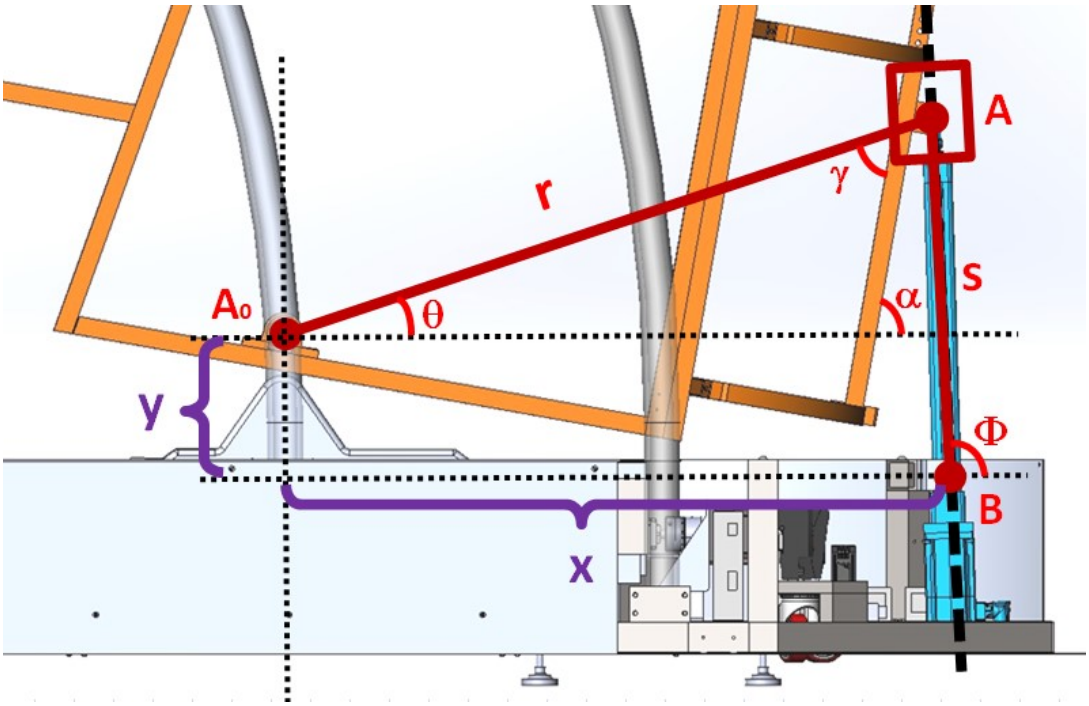

Figure 3.46: Visual Surround Rotation Mechanism in 2D

It should be noted that the rotational position of the visual surround is denoted by α; where

$$\alpha = \theta + \gamma \tag{3.55}$$

γ is a fixed angle formed by the geometry of the visual surround. Hence, with the control of the value of θ, the position of the visual surround can be controlled.

The relation between input "s" and output "α' can be seen from the following Figure 3.47. Like the other mechanisms, the linearity of the visual surround mechanism is also at a sufficient level.

The mechanism was designed so that the initial position of the visual surround was 90 degrees. The required stroke length for the linear actuator denoted by "s" can be deduced from the plot about 370 mm.

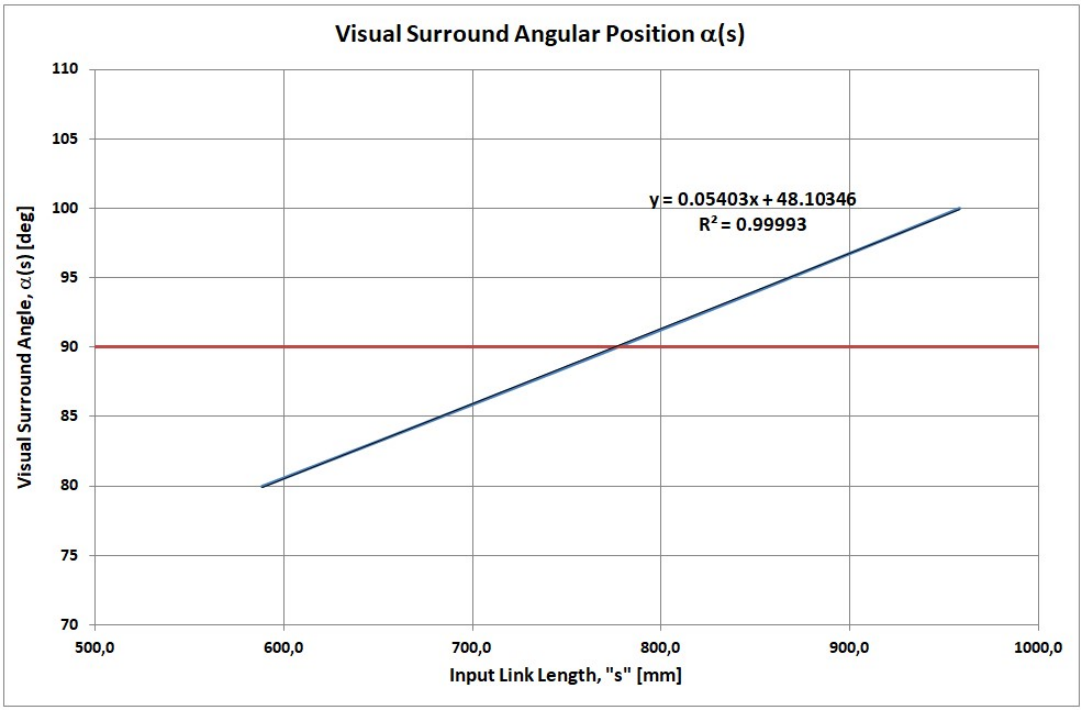

Figure 3.47: Visual Surround Rotation Mechanism Input-Output Plot

The CoG of the Visual Surround is denoted with z_{vs}. The velocity and acceleration expressions of the link can be derived as following;

$$z_{vs} = (r - d) \cdot [e^{i \cdot \theta}] \tag{3.56}$$

$$v_{vs} = (r - d) \cdot i \cdot \dot{\theta} \cdot [e^{i \cdot \theta}] \tag{3.57}$$

$$a_{vs} = (r - d) \cdot i \cdot \ddot{\theta} \cdot [e^{i \cdot \theta}] - (r - d) \cdot \dot{\theta}^2 \cdot [e^{i \cdot \theta}] \tag{3.58}$$

$$a_{x,vs} = -(r - d) \cdot \ddot{\theta} \cdot [\sin(\theta)] - (r - d) \cdot \dot{\theta}^2 \cdot [\cos(\theta)] \tag{3.59}$$

$$a_{y,vs} = (r - d) \cdot \ddot{\theta} \cdot [\cos(\theta)] - (r - d) \cdot \dot{\theta}^2 \cdot [\sin(\theta)] \tag{3.60}$$

The motion profiles of the visual surround defined according to the requirements are drawn in Figure 3.48 Figure 3.49

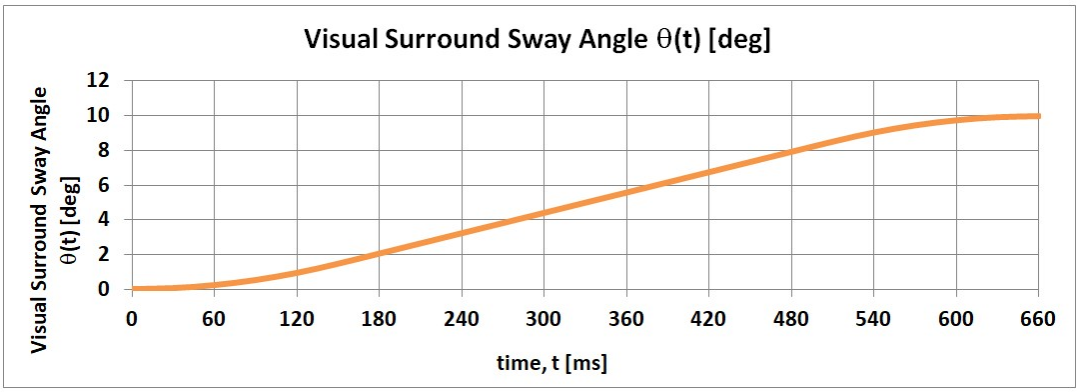

Figure 3.48: Visual Surround Rotational Position Plot

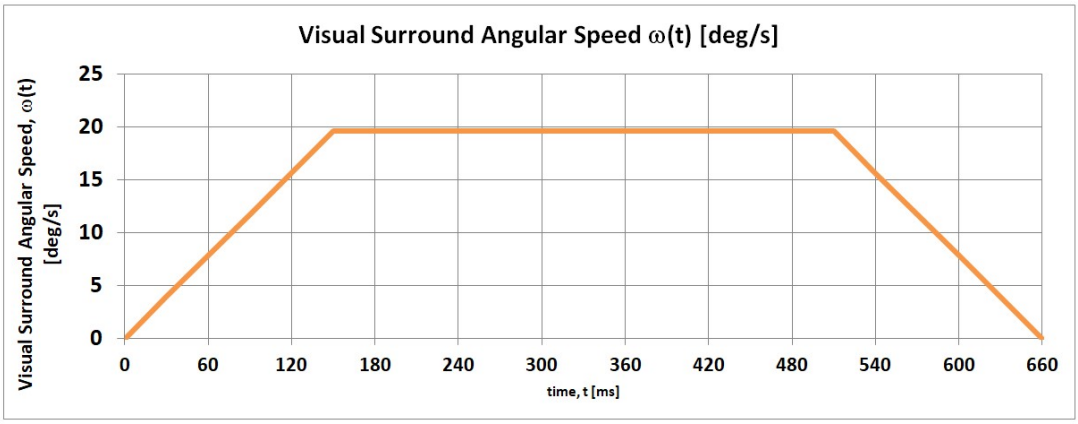

Figure 3.49: Visual Surround Angular Speed Plot

3.4.4.2 Kinetic Analysis of Visual Surround (AP) Rotation Mechanism

For the two links of the visual surround mechanism, the free body diagrams were drawn as in Figure 3.50 and Figure 3.51.

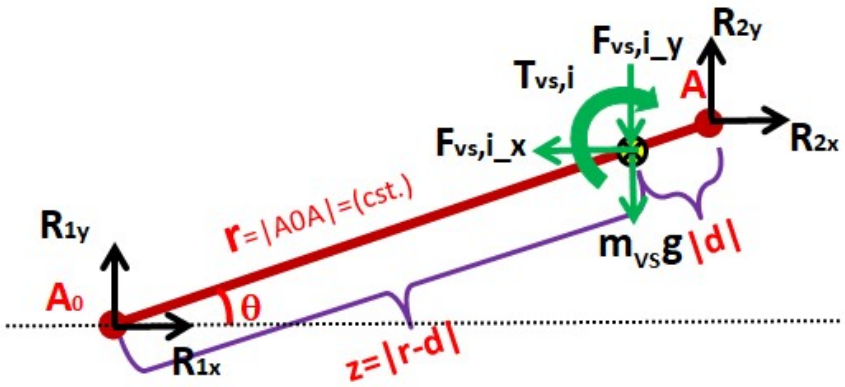

Figure 3.50: Visual Surround Rotation Mechanism Link A_0A

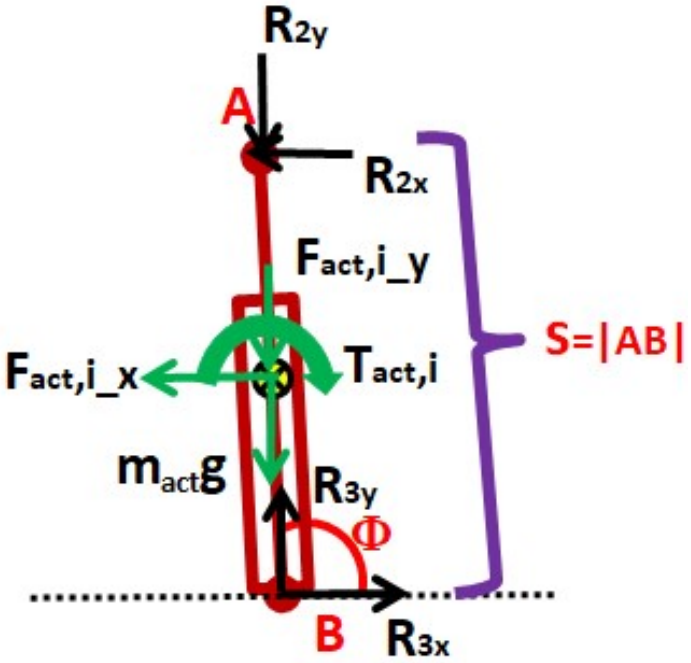

Figure 3.51: Visual Surround Rotation Mechanism Link AB

In order to find the required torque to actuate the mechanism two moment equations are written for each link. Moment equation for link A_0A at point A_0;

for $\sum \boldsymbol{M}_{A_0} = 0$;

$$(m_{vs}\cdot g - F_{y_i,vs})\cdot\cos(\theta) - F_{x_i,vs}\cdot(r-d)\cdot sin(\theta) + R_{2x}\cdot\cos(\theta) - R_{2y}\cdot r\cdot\sin(\theta) - T_{vs,i} = 0 \tag{3.61}$$

where $T_{vs,i} = I_{vs}\cdot\ddot{\theta}$, $F_{x_i,vs} = m_{vs}\cdot a_{x,vs}$ and $F_{y_i,vs} = m_{vs}\cdot a_{y,vs}$

Moment equation for link AB at point B;

for $\sum \boldsymbol{M}_B = 0$;

$$\frac{1}{2}\cdot m_{act}\cdot g\cdot\cos(\pi-\phi) + R_{2x}\cdot s\cdot\sin(\pi-\phi) + R_{2y}\cdot s\cdot\cos(\pi-\theta) - T_{act,i} = 0 \tag{3.62}$$

Solving both moment equations R_{2x} and R_{2y} can be expressed as;

$$R_{2x} = -\frac{m_{act}\cdot g\cdot 0.5\cdot s\cdot\cos(\pi-\phi) + \frac{m_{vs}\cdot g\cdot(r-d)\cdot\cos(\theta) - I\cdot\ddot{\theta}}{r\cdot\sin(\theta)}\cdot s\cdot\cos(\pi-\phi)}{s\cdot\sin(\pi-\phi) + \cot(\theta)\cdot s\cdot\cos(\pi-\phi)} \tag{3.63}$$

$$R_{2y} = \frac{m_{vs}\cdot g\cdot(r-d)\cdot\cos(\theta) + R_{2x}\cdot r\cdot\cos(\theta) - I\cdot\ddot{\theta}}{r\cdot\sin(\theta)} \tag{3.64}$$

As the components of R_2 are derived, the thrust that the actuator to supply can be calculated. It has to be noticed that, the inertial forces for link AB (the actuator) are neglected as they are relatively small.

3.4.4.3 Machine elements and actutator selection

The Visual Surround assembly came out to be approximately 60 kg. After the detailed design the whole Visual Surround structure was placed on three points where two of which are the rotating axis formed by bearings and one point is the actuator connection point. The actuator selection depended on the load and speed requirements. The expressions of load input required to move the Visual Surround were derived in the previous section. The speed of the actuator to give the rotation can be found as;

$$v_{max} = \frac{s}{\frac{1}{2} \cdot t_{acc} + t_{constant} + \frac{1}{2} \cdot t_{dec}} \tag{3.65}$$

where s is the travelled distance, t_{acc} is the acceleration duration, t_{dec} is the deceleration duration, $t_{constant}$ is the time duration for constant speed.

From Figure 3.52 the change of the angle of the visual surround with respect to the stroke of the actuator can be seen. Also the speed graph of the actuator is plotted in Figure 3.53.

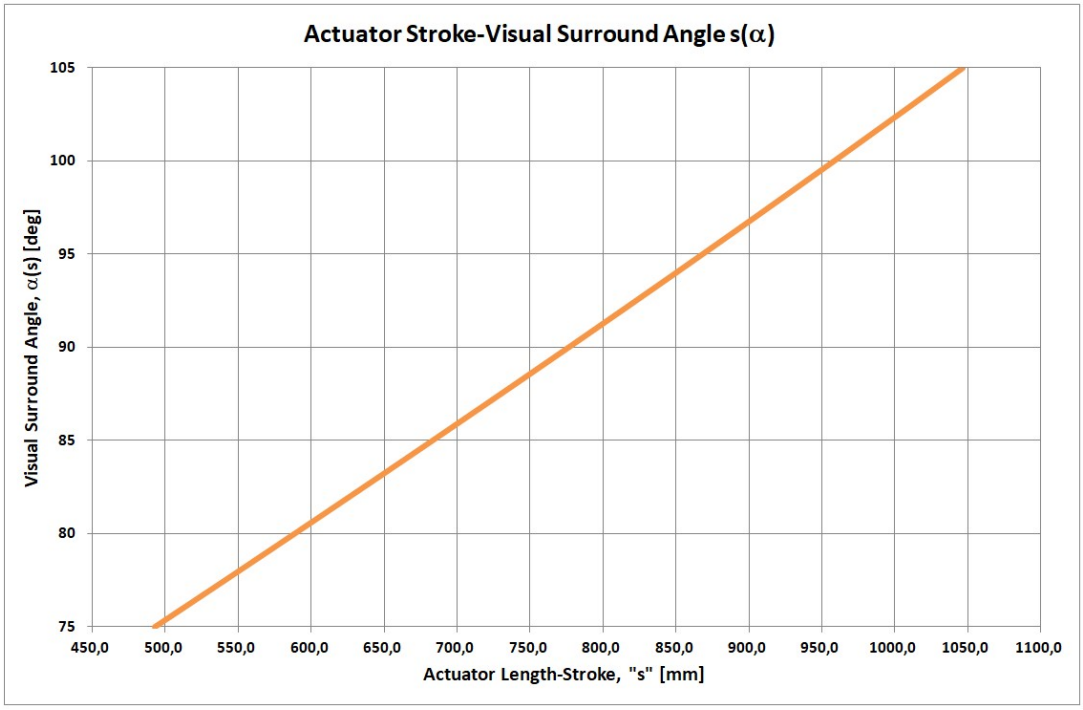

Figure 3.52: Visual Surround Angle-Actuator Stroke

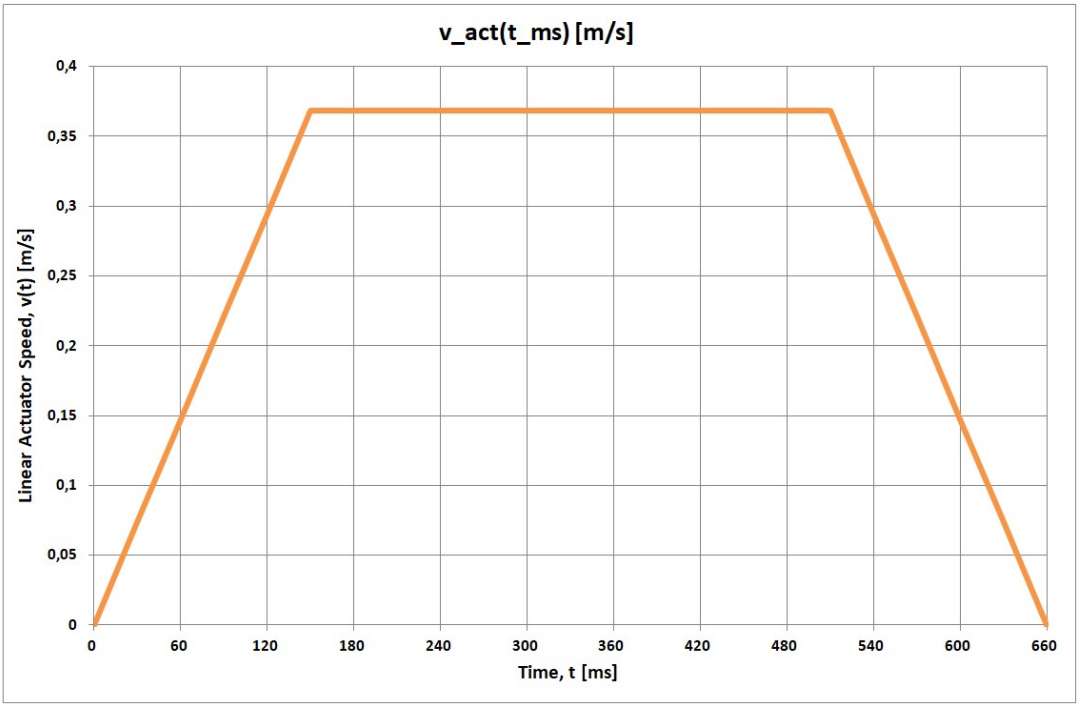

Figure 3.53: Visual Surround Mechanism-Actuator Speed

For $s = 188\ mm$, $t_{acc} = 150\ ms$, $t_{dec} = 150\ ms$ and $t_{constant} = 360\ ms$,

$$v_{max} = 0.37\ m/s$$

Using lead of $h_s = 10\ mm$ for the linear actuator, the rotational speed N_{motor} will be;

$$N_{motor} = \frac{v_{max}}{h_s} = 36.84\ rev/s$$

$$N_{motor} = 2211\ rpm$$

Using the lengths and mass distributions as results of the detailed design process, the expressions derived in the previous section to determine the reaction forces of the mechanism joint R_2 is shown in Figure 3.54. Choosing a linear actuator with a lead of $h_s = 10\ mm$ the torque requirement will be as in Figure 3.55.

The required torque for the electric motor can be found from the following relations.

$$T_{motor} = \frac{h_s \cdot F_{act}}{2 \cdot \pi \cdot \eta} \tag{3.66}$$

where F_{act} is the plotted force in Figure 3.54, η the efficiency of the actuator.

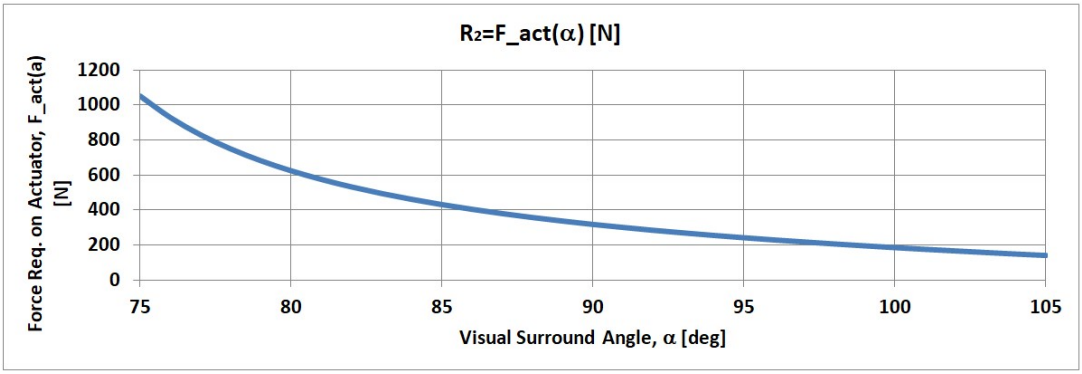

Figure 3.54: Actuator Force required to move the Visual Surround

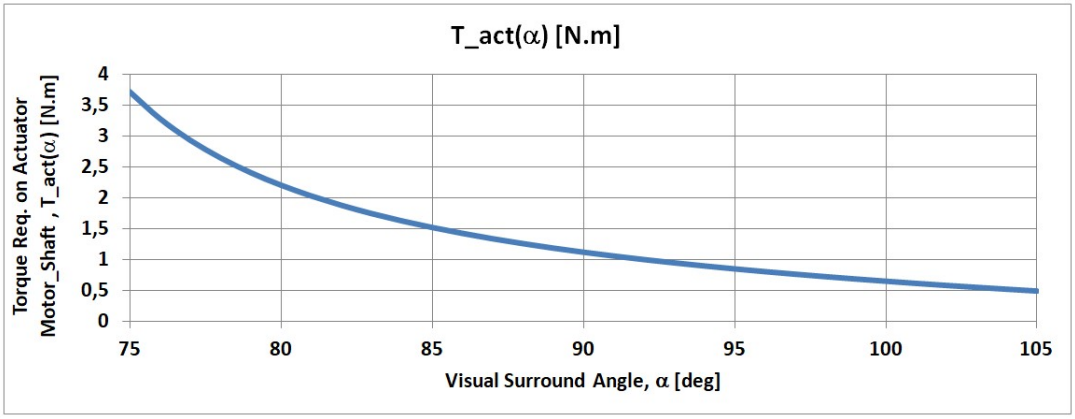

Figure 3.55: Actuator Torque as a function of Visual Surround Angular Position

Hence, an actuator having at least a $2 \cdot s = 2 \cdot 370 = 740\ mm$ stroke, $N_{act} = 2211$ rpm speed and $T_{act} = 2.5\ N.m$ would be sufficient. Considering these results, an AC servo motor with nominal 3000 rpm speed and 2.7 $N.m$ torque was selected.

The linear actuator products may limit the performance criteria; therefore, selection parameters speed, acceleration, stroke, axial force and repeatability capabilities have examined.

As it is easier to mount them on profile sturucture, a standard bearing with housing was selected as shown in Figure 3.56. The sizing of the bearing was related to the pin diameter which will be shown in later section.

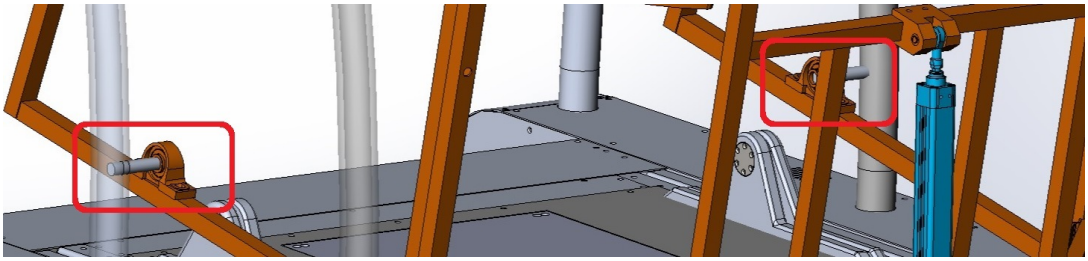

Figure 3.56: Pillow Bearings

3.5 Mechanical Structure Design

In this section the mechanical structure will be in focus. The subassemblies and the critical parts will be analysed and the interfaces between different subassemblies will be shown.

3.5.1 Platform AP (Tilt/Pitch) Rotation Subassembly

The AP rotation subassembly consists of the Force Plate and the rotation mechanism. The details of the Force Plate was explained in Section 3.3. The mechanism links (in purple) are shown in Figure 3.57. In order not to have load only on the fasteners, the geometry of the link interfacing with the bottom of the force plate was designed so that the forces are flowing through the designed mechanical structure. The mechanical interface of the rotation mechanism to the force plate can be seen in the section view in Figure 3.58

The platform rotation in both directions are limited with the limit switches at

± 10 *deg* positions as shown in Figure 3.59 and in Figure 3.60.

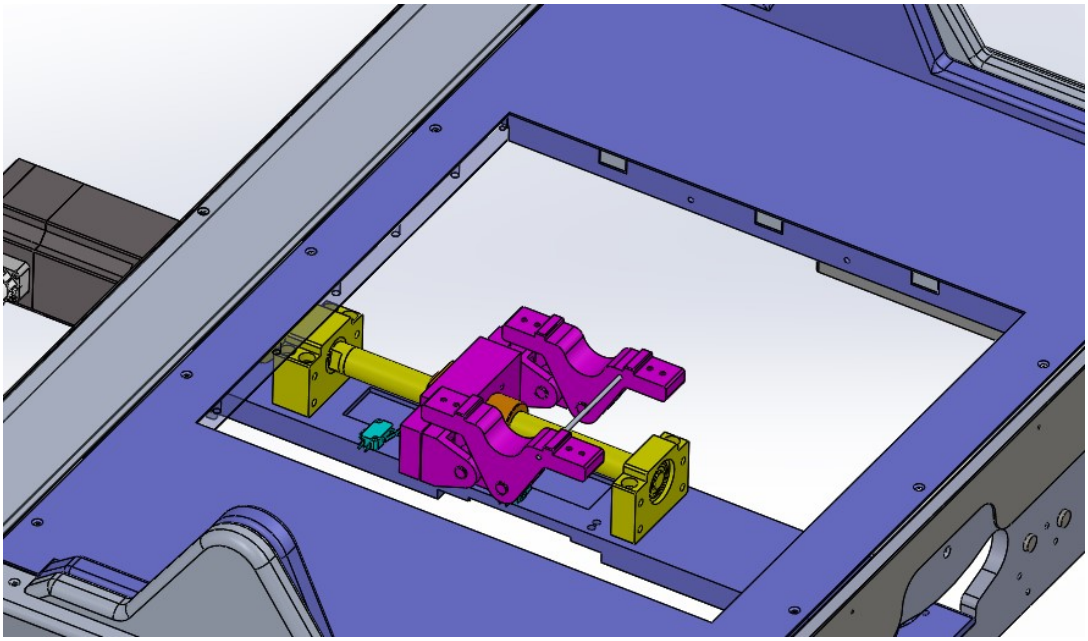

Figure 3.57: AP Rotation Mechanism Links

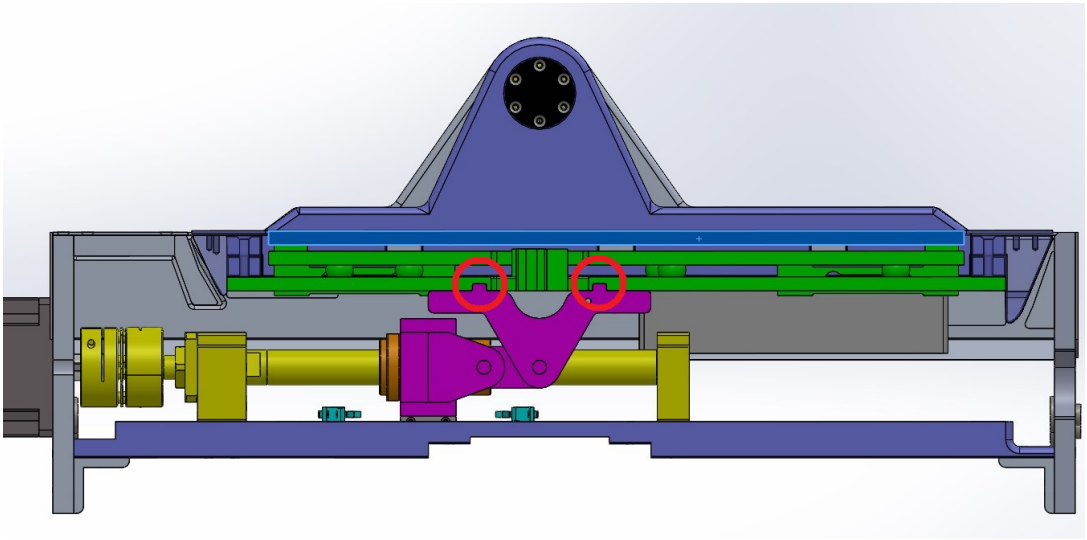

Figure 3.58: Force Plate-AP Rotation Mechanism Interface

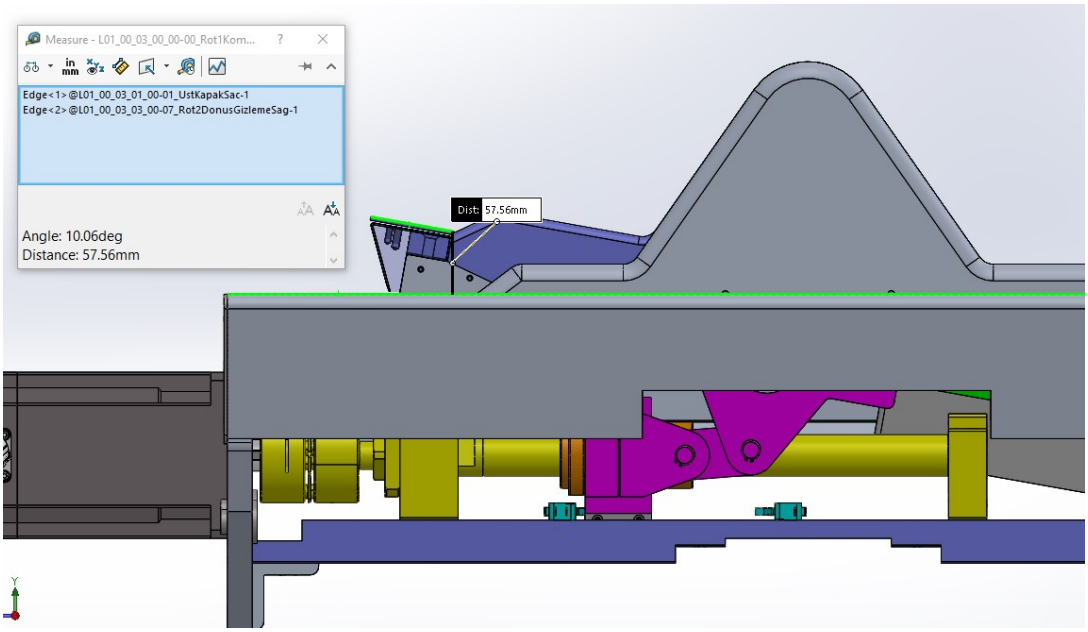

Figure 3.59: AP Rotation at Toes Down (-10 deg) Limit

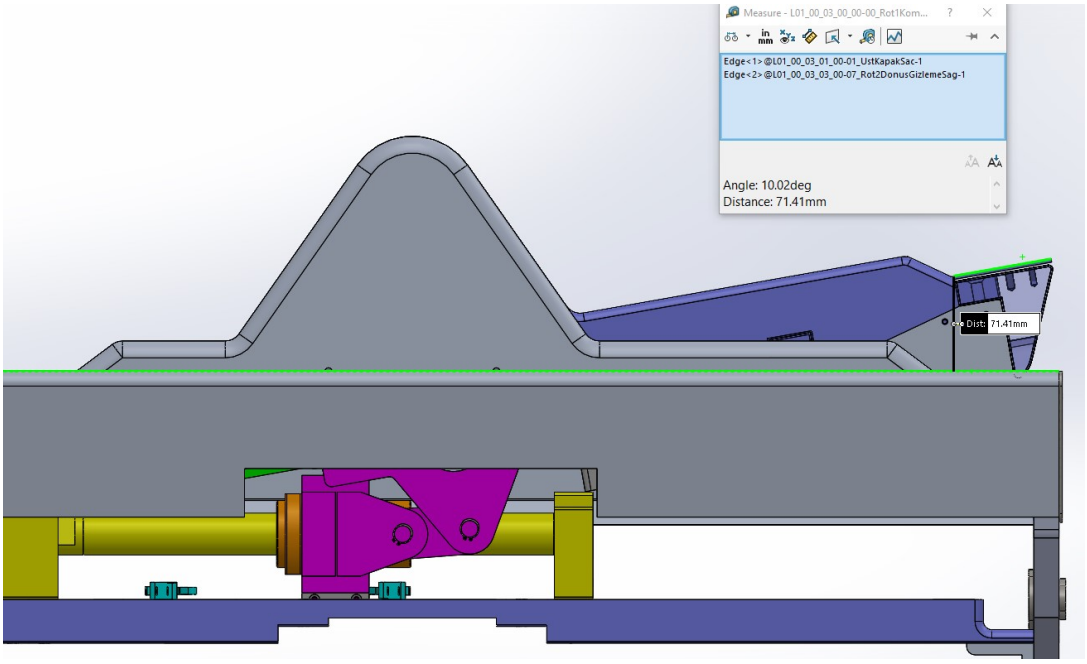

Figure 3.60: AP Rotation at Toes Up (+10 deg) Limit

The section view of the connection of AP Rotation Subassembly (green) with

ML mechanism (purple) is shown in Figure 3.61. The crank link of the ML mechanism was mounted to the part where the ballscrew of the AP mechanism was fixed. The connections of curved guides were described earlier in Section 3.4.2.

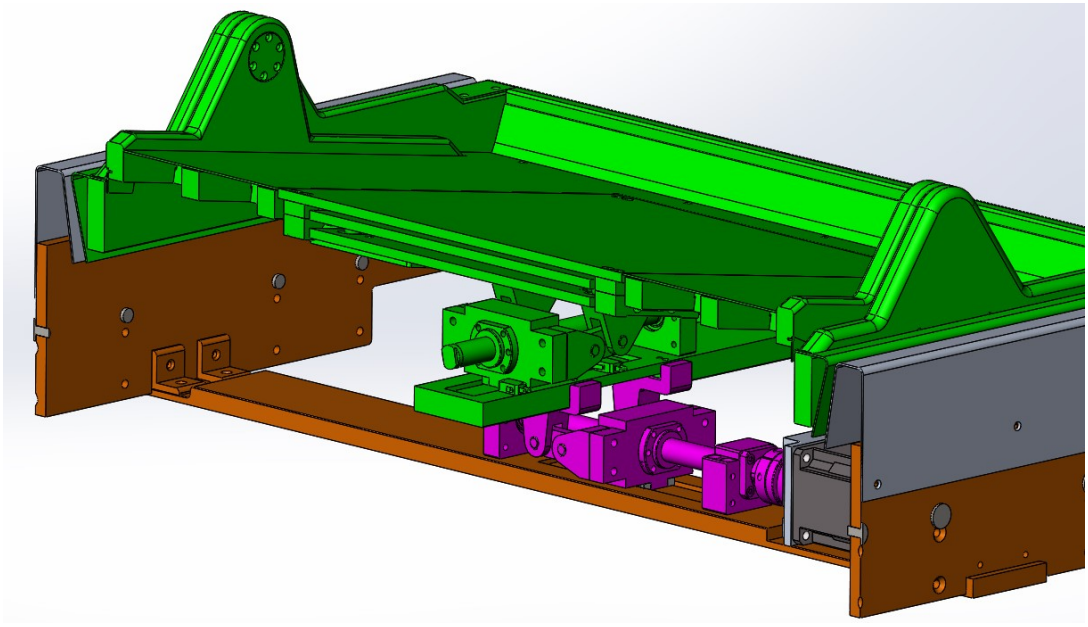

Figure 3.61: AP-ML Mechanism Connections

The most critical parts in AP subassembly were the pins about which the structure rotates. The design details of the pins are as following:

The technical drawing of the Pin is shown in Figure 3.62.

The load acting on the pin include the weight of the patient (140 kg for the worst scenario) and the rotating platform (45 kg). Hence, the loads are presented in Figure 3.63.

The stainless steel pin with 210 MPa yield strength was subjected to 910 N vertical load (corresponding to half of the total weight of the platform and the patinent) , as pin has discontinuities, stress concentrations have to be analysed. The plot 3.64 gives information about choosing the right stress concentration factor K_t. Values in Table 3.5 that are not available in the Figure 3.64 are

interpolated.

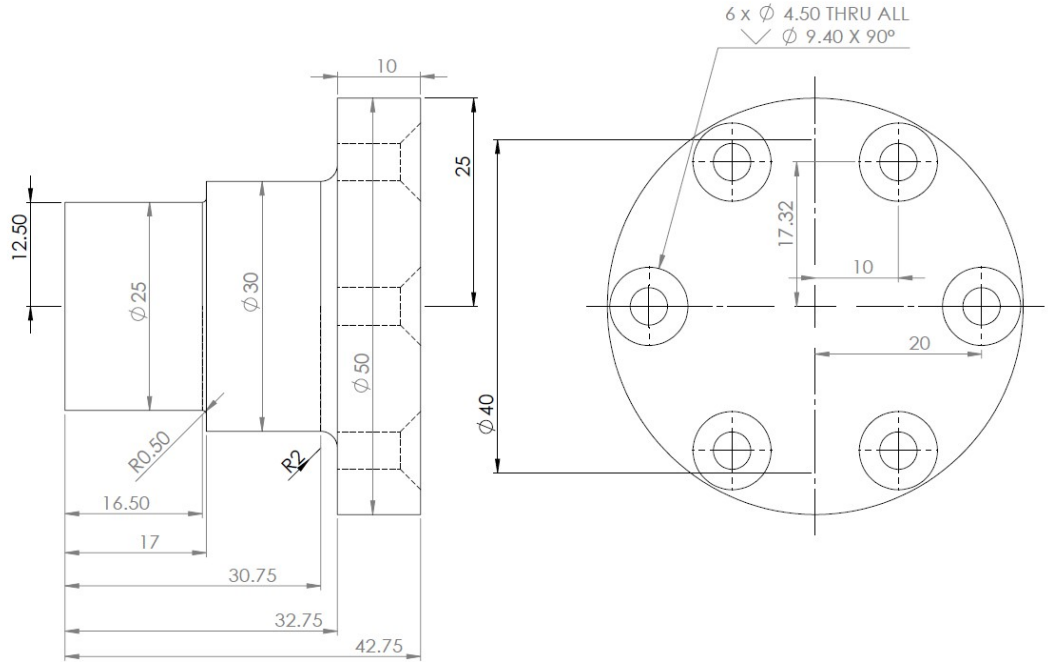

Figure 3.62: AP-Rotation Pin

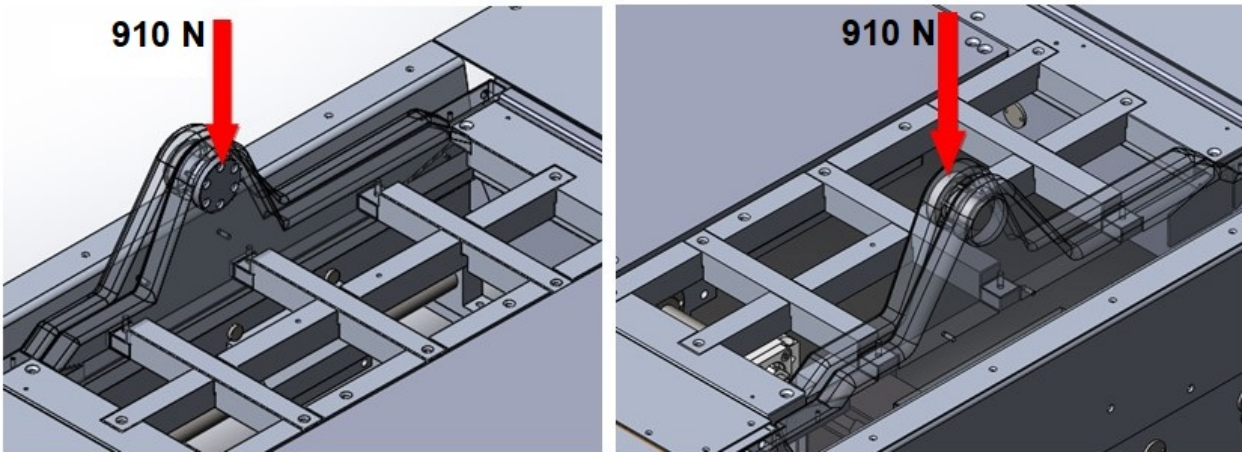

Figure 3.63: Loading of the AP-Rotation Pin

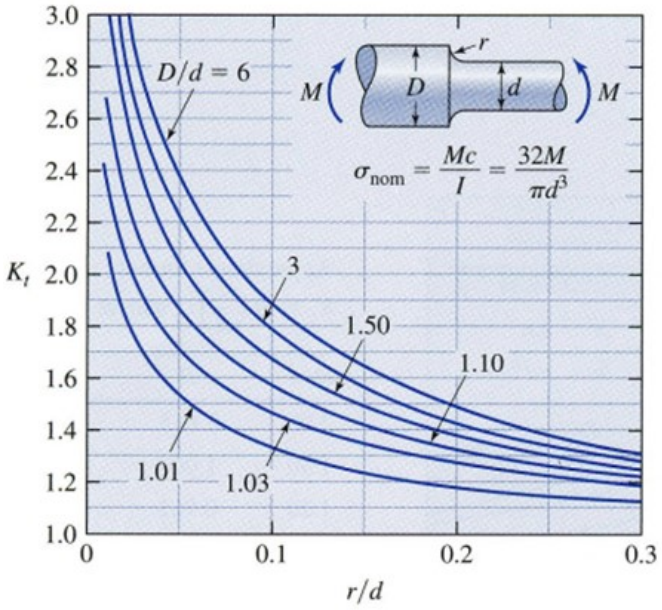

Approximate formula
$K_t \approx B\left(\frac{r}{d}\right)^a$, where:

D/d	B	a
6.00	0.879	−0.332
3.00	0.893	−0.309
1.50	0.938	−0.258
1.10	0.951	−0.238
1.03	0.981	−0.184
1.01	0.919	−0.170

Figure 3.64: Stress Concentration Factor [17]

Table3.5: Stress Concentrating Factor of Part Pin

-	R2	R0.5
r/d	0.07	0.02
D/d	1.67	1.2
B	0.93	0.95
a	-0.26	-0.24
K_t	1.91	2.45

For the critical point the normal stress will be;

$$\sigma_{corr} = K_t \cdot \sigma \tag{3.67}$$

where

$$\sigma = \frac{32 \cdot M}{\pi \cdot d^3} \tag{3.68}$$

and

$$M = F_{load} \cdot L \tag{3.69}$$

and length of the moment arm is taken $L = 29.5\ mm$. Inserting all numerical

values into the equation, σ_{corr} was found to be;

$$\sigma_{corr} = 42.8MPa$$

The safety factor was calculated as;

$$N = \frac{S_{yield}}{\sigma_{corr}} = 4.91$$

Also finite element analysis was performed for the pin, the result was obtained as presented in Figure 3.65.

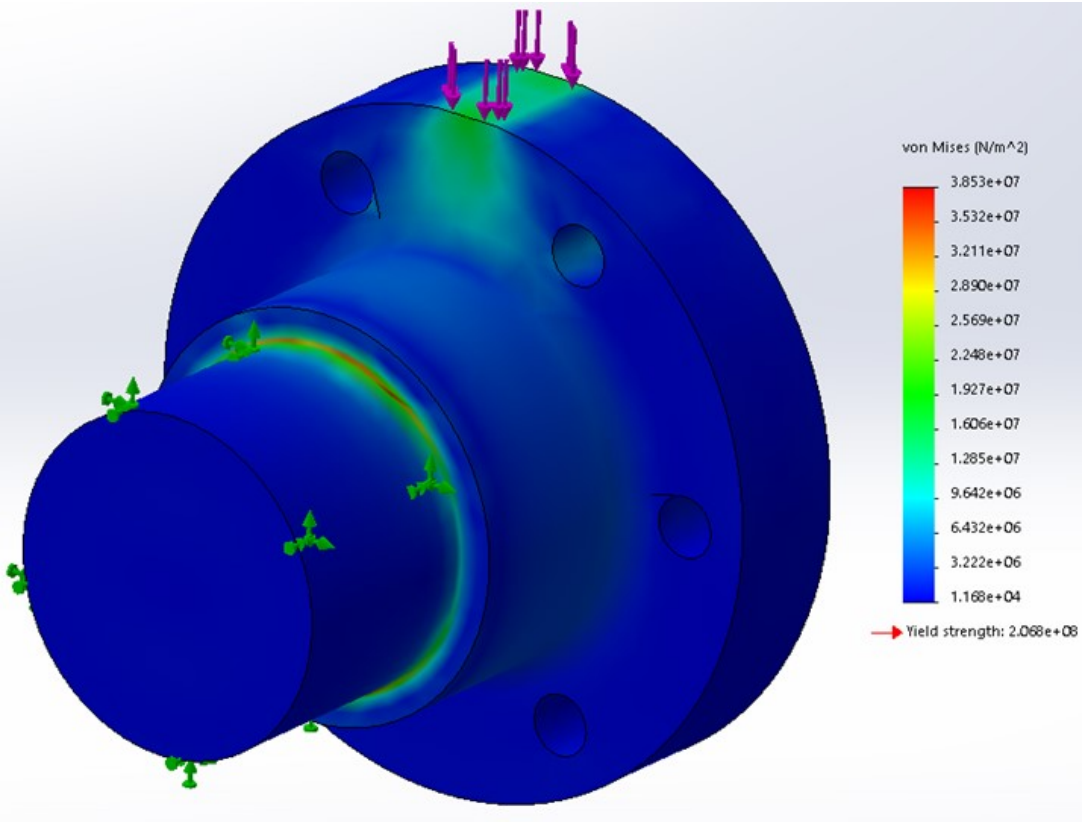

Figure 3.65: Von Mises Stress Distribution of Part "Pin"

Both results show a safety factor N about 5.

3.5.2 Platform Roll (ML) Rotation Subassembly

The ML mechanism was explained in the previous sections. The interface with AP rotation subassembly was also presented. The interface of ML subassembly

with the translating subassembly is simply formed by linear bearings. The four bearings (red) move forwards and backwards with the whole structure (blue) as shown in Figure 3.66.

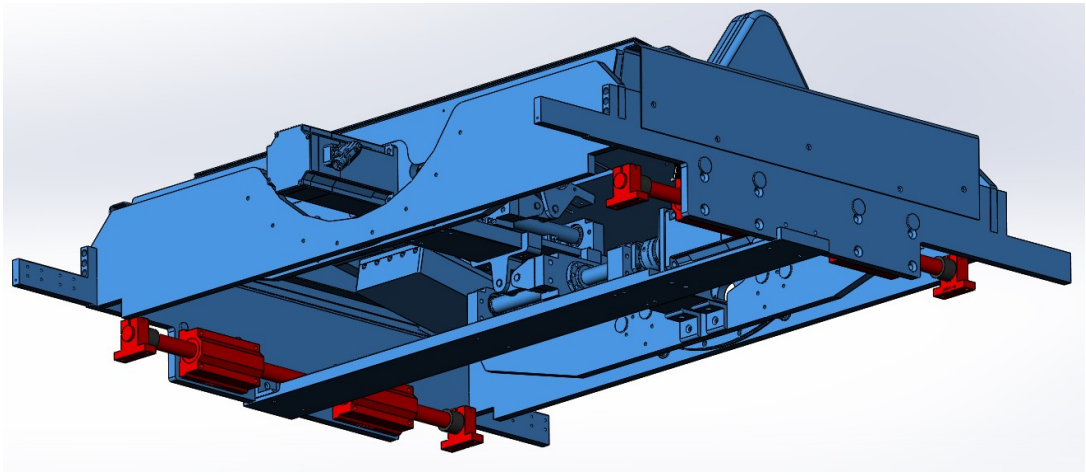

Figure 3.66: ML Subassembly Interface with Translating Subassembly

3.5.3 Platform (AP) Translation Subassembly

The translating subassembly carries the other two rotating mechanisms. The whole structure rests on four points on the chassis as shown in Figure 3.67. The motor of the translating mechanism is fixed to the chassis and the rods of the linear bearings guide the platform to move along their direction. Figure 3.68 presents a section view showing the details of chassis translating subassembly interfaces. It can be inferred from the view that the platform motion mechanisms are embedded in the platform structure and there is no mechanical interference during mechanism movements, each within their defined ranges.

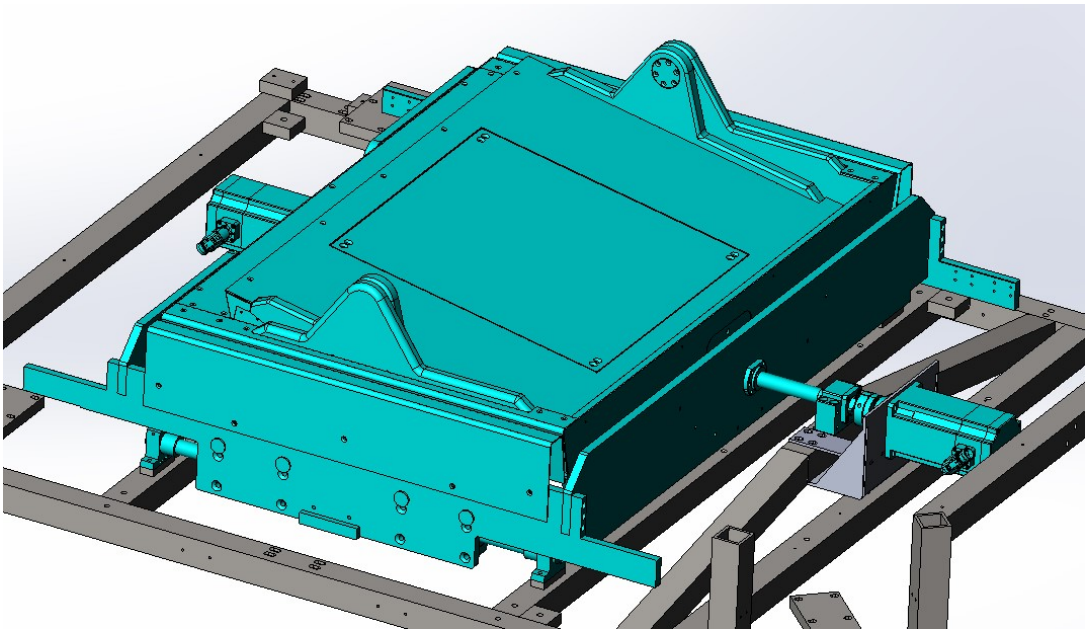

Figure 3.67: Translating Subassembly Interface with Chassis

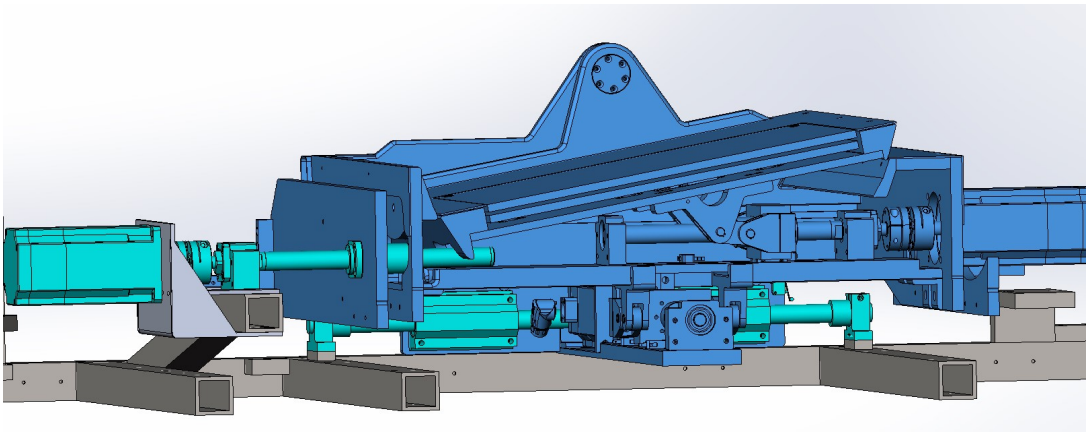

Figure 3.68: Translating Subassembly Interface with Chassis

As the translating structure carries the whole moving platform, it is also the heaviest subassembly that moves approximately 320 kg including the patient. Therefore a structural analysis was performed on the linear guiding induction hardened rod. To see the safety of the design a total load of 3150 N was applied on the two rods. Figure 3.69 reveals that the most critical points have a factor

of safety about 3.

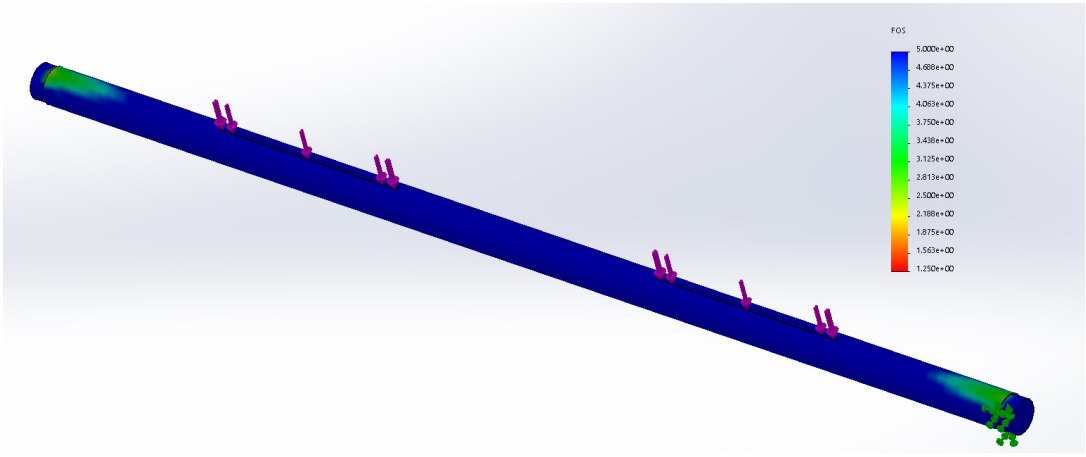

Figure 3.69: Factor of Safety Distribution of Static Load Analysis of the Rod

3.5.4 Visual Surround (AP) Rotation Subassembly

The motion mechanism of the visual surround was studied in detail, in previous sections. To remember, the rotation mechanism of the visual surround has interfaces with the chassis and the patient harness bars as shown in Figure 3.70. The actuator of the visual surround mechanism was mounted to the chassis, having rotary connection. The visual surround, formed by box sections was connected to the harness bars. Pins on two sides of the harness bars were inserted in the pillow bearings placed on the visual surround.

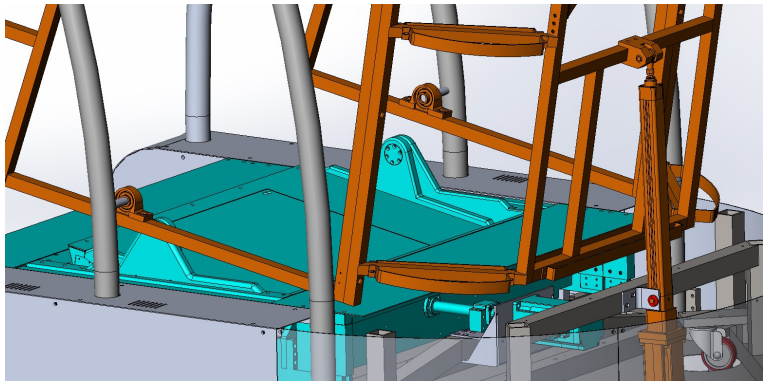

Figure 3.70: Visual Surround Subassembly Interface with Chassis and Harness Bars

3.5.5 LCD/LED Display Mechanism Subassembly

According to the design requirements a patient display was placed on the visual surround. Considering children and adult patients, a height adjusting mechanism as shown in Figure 3.71 was designed.

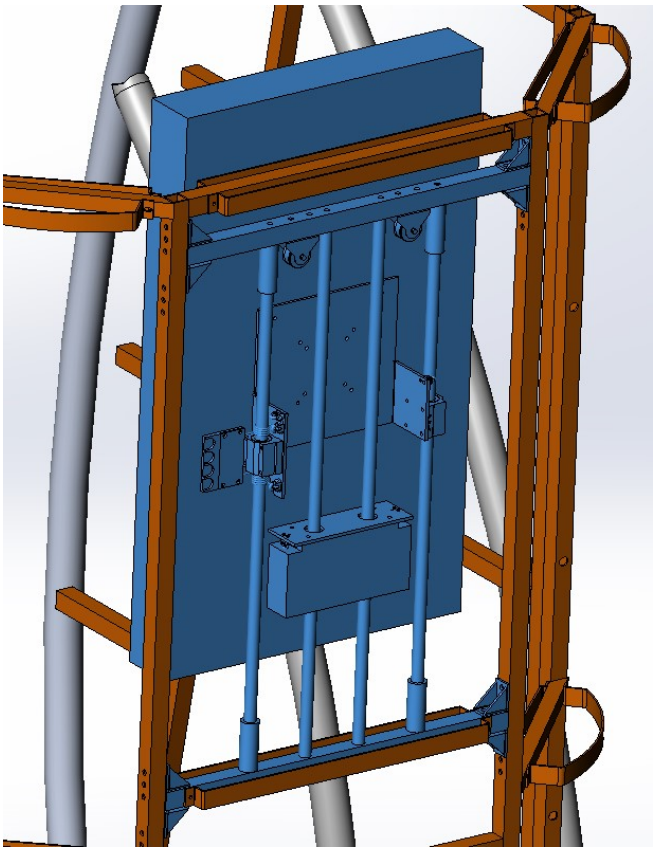

Figure 3.71: LCD/LED Display Height Adjusting Mechanism

The design consists of four rods where the inner two of them carries a counter weight equal to the weight of the 40 *in* LED/LCD display. The outer ones guide the display where the counter weight and the LED/LCD display are connected with steel wires by two pulleys at the top. The mechanism is fixed with the help of a spring where at rest it holds the display at its position. When the spring is pressed, it expands and gets loose, so the "brake" is released and the LED/LCD display can be moved up or down.

3.5.6 Patient Harness Subassembly

The Patient Harness bars (green) in Figure 3.72 secure the patient in case of a fall. The patient is attached to the bars with a harness waistcoat to the connection points (red) on the bars are shown in Figure 3.73. The whole subassembly is fixed to the chassis with locks as shown in Figure 3.74. The harness bars rest on the chassis, the locks which are also mounted on the chassis clamp the harness bars fixed so that the bars do not move when load is applied form any point and any direction.

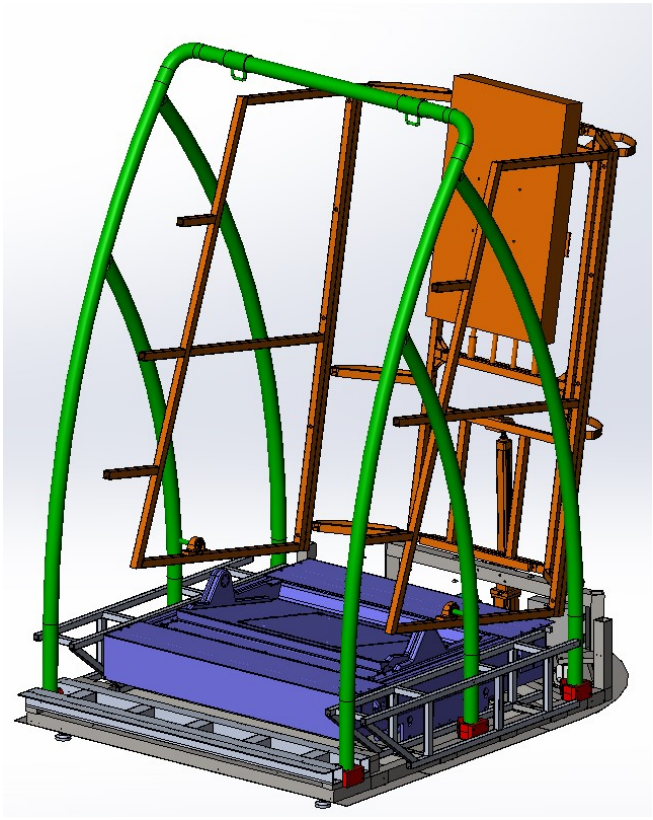

Figure 3.72: Harness Bars

In contrast of its huge geometry, the weight of the harness bar has to be a concern for the carrying person. The total assembly consists of three parts, the side bars and the top bar with the waistcoat interface detached. Moreover, the material of the harness bars was chosen to be Aluminum 6061-T6 to have a lighter structure. However in this case considering aluminum material, load

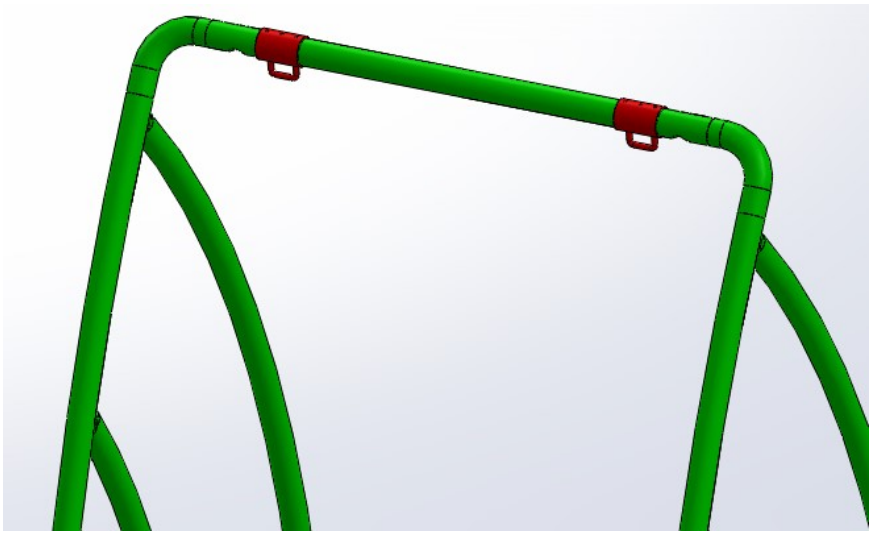

Figure 3.73: Harness Waistcoat Connection Points

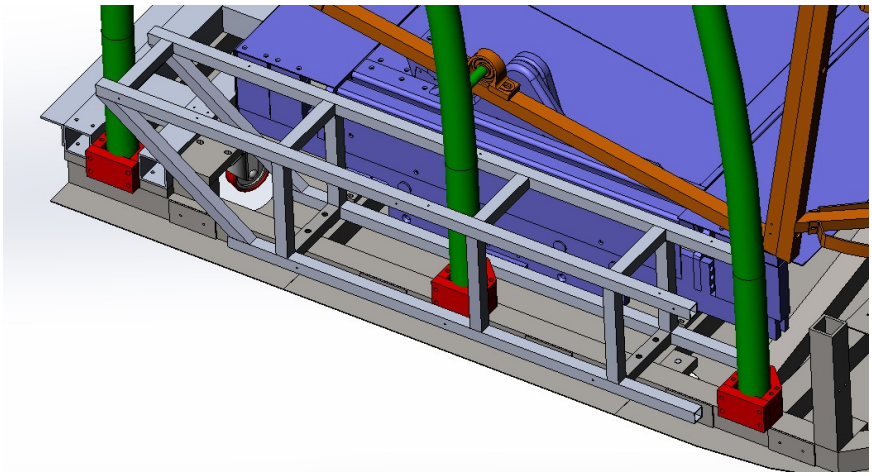

Figure 3.74: Harness Bars Lock

analysis on the pins were made. The load acting on the pins, about which the visual surround is rotating is shown in Figure 3.75. The force is acting on the tip of the pin and the critical point is at the edge of the pin, welded on the harness bar. So the stress level will be as a function of the length of the pin. At the edge;

$$\sigma_{harness,pin} = \frac{M \cdot r_{pin}}{I_{pin}} \tag{3.70}$$

For pin length L=90 mm, pin diameter r=10 mm the following normall stress plot is drawn shown in Figure 3.76:

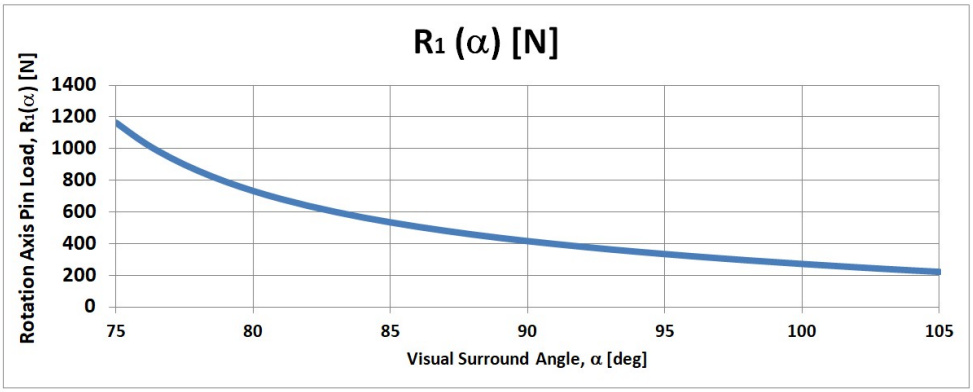

Figure 3.75: Force Acting on Harness Rotation Axis Pin as a Function of Visual Surround Angle "α"

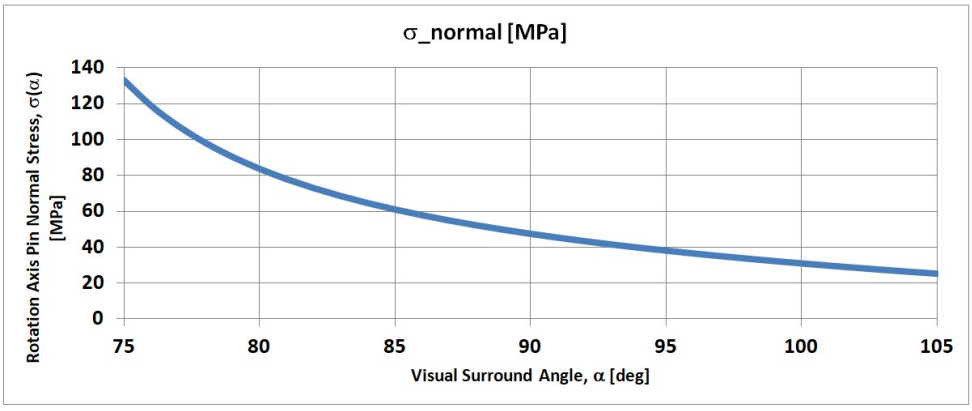

Figure 3.76: Harness Pin Analysis, Normal Stresses as a Function of Visual Surround Angle "α"

3.6 Final Product

The total height of the platform after finalizing the design was approximately 320 mm above the ground. In order make it easier to get on the platform, the design included two steps where the second step (grey) is also the translating subassembly. Two detachable bars hanging from the top harness bar were added for further safety purpose.

The photo in Figure 3.77 presents the device which is assembled after manufacturing process. On the left side of the picture the system computer and operator interface can be seen. Whereas on the right is the so called "Robotic Balence" CDP-Device with all its accessories. All the mechanism positions are at home position, the pitch (AP) and roll (ML) axis are at level position, the visual surroud is at 90 degrees and the translational position of the platform is at rest position.

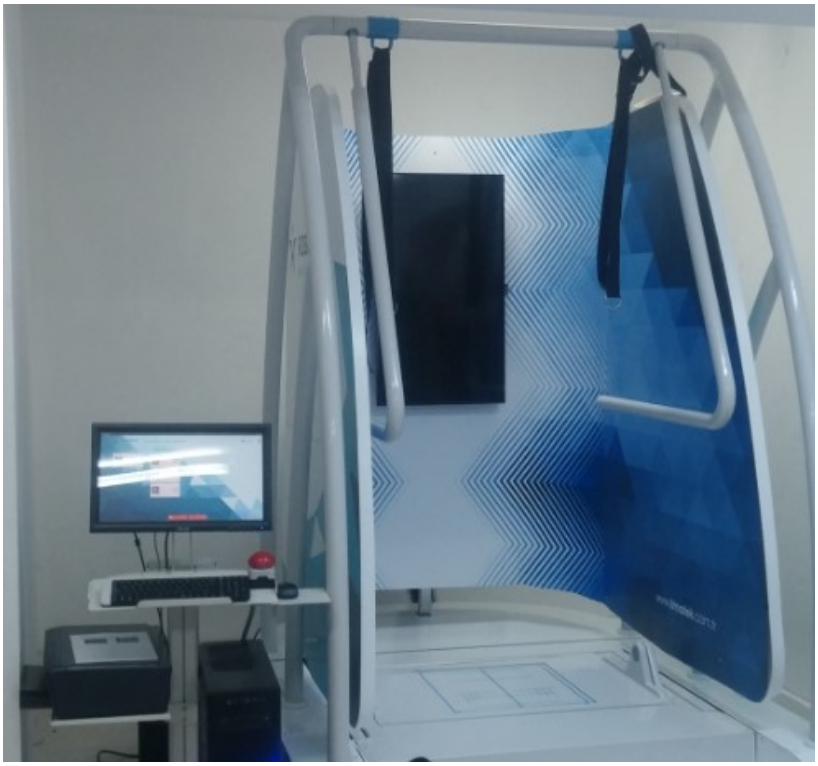

Figure 3.77: CDP-Device "Robotic Balance"

In Figure 3.78 each of the the device axes are moved; toes down in pitch (AP) direction, right-side up in roll (ML) direction, Visual Surround at lowest limit at 80 degrees and translating position is at the forward limit. In Figure 3.79, this time each of the device axes are moved in reverse direction; toes up in pitch (AP) direction, left-side up in roll (ML) direction, Visual Surround at highest limit at 100 degrees and translating position is at the back limit.

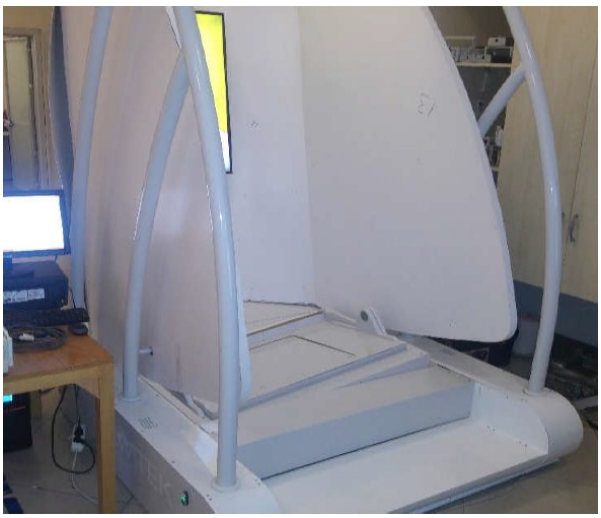

Figure 3.78: CDP-Device "Robotic Balance"

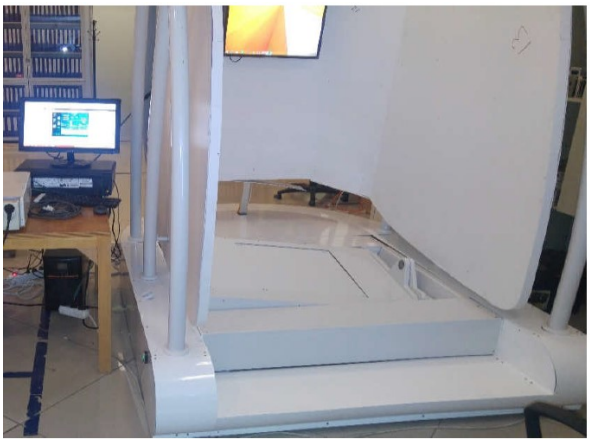

Figure 3.79: CDP-Device "Robotic Balance"

CHAPTER 4

VERIFICATION

In this section measurement results are presented. It was measured how precise the device performs the motions that are commanded through the system computer.

4.1 Platform and Visual Surround Motion Measurements

As defined earlier the motion profiles were set according to CDP protocol tests. The three axis platform motions and the visual surround motion velocity profiles were specified to be in trapezoidal shape.

The measurements were done with a patient on the platform to simulate real conditions. So, load was acting on the platform and the motion profiles were analysed whether the desired profiles were obtained with the designed mechanism and selected components.

The height of the patient was 186 cm and was 95 kg. The patient was placed on the platform where the position of his ankle was aligned with the rotation axis direction, the width between his feet was 35 cm. The measurement device was an Android operated smartphone (LG G2 D802TR) furnished with a 3-axis LGE accelerometer sensor (STMicroelectronics, 0.001 m/s^2 precision) and a 3-axis LGE gyroscope (STMicroelectronics, 0.001 rad/s precision). The resolution values of the sensors was obtained from a research, investigating the use of smart phones for physical measurements. Luckily, the same smart phone (LG G2 D805) with same hardware was used in the study [36]. The "AndroSensor"

application was used to monitor and record the preferred data, at a sampling frequency 200 Hz, in average. Angular speeds and orientation of the platform were recorded with the use of the smart phone. The translation motion of the platform was recorded by an ultrasonic sensor which was connected to Arduino Uno for data acquisition. The sampling frequency was again set to 200 Hz. Figure 4.1 represents the measurement technique for platform motions. The smart phone was bonded to the force plate so that the motions were recorded directly.

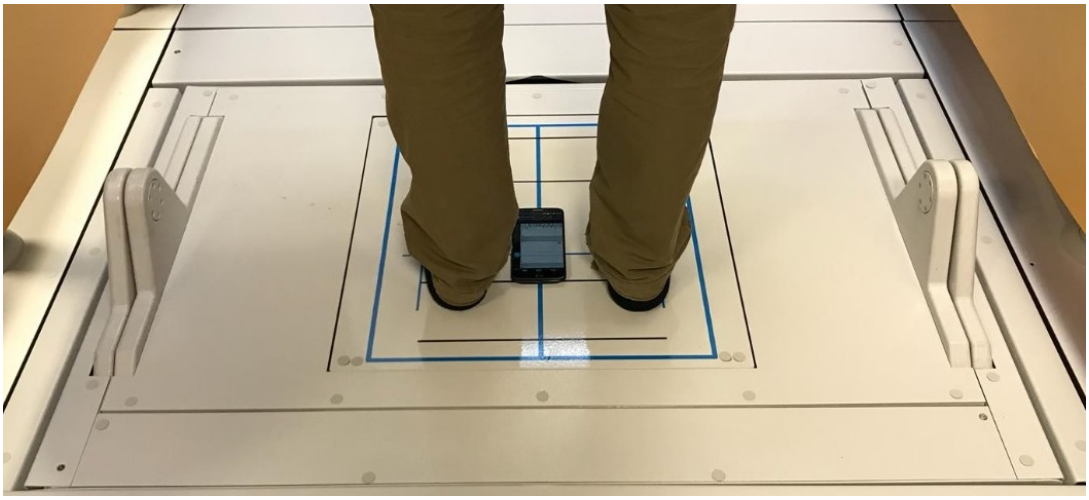

Figure 4.1: Platform Motion Measurements

Figure 4.2 represents the measurement technique for visual surround rotation. The smart phone was bonded to the mechanical structure of the visual surround near to the rotation axis so that no elastic or loose part would affect the measurements.

Figure 4.2: Visual Surround Motion Measurement

Figure 4.3 presents the translational motion measurement. The ultrasonic sensor was bonded to the stationary part of the device and the moving part was traced by the sensor.

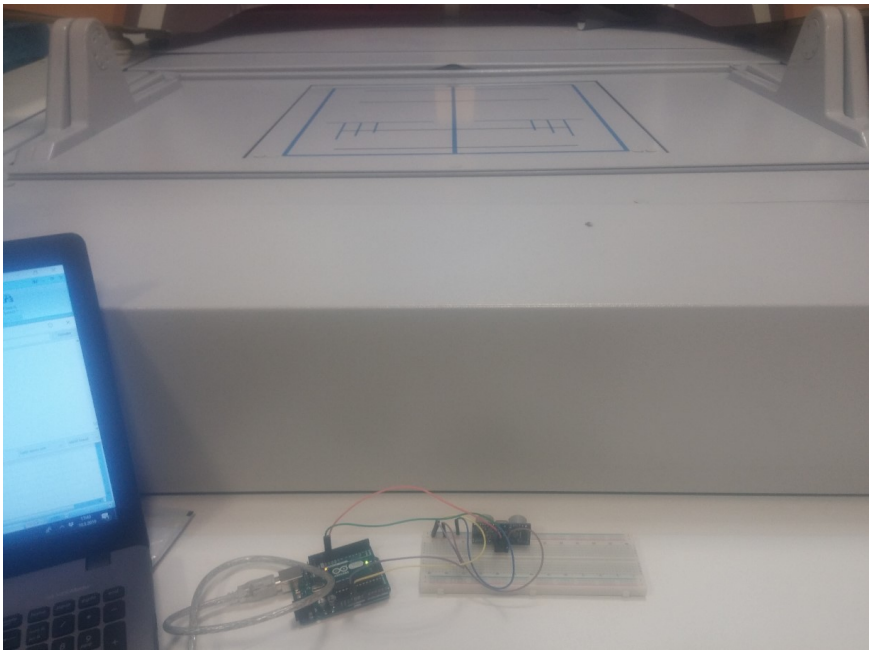

Figure 4.3: Translational Motion Measurement - Ultrasonic Sensor

The plots below show the deviations between the desired and actual motions for each motion axis.

For the AP rotation axis the commanded position was to rotate the platform to 8 *deg* with a maximum rotation speed of 23 deg/s. Figure 4.4 presents the AP sway angle of the platform. The green line represents the ideal linear form of the desired motion, whereas the red line is the actual position obtained from the measurement. As the measurement is almost identical with the linear-ideal form, the performance of the AP axis was evaluated as satisfactory. Moreover, 4.5 presents the speed deviation from ideal trapezoidal form for AP rotation. Here, the measurement result have more deviation than the angular position results. However, again the result fits on the ideal trapezoidal shape. The overall character of the motion is evaluated as satisfactory considering desired position, maximum speed and total duration of the motion.

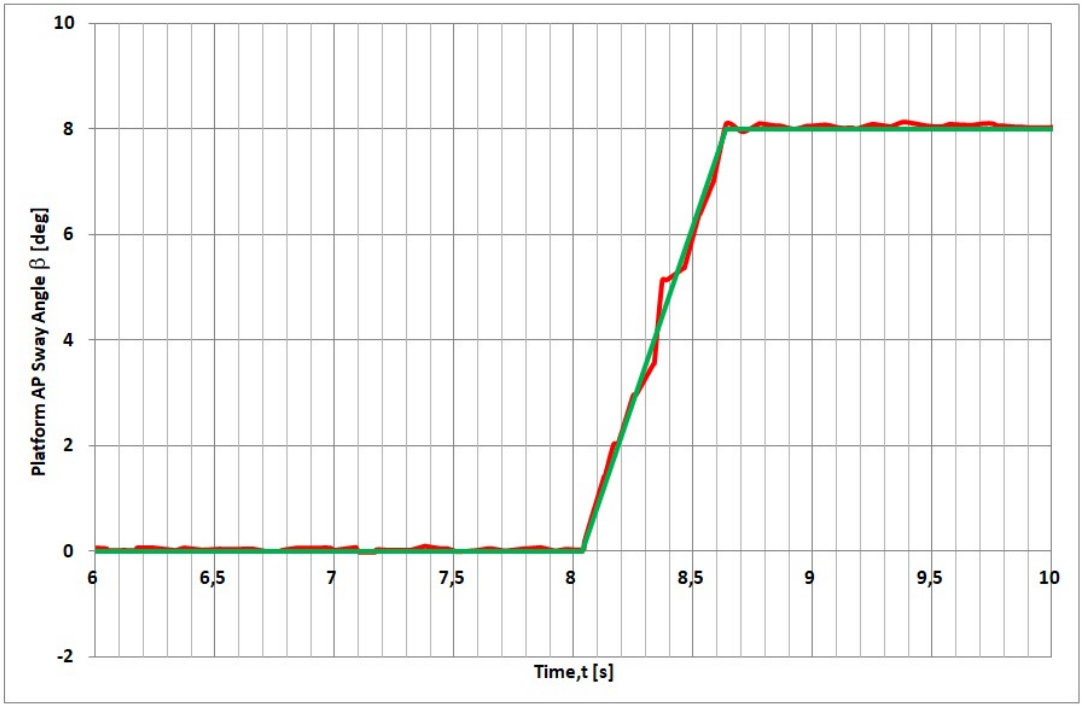

Figure 4.4: AP Rotation Position Measurement

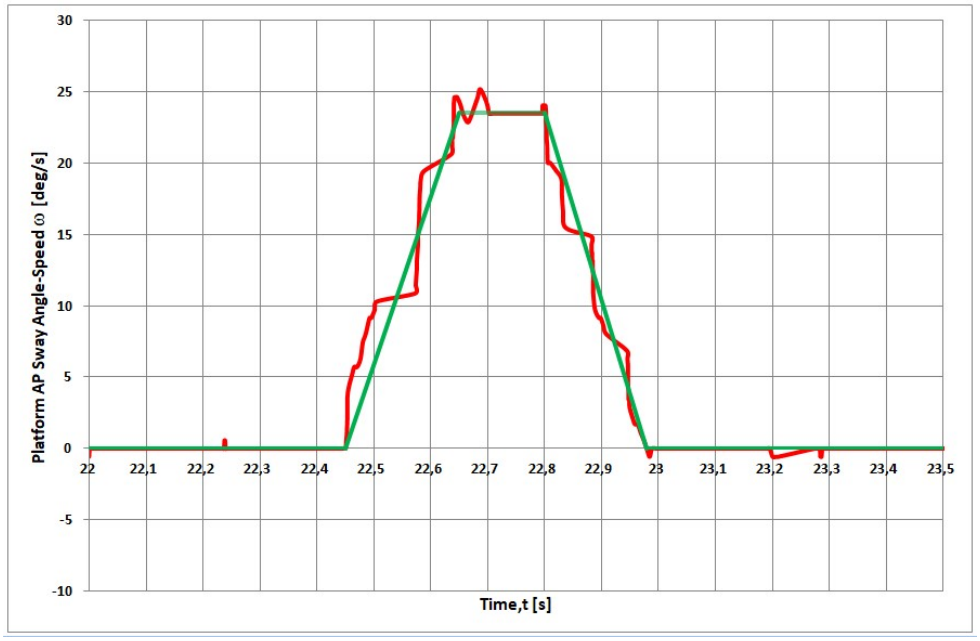

Figure 4.5: AP Rotation Speed Measurement

Similarly, for the ML motion axis Figure 4.6 and 4.7 represent small deviations from ideal ML rotation position and ML speed.

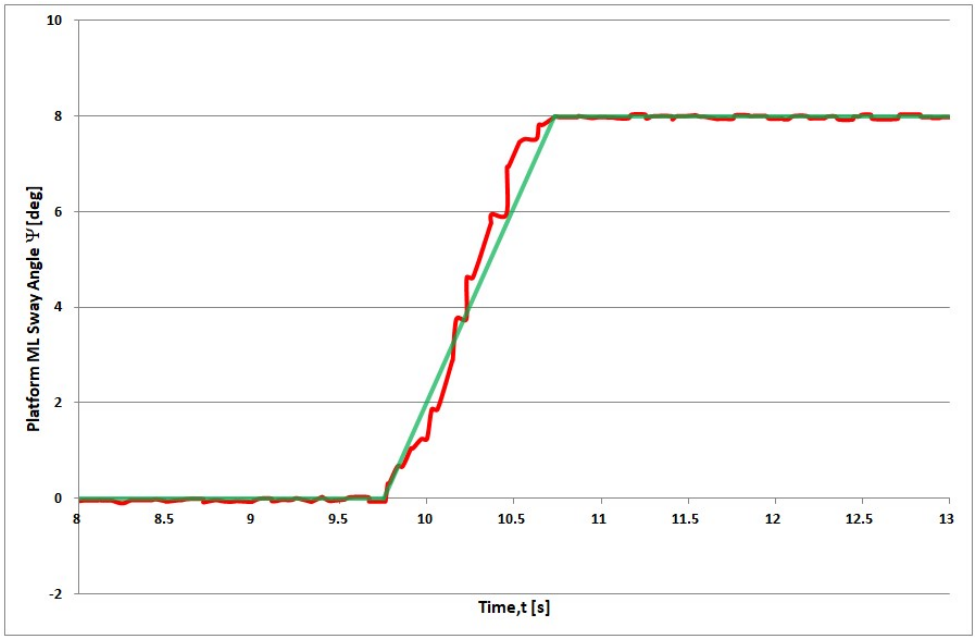

Figure 4.6: ML Rotation Position Measurement

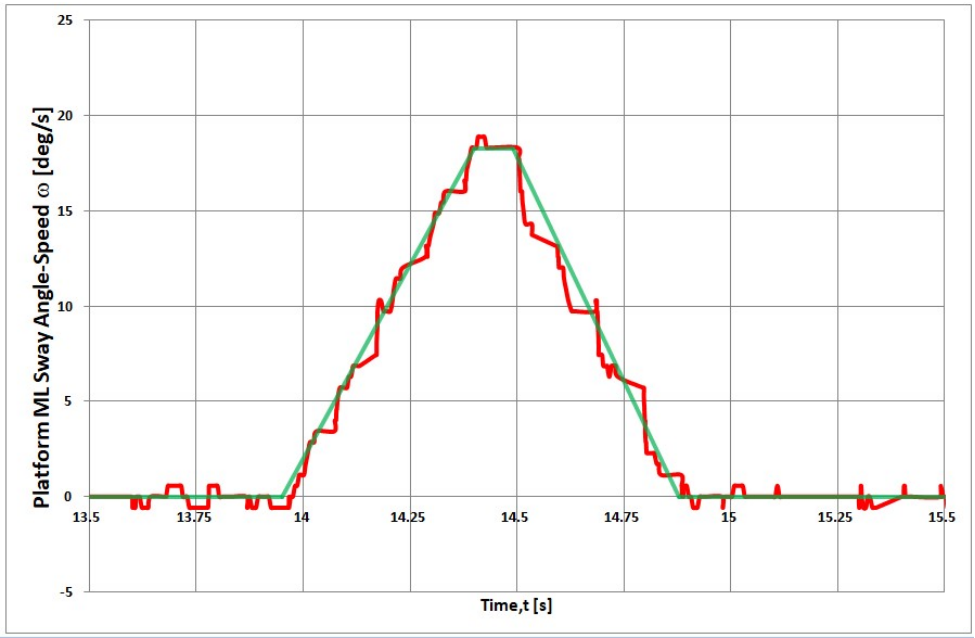

Figure 4.7: ML Rotation Speed Measurement

Figure 4.8 shows the measurement for translating motion. The motion includes forwards and backwards translations. Only the position of the translating platform was measured. The acceleration and the speed of the motion was also recorded with the smart phone; however, the noise of the data was too much to make a clear evaluation. Therefore, only the results obtained from the measurement with the ultrasonic sensor were presented. Again it is obvious that the desired motion overlaps with the measured motion. From the plot it can be seen that there is a slight change of the position at stationary position at 100 mm which is commented as measurement error of the ultrasonic sensor.

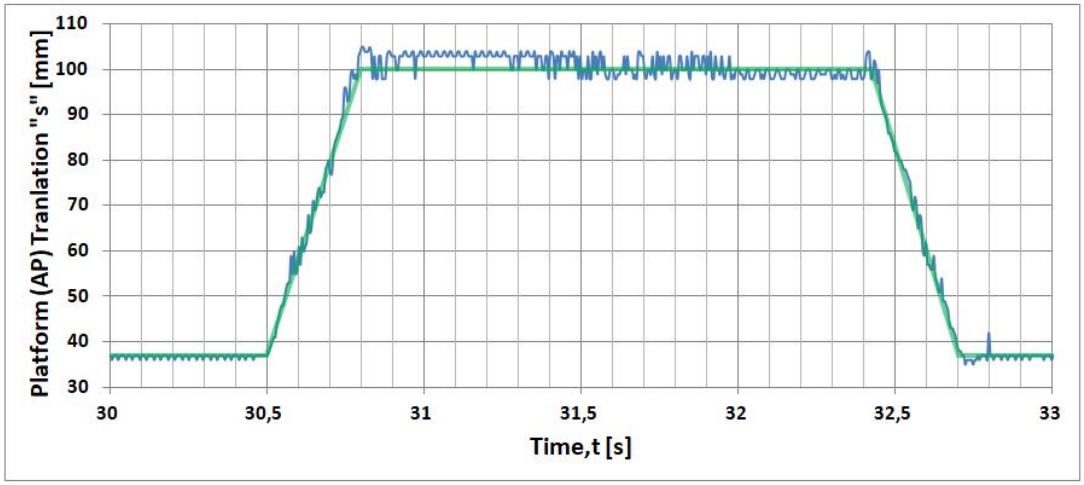

Figure 4.8: Platform (AP) Translation Position Measurement

Figure 4.9 and 4.10 shows the deviation for Visual Surround rotation. The measurement results represent sufficient accuracy, as the actual position and speed of the motion axis fits on the ideal shape of the motion profile as depicted in the plots.

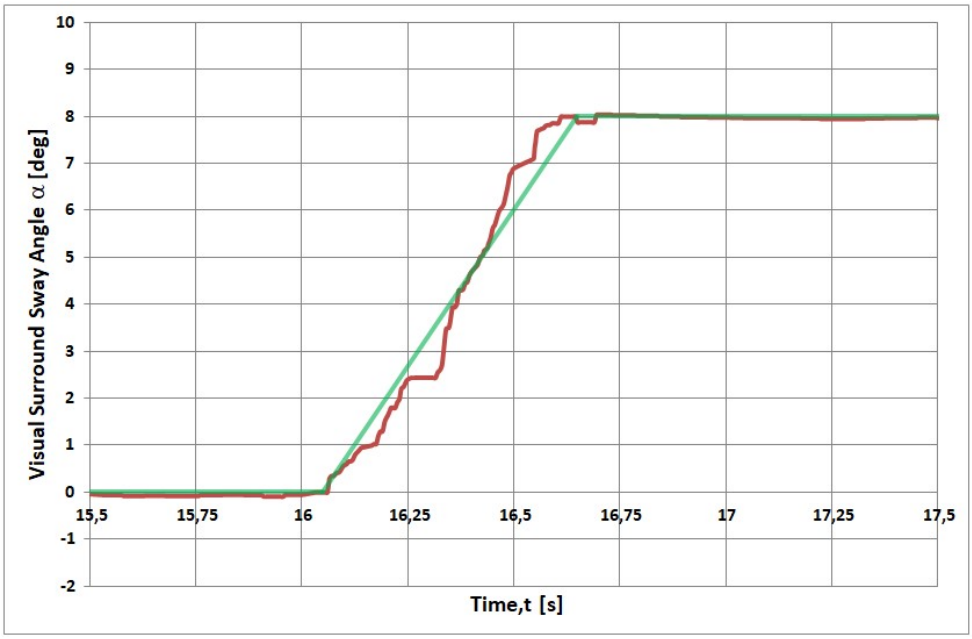

Figure 4.9: Visual Surround Rotation Position Measurement

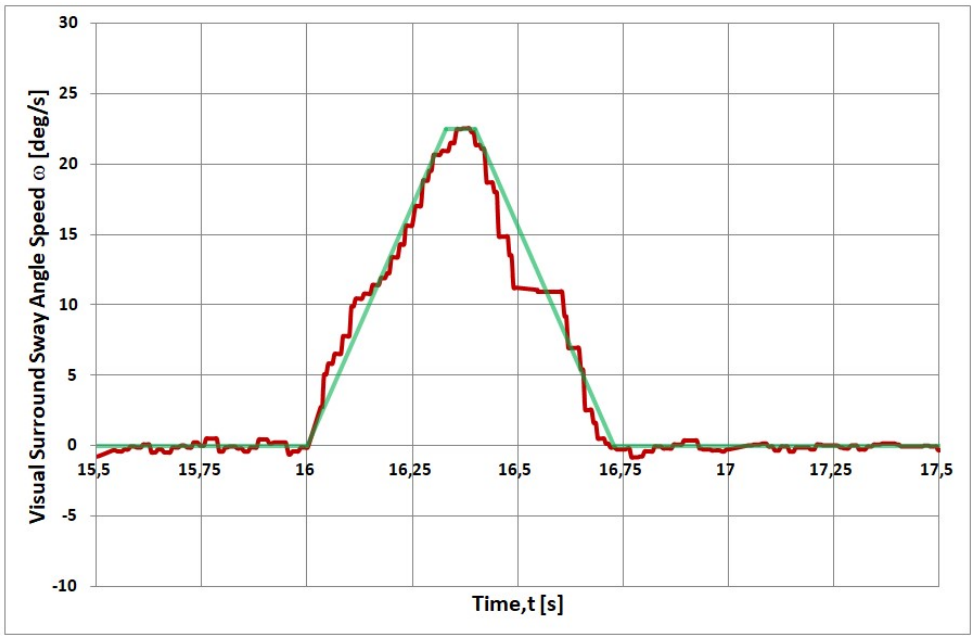

Figure 4.10: Visual Surround Rotation Speed Measurement

The motion commands were given by the system computer. A GUI was developed for platform tests. Different from the time dependent motion profiles as defined in the earlier chapters, target position, speed and acceleration values were defined on the system as time is not a variable that can be set as an input.

4.2 Force Plate CoP Measurements

The CoP data the system generates plays a key role for the conductance of the CDP tests and evaluation of the test reports. Therefore, the accuracy of the measurements becomes an important parameter. Firstly, each loadcell (FL, FR, RR, RL) was calibrated and a linear trendline was drawn. Then, the linear trendline equation for each load cell was used in the CoP formula to calculte the actual CoP.

Calibration was done by applying (70 kg) 686.7 $Newton$ load on five different points on the force plate. Then, the digitized raw data for each load cell at each load application point was recorded. In addition, the raw data when no load

was on the plate was also recorded. At each point, the fraction of the applied total load acting on each of the four load cell was calculated. Then, for each load cell at each corresponding load application point and corresponding load fraction, digital data was recorded and following plots were drawn.

Although the applied load at some points are same, i.e. zero, the output of the sensor was not identical. This deviation was considered as a result of the position error of the applied load. Therefore, the differences in the output was noticed to be negligible.

Forward-Left Loadcell : Table 4.1 represents the data of the calibration process and Figure 4.11 presents the output of the load cell under different loads.

Table4.1: FL Load Cell Measurements

Test Point	X (mm)	Y (mm)	W-fraction	W (Newton)	FL Raw Data (Bit)
Empty	-	-	0	0	35
Point-1	0	0	0,1875	128,8	810
Point-2	220	0	0	0	67
Point-3	-220	0	0,375	257,5	1700
Point-4	0	290	0,5	343,35	2200
Point-5	0	-170	0	0	7

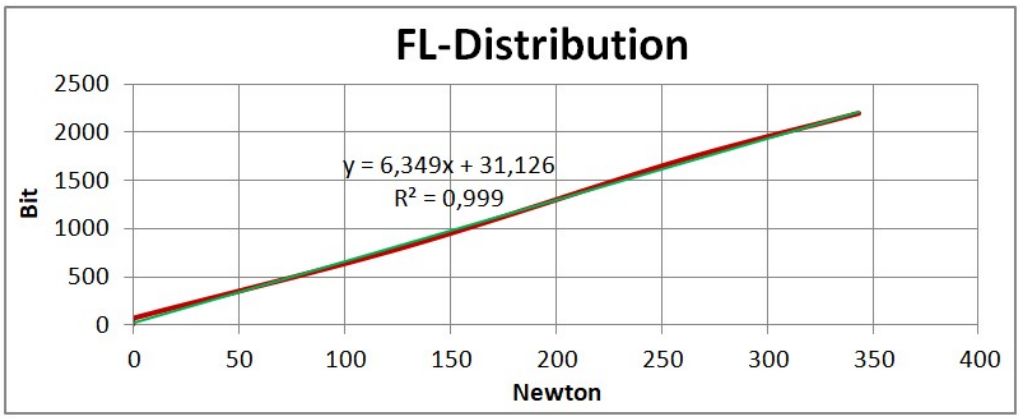

Figure 4.11: Forward-Left Load Cell

Forward-Right Loadcell : Table 4.2 represents the data of the calibration process and Figure 4.12 presents the output of the load cell under different loads.

Table4.2: FR Load Cell Measurements

Test Point	X (mm)	Y (mm)	W-fraction	W (Newton)	FL Raw Data (Bit)
Empty	-	-	0	0	261
Point-1	0	0	0,1875	128,8	1075
Point-2	220	0	0	0	1970
Point-3	-220	0	0,375	257,5	280
Point-4	0	290	0,5	343,35	2700
Point-5	0	-170	0	0	260

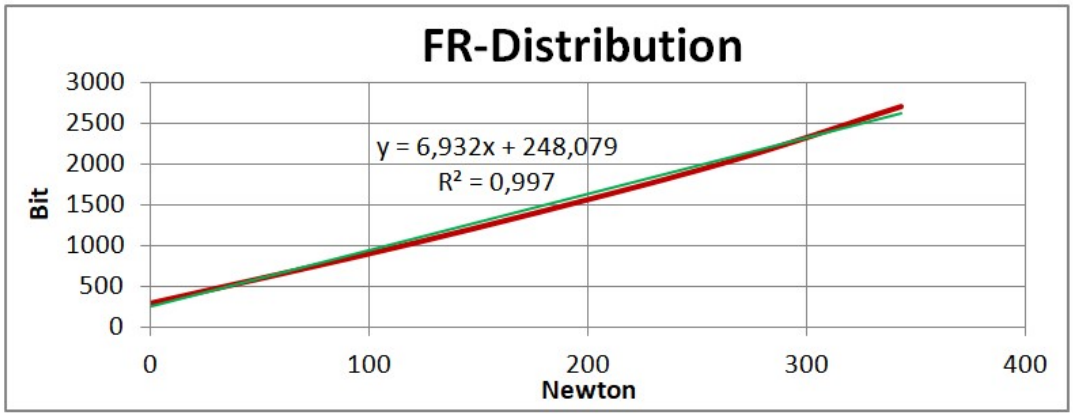

Figure 4.12: Forward-Right Load Cell

Rear-Left Loadcell : Table 4.3 represents the data of the calibration process and Figure 4.13 presents the output of the load cell under different loads.

Table4.3: RL Load Cell Measurements

Test Point	X (mm)	Y (mm)	W-fraction	W (Newton)	FL Raw Data (Bit)
Empty	-	-	0	0	469
Point-1	0	0	0,3125	214,6	2200
Point-2	220	0	0	0	500
Point-3	-220	0	0,625	429,2	4050
Point-4	0	290	0	0	550
Point-5	0	-170	0,5	343,35	3200

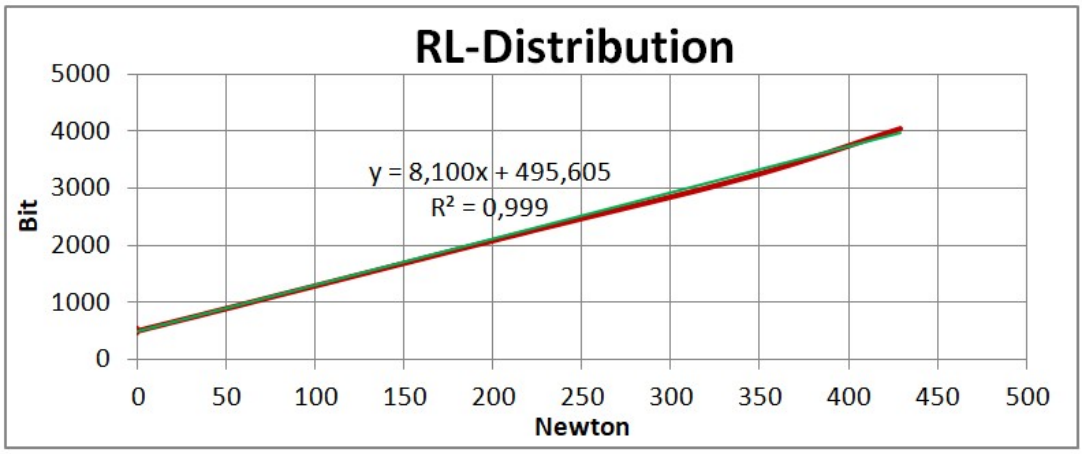

Figure 4.13: Rear-Left Load Cell

Rear-Right Loadcell : Table 4.4 represents the data of the calibration process and Figure 4.14 presents the output of the load cell under different loads.

Table4.4: RR Load Cell Measurements

Test Point	X (mm)	Y (mm)	W-fraction	W (Newton)	FL Raw Data (Bit)
Empty	-	-	0	0	92
Point-1	0	0	0,3125	214,6	1500
Point-2	220	0	0,625	429,2	3200
Point-3	-220	0	0	0	75
Point-4	0	290	0	0	7
Point-5	0	-170	0,5	343,35	2500

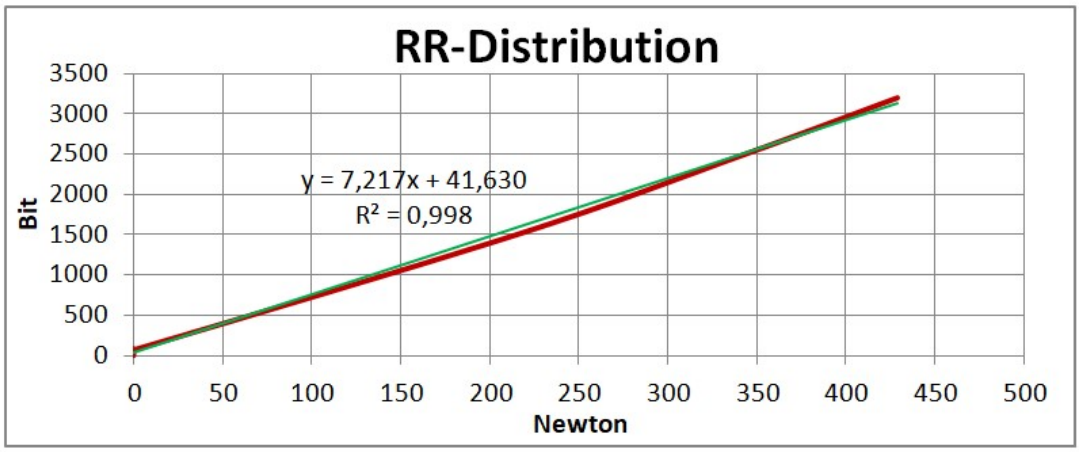

Figure 4.14: Rear-Right Load Cell

Measurements on the force plate was done by applying specific load as in Figure 4.15 on predetermined points as presented in Figure 4.16 and the outcome of the system and the known application points were compared. The Table 4.5 presents the results for each point.

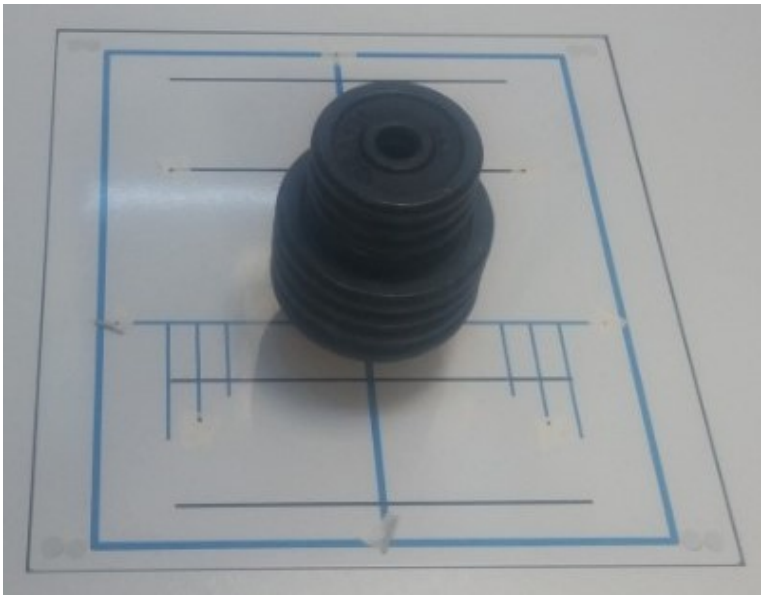

Figure 4.15: Force Plate Point-1 Measurement

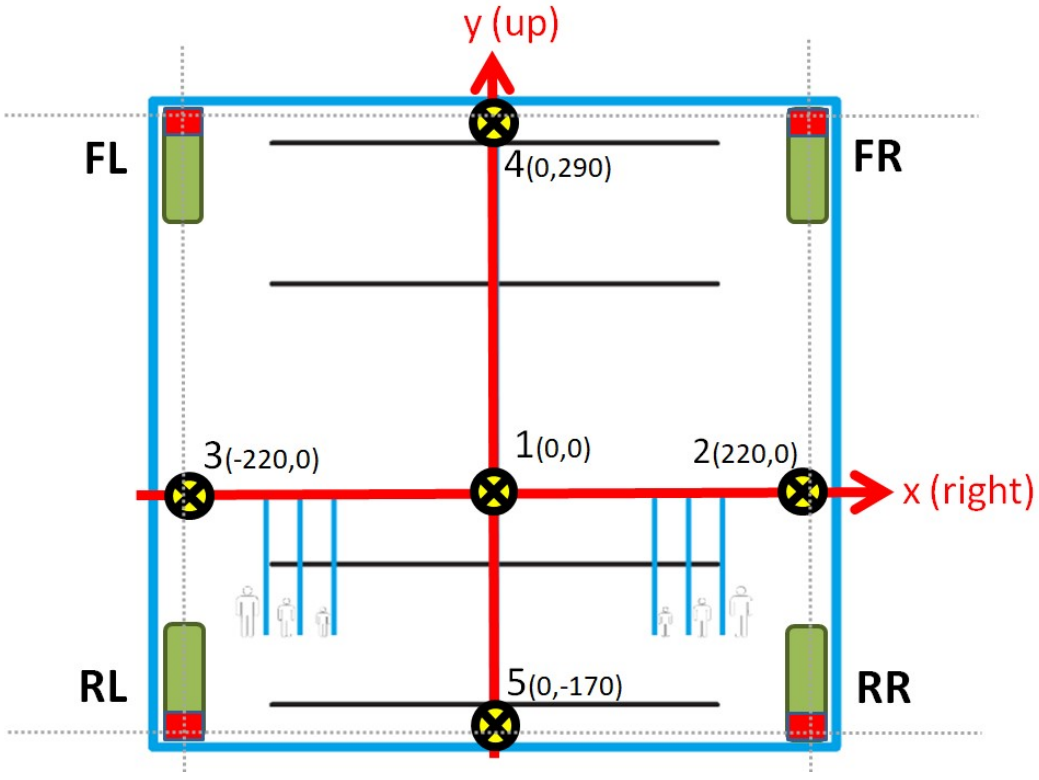

Figure 4.16: Force Plate Measurement Points

Table4.5: Force Plate Raw Data and Calculated Force

Test Point	Load Cell Data							
	FL	FL (N)	FR	FR (N)	RL	RL (N)	RR	RR (N)
Empty	35	0,6	261	1,9	469	-3,3	92	7
Point-1	810	122,7	1075	119,3	2200	210,4	1500	202,1
Point-2	67	5,7	1970	248,4	500	0,5	3200	437,6
Point-3	1700	262,9	280	4,6	4050	438,8	75	4,6
Point-4	2200	341,6	2700	353,7	550	6,7	7	-4,8
Point-5	7	-3,8	260	1,7	3200	333,9	2500	340,6

Table 4.5 was created using the linear trendline equations for each load cell. In fact, the actual values in the table in next colomns of raw load cell data values represent the calculated data using these equations.

The following equations were used for determining the CoP. In the equations "actual" load cell data found in the previous step tabulated in Table 4.5 was used and 4.6 was created. Note that the geometric center of the plate is not identical with the coordinate axis origin. Hence, a 62.5 mm shift occurs in the CoP_y formula.

$$CoP_x = \frac{(RF + RR) - (LF + LR)}{RF + RR + LF + LR} \cdot 226.5 \ \ mm \tag{4.1}$$

$$CoP_y = \frac{(RF + LF) - (LR + RR)}{RF + RR + LF + LR} \cdot 234 + 62.5 \ \ mm \tag{4.2}$$

Table4.6: Force Plate Center of Pressure Error

Test Point	CoP (measured) [mm]		CoP Error [mm]	
	CoP_X	CoP_Y	CoP_X,err	CoP_Y,err
Point-1(0,0)	-4,1	1,5	4,1	1,5
Point-2(220,0)	222,4	0,3	2,4	0,3
Point-3(-220,0)	-220,6	4,6	-0,6	4,6
Point-4(0,290)	0,2	295,2	0,2	5,2
Point-5(0,-170)	4,1	-172,9	4,1	-2,9

The following relations were used to calculate the CoP error as % CoP error:

$$\%CoP\_X, error = \frac{(CoP\_X_{measured}) - (TestPoint\_X)}{226.5}\ mm \tag{4.3}$$

$$\%CoP\_Y, error = \frac{(CoP\_Y_{measured}) - (TestPoint\_Y)}{234}\ mm \tag{4.4}$$

The % *CoP Error* represents the CoP deviation as a percentage of the length of the force plate in the corresponding direction. According to the results presented in Table 4.7 the maximum error came out to be %1 for each direction which satisfies the design requirement.

Table4.7: Force Plate Center of Pressure % Error

Test Point	% CoP Error	
	% CoP_X,err	%CoP_Y,err
Point-1(0,0)	-0,8	0,3
Point-2(220,0)	0,5	0,1
Point-3(-220,0)	-0,1	0,9
Point-4(0,290)	0,04	1,0
Point-5(0,-170)	0,8	-0,6

CHAPTER 5

MULTI-AXES FORCE PLATE DESIGN

5.1 Literature Survey

Force plates in CDP devices are usually used for measuring the CoP. However, for general investigation of patient responses, or for research purposes, a multi-axial force plate might be required. Therefore, the force plate has to be capable of measuring all the forces and moments occuring in three axes perpendicular to each other. Considering strain gage based force plates, the patents related to multi-axes force measurements suggest to position and orient the gages, specifically. As presented in Figure 5.1 and Figure 5.2 gages are located on the pylons which form the feet of the whole structure. Each gage is applied in different direction and orientation, so that an instrument sensitive in desired directions would be obtained.

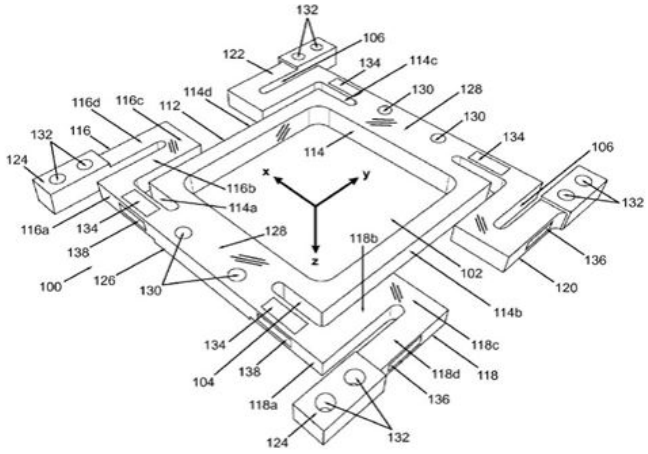

Figure 5.1: Low-Profile Transducer, Patent No: US 9,032,817 B2

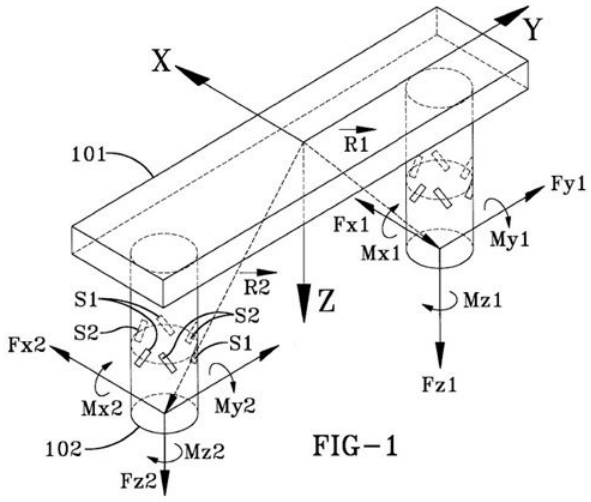

Figure 5.2: Multi-axes Transducer, Patent No: US 6,354,155 B1

The main idea is to meaure all the forces occuring in each foot by designing suitable pylons being sensitive in the three perpendicular directions, where each direction has also a different load capacity requirement.

5.2 Pylon Design

A force plate was designed for future needs of balance investigations. The design could be integrated to the CDP device or it could be used alone for biomechanical investigations. Being inspired from the patents, the design of the force plate consist of an upper plate and four feet or pylons being sensitive in vertical and horizontal directions. The pylon design can be studied as a platform or bending type load cell design. As presented in Figure 5.3 for different applications, differences in the load cell design exist. Here, in order to increase the strain magnitude and the sensitivity of the measurements, pockets may be created in different sizes and shapes.

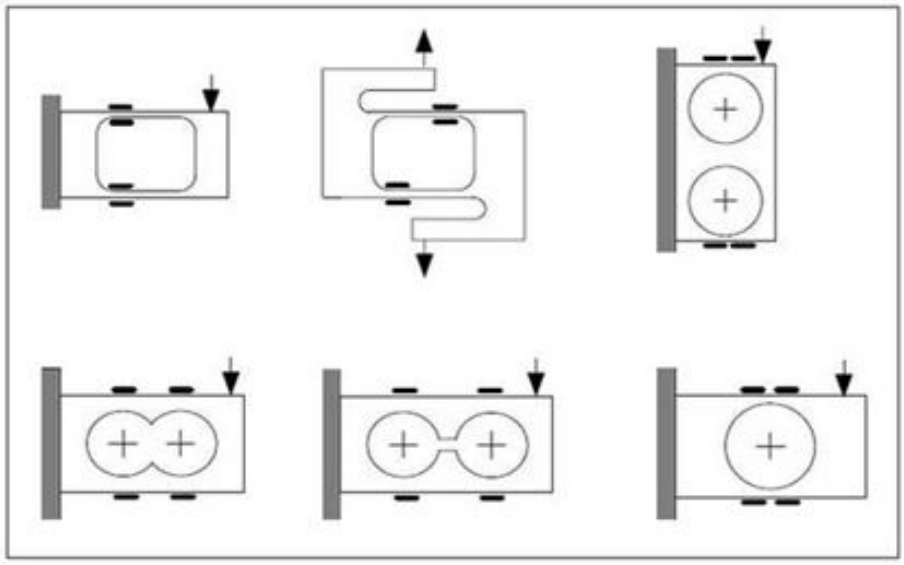

Figure 5.3: Strain-Gage Locations for Different Applications

Firstly, a custom bending type laod cell presented in Figure 5.4 was designed which was sensitive only in one direction. In order to observe cross-talk effects, the design consisted of an interface at the end tip to make a torsional force on the load-cell. The bending analysis of the load cell, which was done on a finite element analysis software, gave information about the most sensitive points on the load cell. This was later used for determining the locations of the strain gages. Figure 5.5 presents the strain distribution on the test-specimen load cell.

The red marked region is the most strained part; therefore, it is suitable to place the strain gages at that zone.

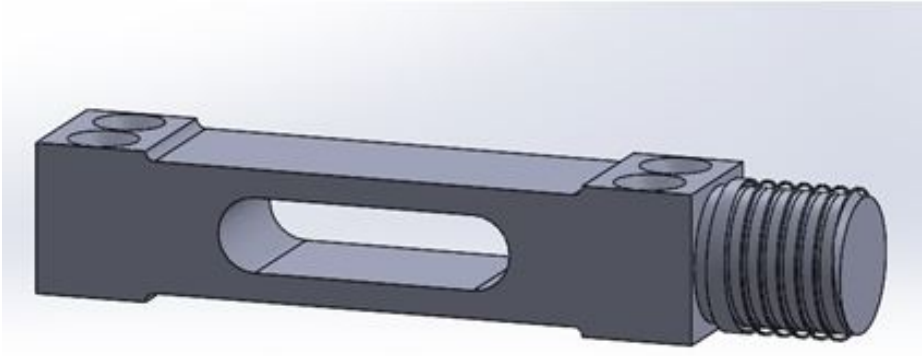

Figure 5.4: Unidirectional Custom Design Load Cell

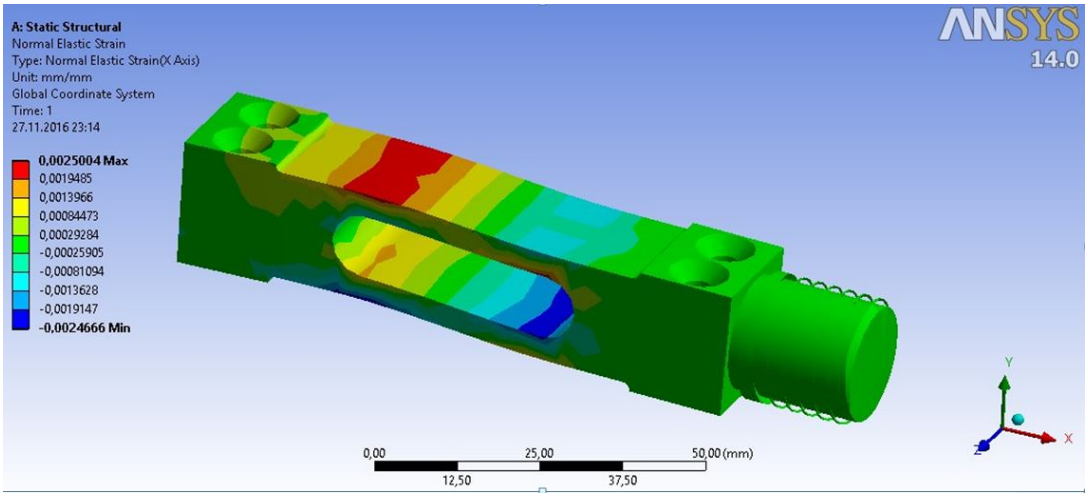

Figure 5.5: FEA of the Custom Design Load Cell

After determining the specific strain gage positions and applying them on the specimen, load tests were done to observe the linearity of the load cell. As presented in Figure 5.6 the sensor shows a high linear behaviour.

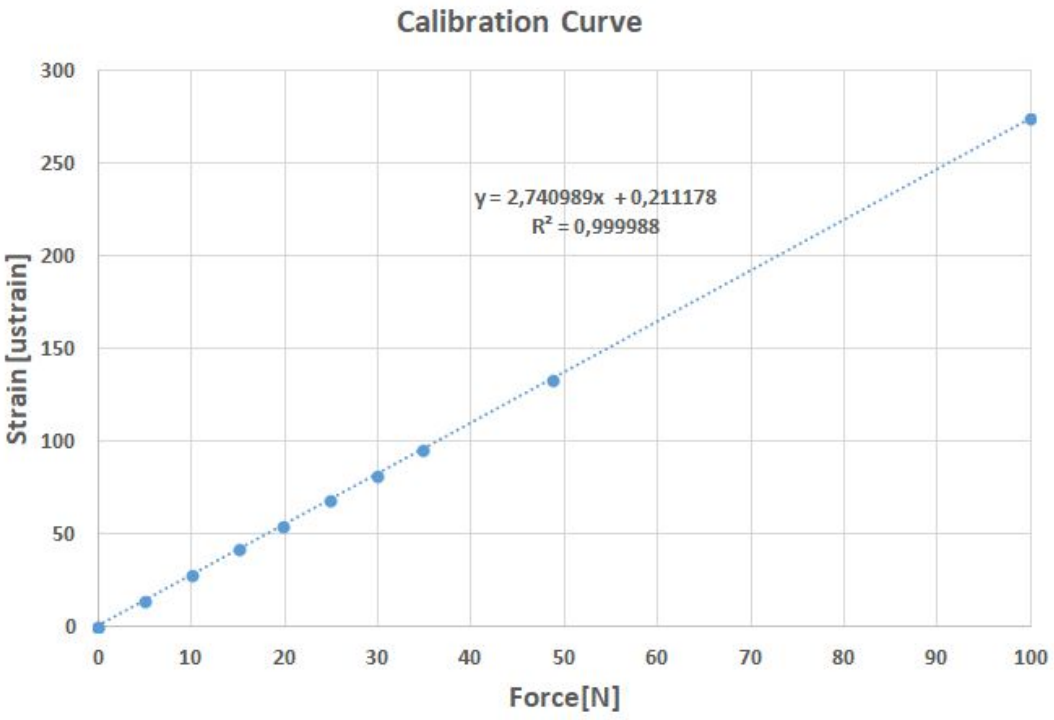

Figure 5.6: Load Test of the Custom Design Load Cell

This result encouraged for further studies on multi-axes loadcell design. Figure 5.7 presents the initial design developed to be sensitive in each three direction. The pockets are formed so that the structure becomes sensitive regions considering each load application direction. However, considering combined loading, the design must also not fail especially at critical points where the strain gages are going to be applied. The FEA presented in Figure 5.8 gives information about the results of the combined loaded pylon. In Figure 5.9 strain distribution in "y" direction under maximum combined loading is presented. Here, it has to be commented that the part design shows a too stiff behaviour which is not desirable for sensing small loads. It would be acceptable if the strain values under maximum loading be close to the limits of the strain gage and meanwhile being away from the material yield point.

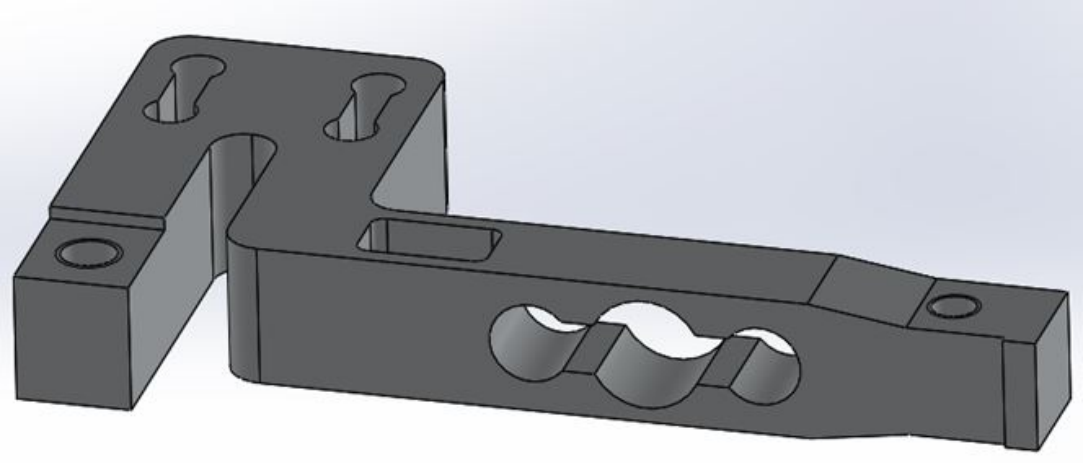

Figure 5.7: Multi-Axes Pylon Design-1

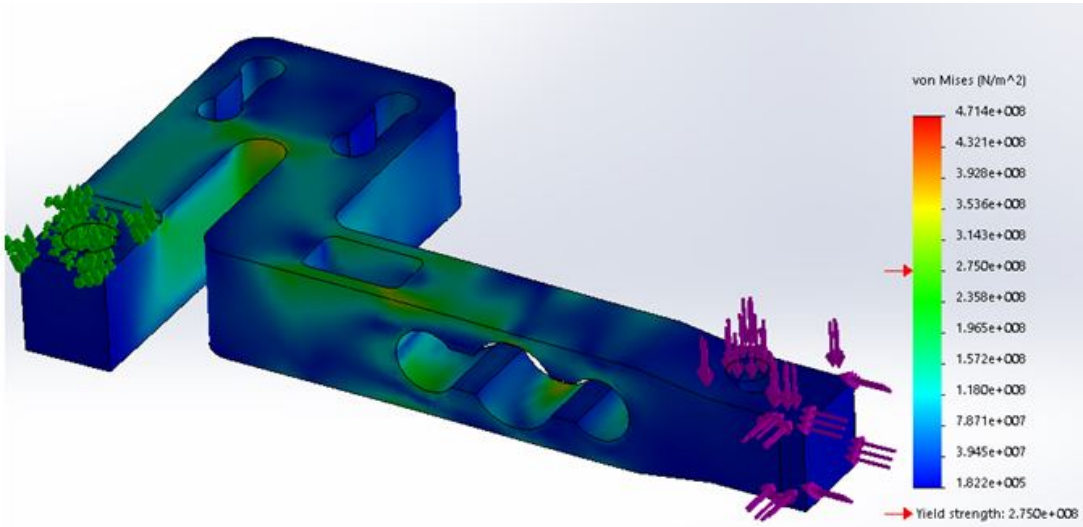

Figure 5.8: Von Mises Stress Distribution on Multi-Axes Pylon

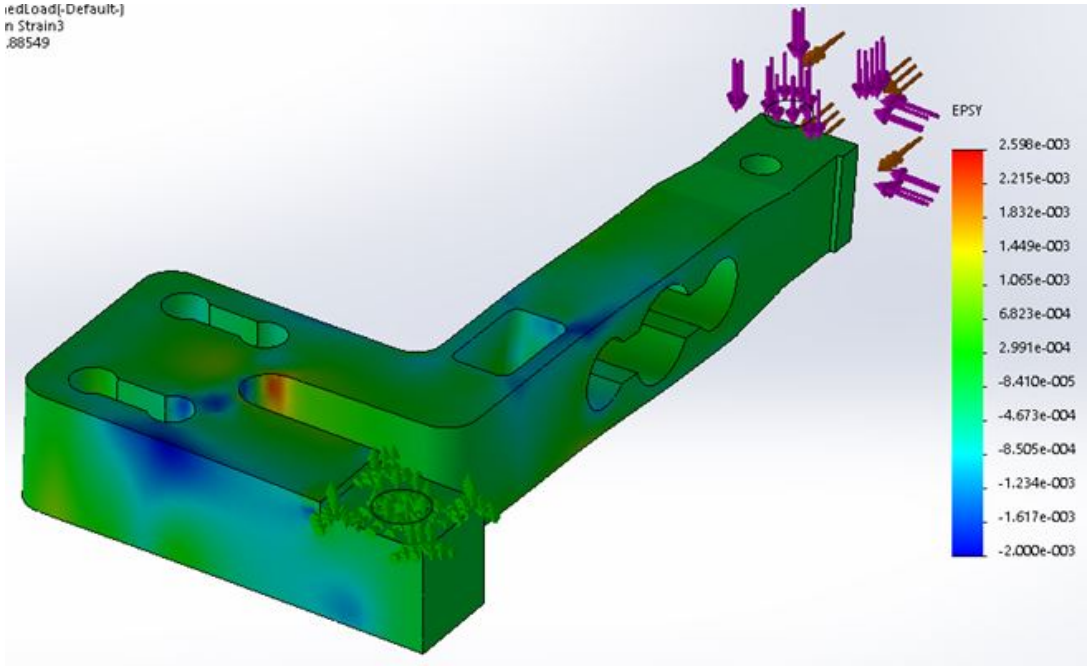

Figure 5.9: Strian in "y" Direction on Multi-Axes Pylon

5.2.1 Final Pylon Design

The final design of the pylon is presented in Figure 5.10. Again in this design, one end of the "L" shaped pylon is fixed to the ground and the other end is the part where the load is transmitted from the upper plate. The pockets are formed so that there is sufficient strain occuring under loading in the three perpendicular directions, while under combined loading no strain gage point on the pylon exceed the yield point.

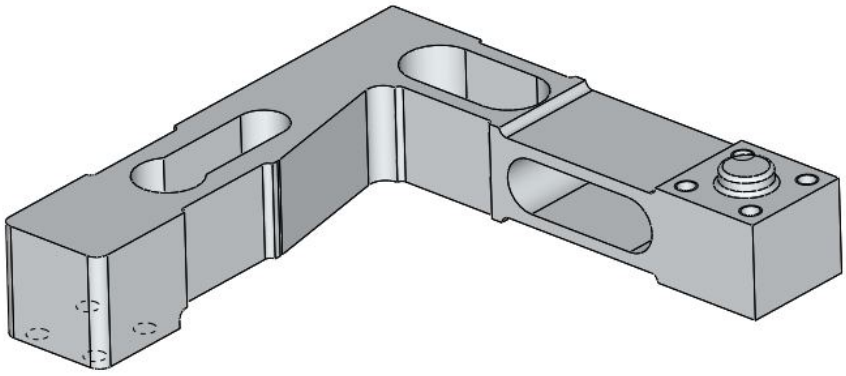

Figure 5.10: Multi-Axes Pylon Design-2

After iteratively studying the pylon for maximum strain at specific regions and no yielding under combined loading on those regions, the geometry was optimized. Considering load requirements, a vertical 1400 N in z direction and horizontal 500 N in each x and y directions were applied. Figure 5.11 presents the factor of safety distribution. The regions other than blue color indicate a yield. Hence, there is no yield at the strain gage application points under combined loading. The von-Mises stress distribution is presented in Figure 5.12, here the whole behaviour of the part under combined loading was investigated.

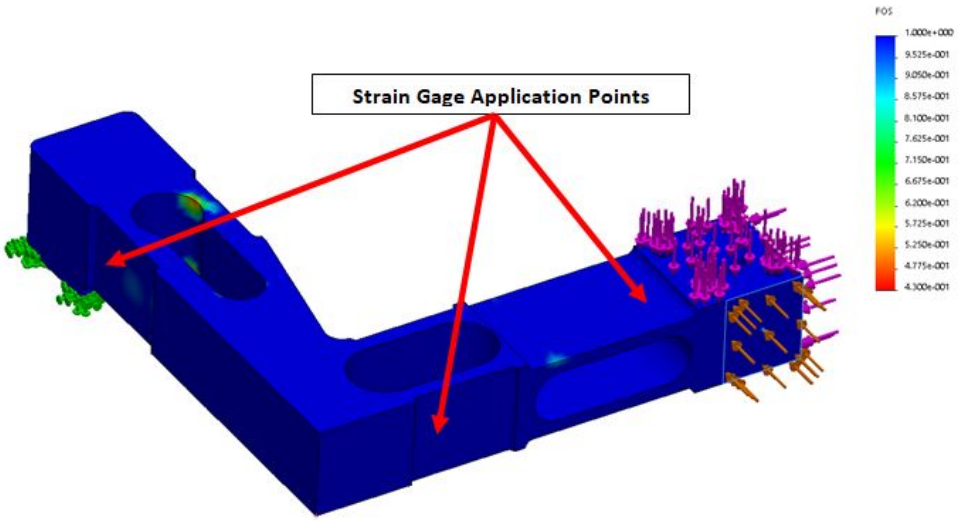

Figure 5.11: Factor of Safety of the Finalized Pylon Under Combined Load

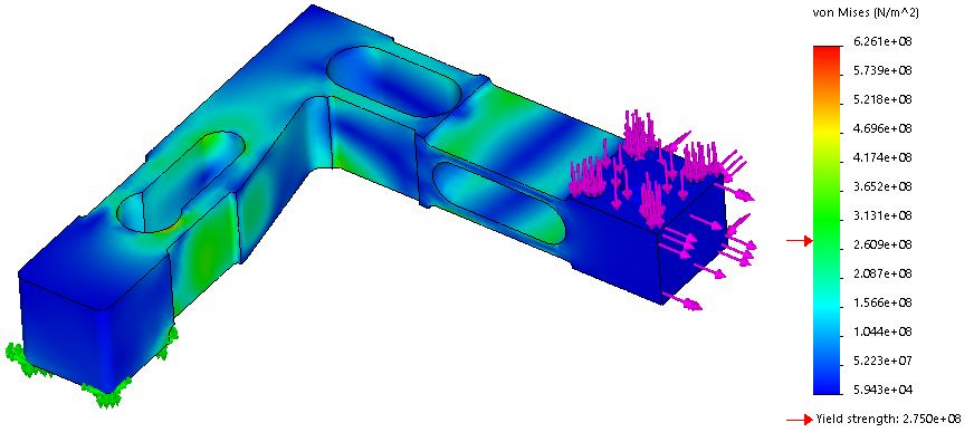

Figure 5.12: von Mises Stress Distribution of the Finalized Pylon Under Combined Load

In order to observe the strainig and failure status of the points at which the strain gages are going to be applied, load analysis in each direction was done one by one.

Applying only a vertical 1400 N load in z direction on the pylon, Figure 5.13 presents the strain distribution in the corresponding direction. Here, approximately a maximum 4500 ustrain occurs which is about 15% of the strain gage limit. The von Mises stress distribution is presented in Figure 5.14. The stress distribution shows high equivalent dispersion at points where the strain gages forming a full bridge are to be applied for the vertical load. This will enable to make more accurate measurements and healthier comments on the measured data.

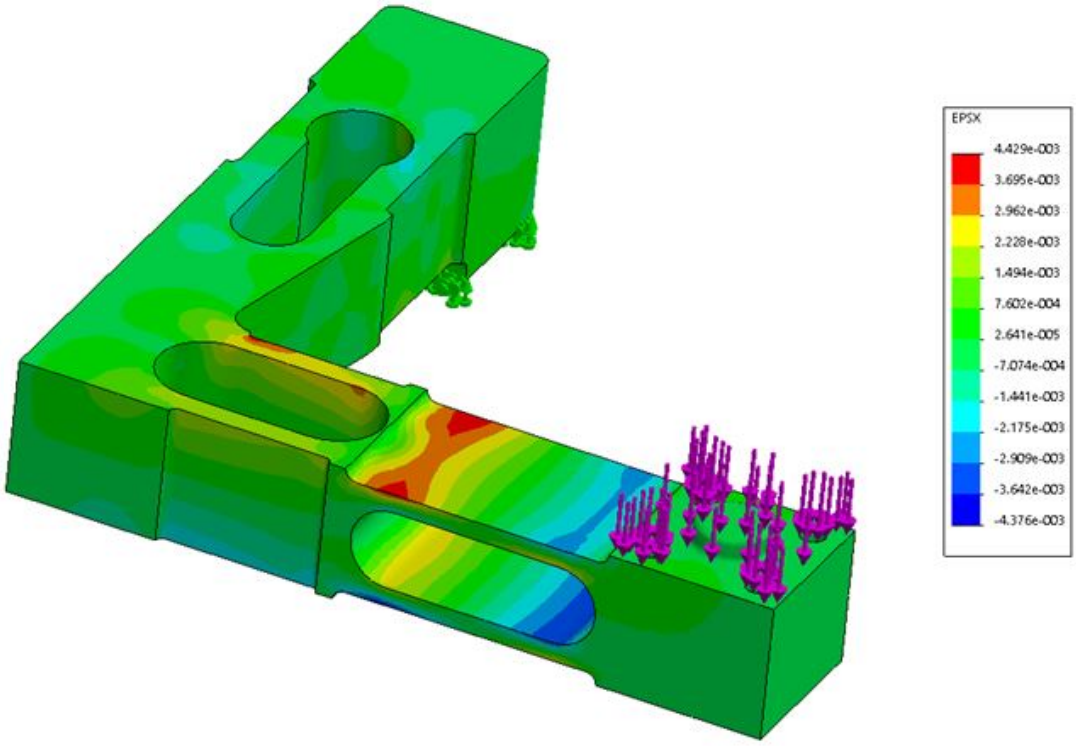

Figure 5.13: Strain in Finalized Pylon Under z Vertical Load

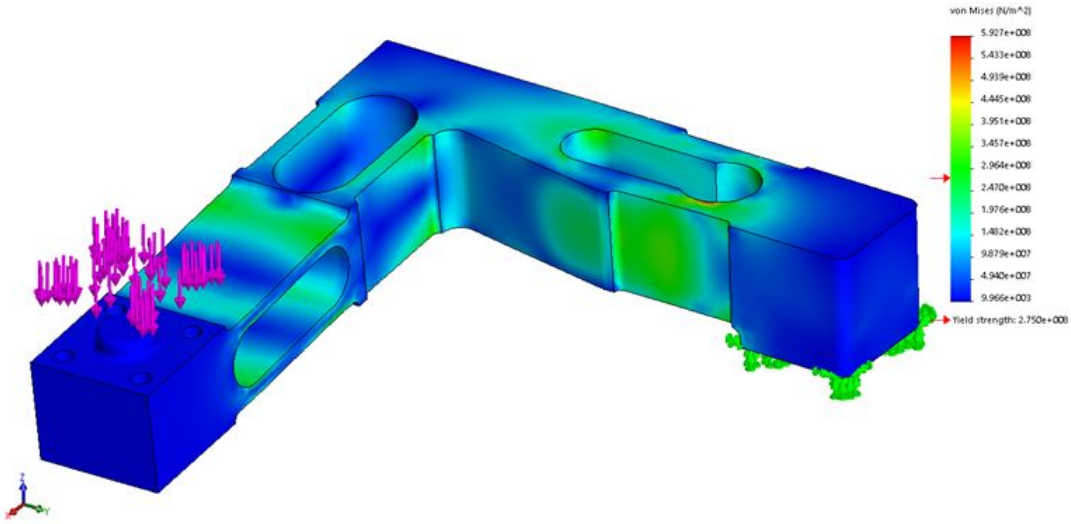

Figure 5.14: von Mises Stress Distribution of the Finalized Pylon Under Vertical Load

Similarly, horizontal loads were applied and the stress and strain status was analyzed. Presented in Figure 5.15 and Figure 5.16, 500 N load in x and y directions were applied on the pylon.

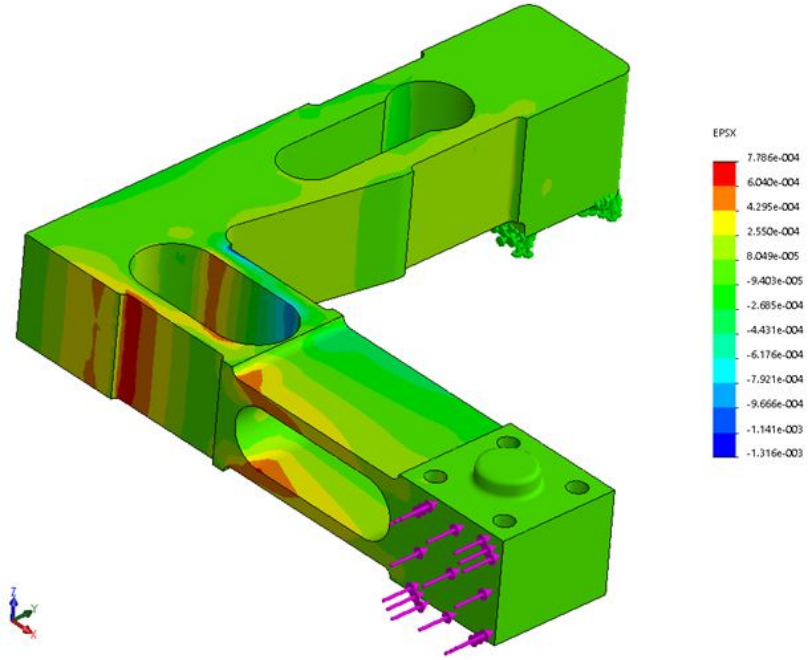

Figure 5.15: Strain in Finalized Pylon Under x-Horizontal Load

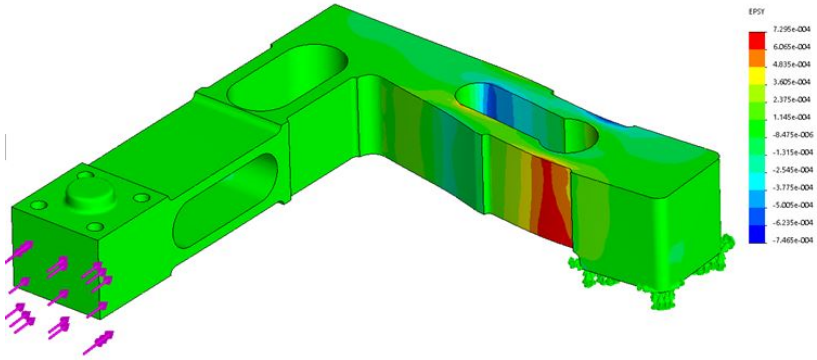

Figure 5.16: Strain in Finalized Pylon Under y-Horizontal Load

According to the analysis, there would be approximately 780 ustrain occuring at the zone the strain gage measuring the forces applied in horizontal y direction and approximately 730 ustrain in horizontal x direction. To summarize, the proposed pylon satisfies the loads in three directions and the strains that occur

on it at particular zones would be sufficient for the measurements. Therefore, a structure could be build on the pylons forming the force plate.

5.3 Force Plate Structure

As discussed earlier, the multi-axes force plate consists of a rigid upper plate and four pylons at the corners supported from the ground. As presented in Figure 5.17 and Figure 5.18 the force plate can be seen in the assembled and exploded view.

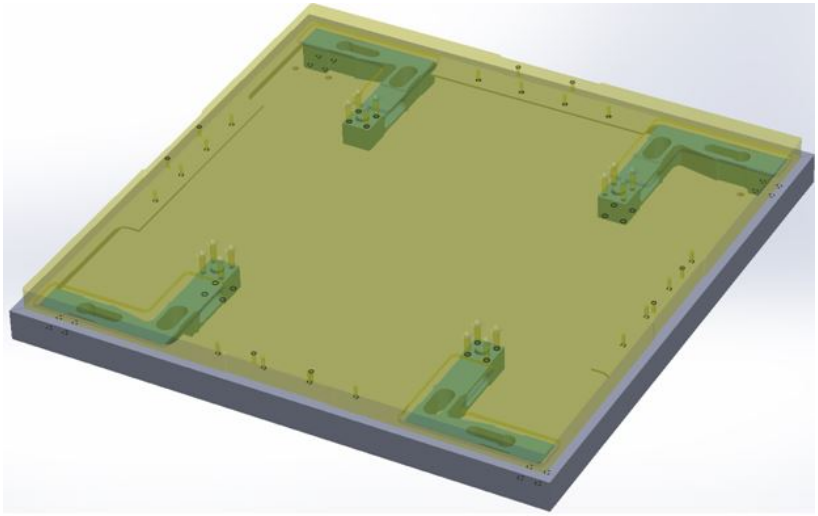

Figure 5.17: Multi-Axes Force Plate Structure

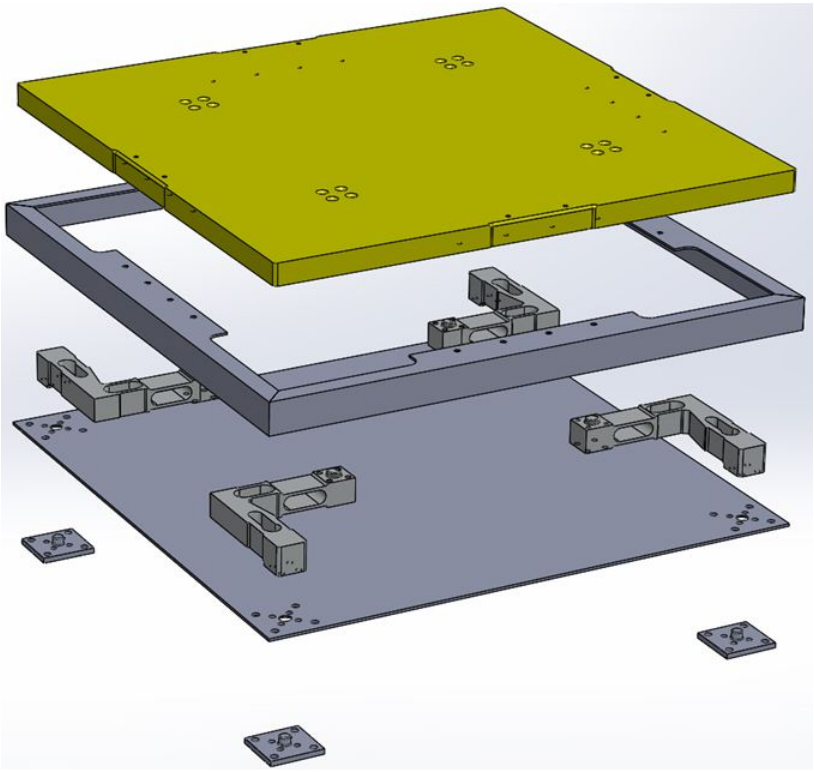

Figure 5.18: Multi-Axes Force Plate Structure

To calibrate the force plate and obtain the calibration matrix, a simple tool was also designed. In Figure 5.19 the assembled view of the force plate and the tool is presented. Here, the tool is supposed to be used for applying horizontal loads.

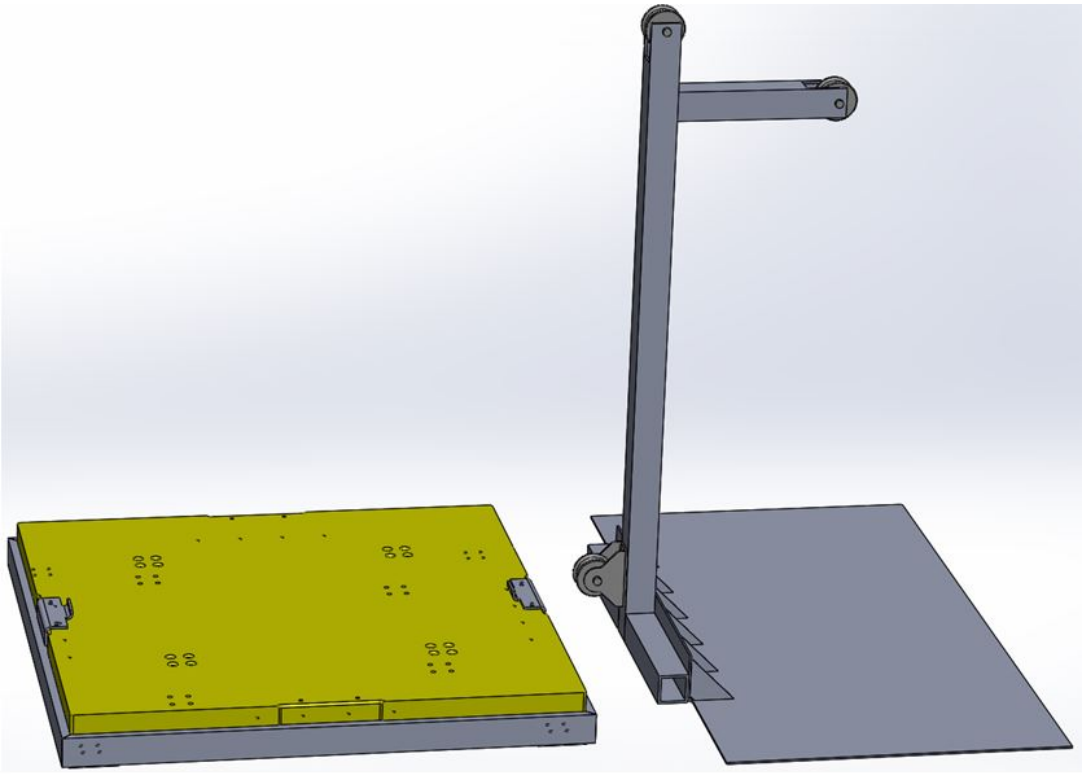

Figure 5.19: Calibration Tool of the Force Plate

5.3.1 Crosstalk Analysis

After the production of the pylon and instrumentation with strain gages, force measurements were done by applying loads in three perpendicular directions, seperately. Each time, the outcomes of each full bridge numbered as channels 1, 2 and 3 were noted. The results show that especially when loads are applied in horizontal directions there is some crosstalk. In Figure 5.20 the axes and the gage location regions are defined.

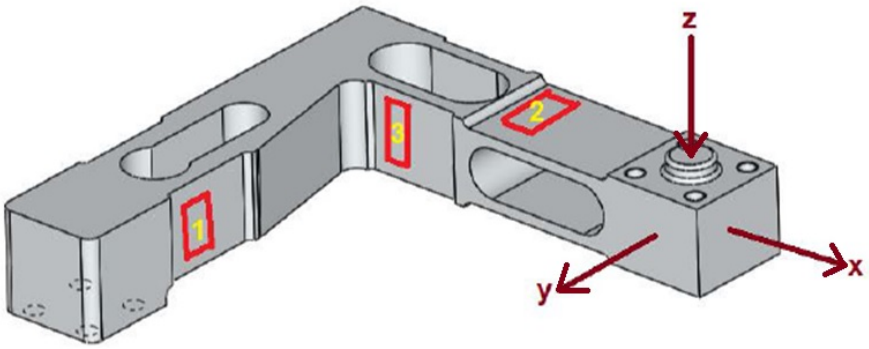

Figure 5.20: Definition of Pylon Axes and Gage Locations

The following figures show the loading outcomes in each direction and the outputs of the off-axis channels. Under the loads in z-direction, the measurement results were noted as given in the following plot in Figure 5.21. The sensitive bridge in z-direction, numbered as channel 2, shows high linearity. The other bridges which are sensitive in the horizantal loads also give some output, however the outcomes of the sensitive vertical channel over the horizantal ones are too dominant. Hence loadings in z-direction have low crosstalk.

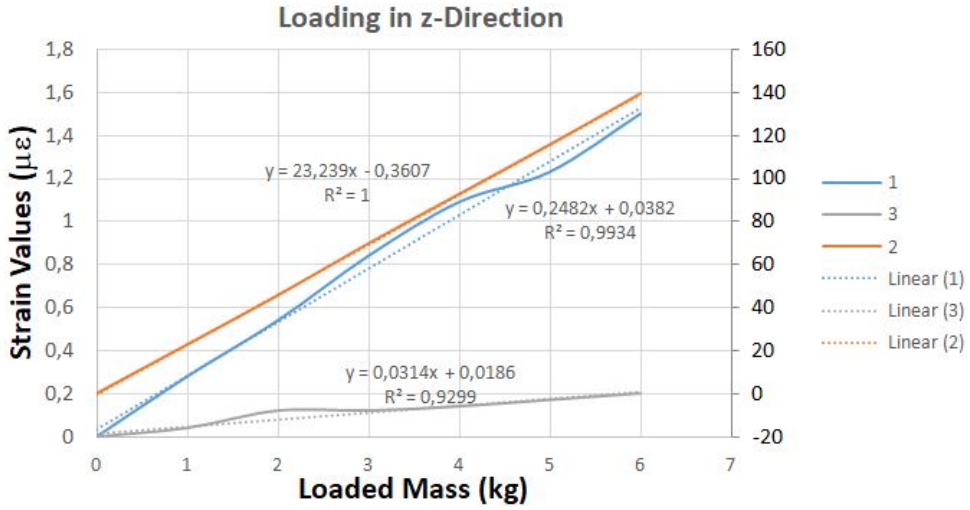

Figure 5.21: Outputs of the channels when loaded in z-Direction

The results of loading the pylon in y-direction is presented in Figure 5.22. According to the results, when the pylon is loaded in y-direction the channels for

measuring the loads in y-direction and in x-direction give output, together.

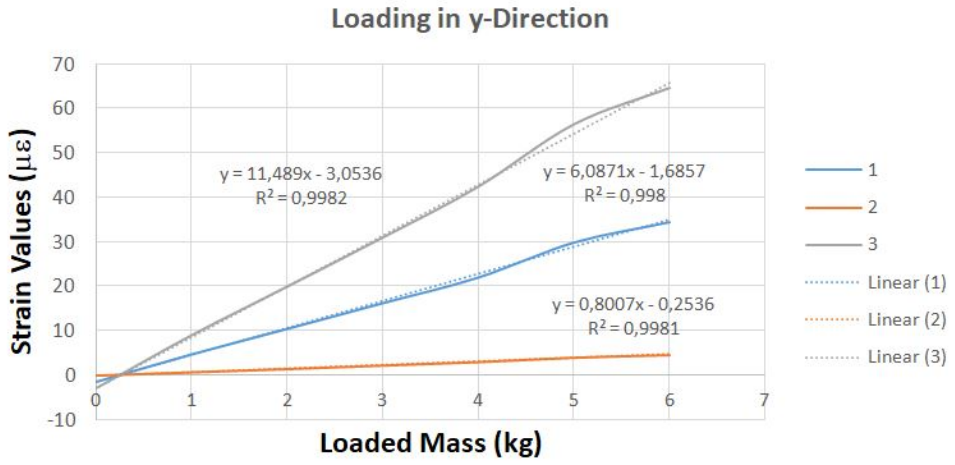

Figure 5.22: Outputs of the channels when loaded in y-Direction

The results of loading the pylon in x-direction is presented in Figure 5.23. According to the results, when the pylon is loaded in x-direction there is low crosstalk over channel-3 but the cross-sensitivity in channel-2 has to be lowered.

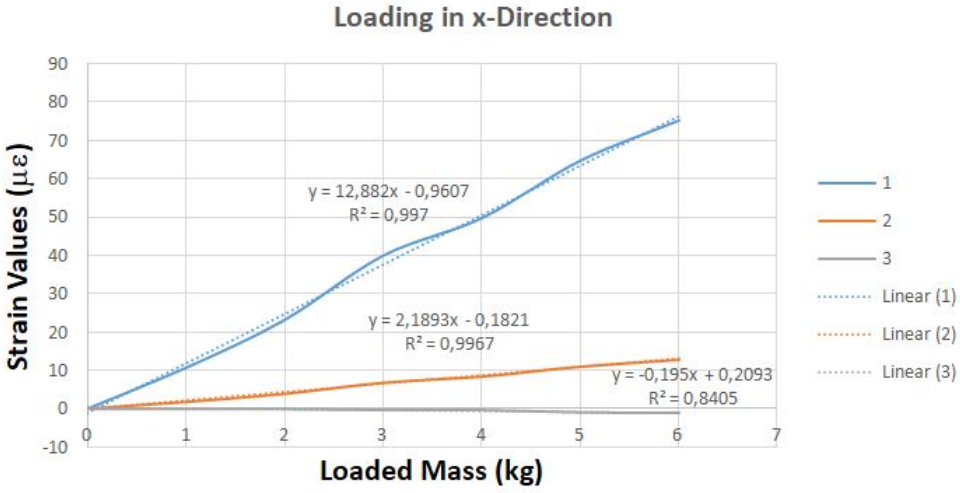

Figure 5.23: Outputs of the channels when loaded in x-Direction

According to the measrurements the calibration matrix is formed as in Figure 5.24.

Channel		1	3	2
K	x-measr	12,882	-0,195	2,1893
	y-measr	6,0871	11,489	0,8007
	z-measr	0,2482	0,0314	23,239

Figure 5.24: Calibration Matrix

The values in the matrix indicated with red are the cross-sensitivity values which have to be eliminated. Therefore, a study explained in next sections in detail was done to lower these values. Here, theoretically by doing finite element analysis the gage locations were altered so that the cross-talk effects were lowered at the end. New theoretical points were selected on the FEA model and recorded. Here by selecting the new points the main parameter was the symmetry of the strain values under loadings.

5.3.1.1 Applying 1 N Force in Vertical z-Direction

Finite element analysis was done to observe behaviour of the pylon under different loads acting in different directions. Also the strain values at the points where the strain gages are applied were also investigated. Applying a unit load in the finite element analysis in z-direction, the results came out to be approximately 5% different than the measurement, which is evaluated as satisfactory. Figure 5.25 shows the finite element analysis results, the indicated nodes are the points where the strain gages were applied. The strain values came to be (2.505 e-6), (2.388 e-6), (-2.524 e-6) and (-2.414 e-6).

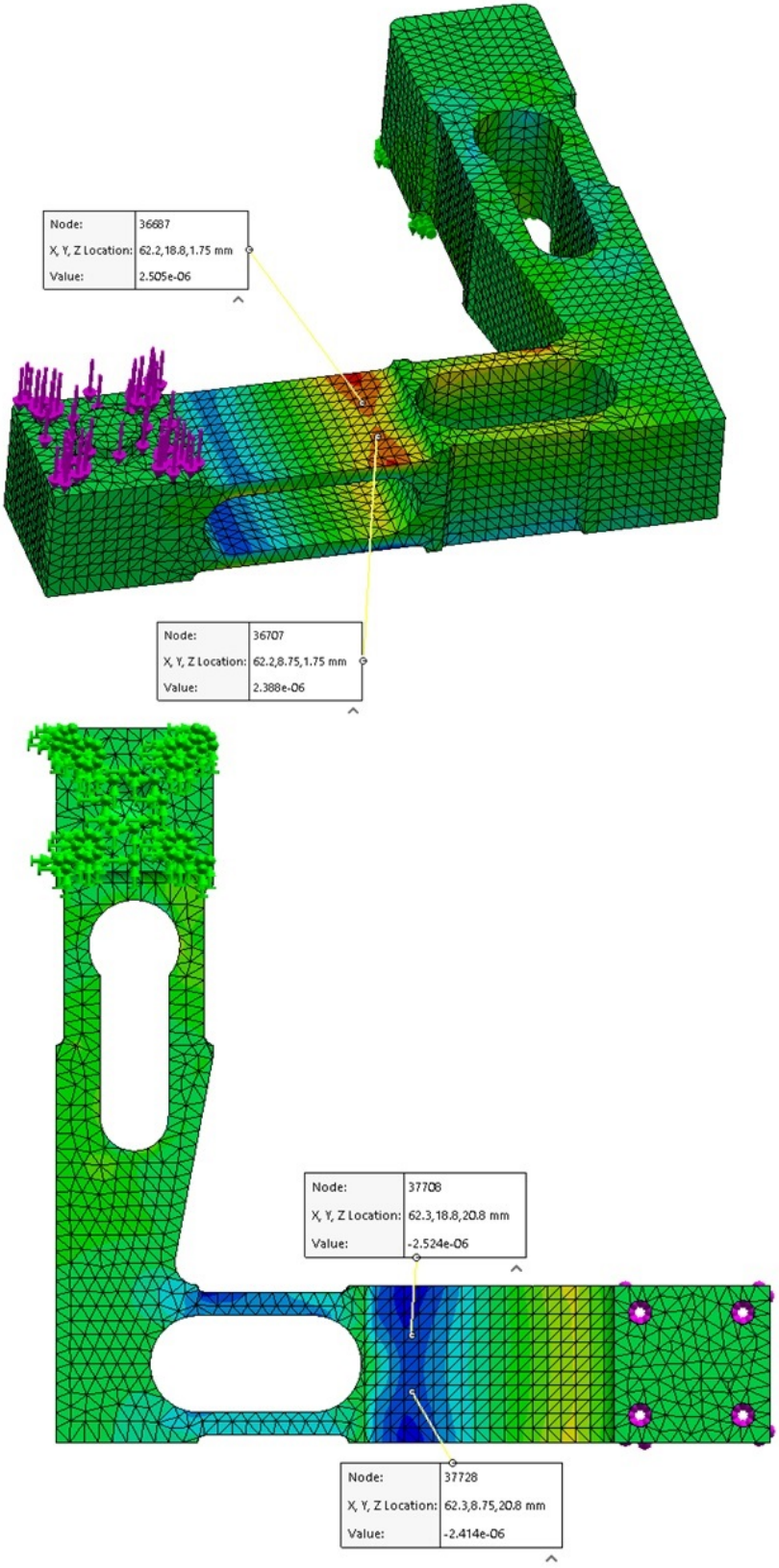

Figure 5.25: FEA Results in z-Load in Channel-2

As the measurements showed that there was a cross sensitivity in channel-2 especially when loaded in x-direction, new gage locations were investigated. At the end, new points for channel-2 expressing increased straining symmetry were selected as shown in Figure 5.26. New strain values came to be (2.423 e-6), (2.388 e-6), (-2.444 e-6) and (-2.414 e-6).

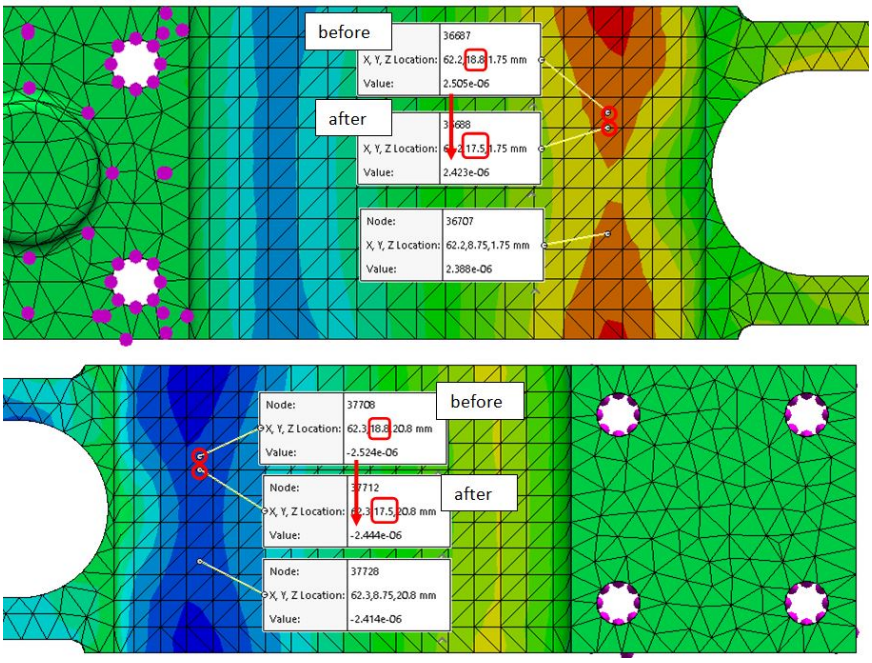

Figure 5.26: New Gage Locations for Channel-2

Under the load in z-direction, the strain values in channel-2 were also observed in the finite element analysis. The strain values came to be (9.671 e-7), (-9.699 e-7), (5.997 e-7) and (-5.998 e-7) as shown in Figure 5.27. The strain values at gage positions for channel-3 are very symmetric, hence there was no need to relocate the gages.

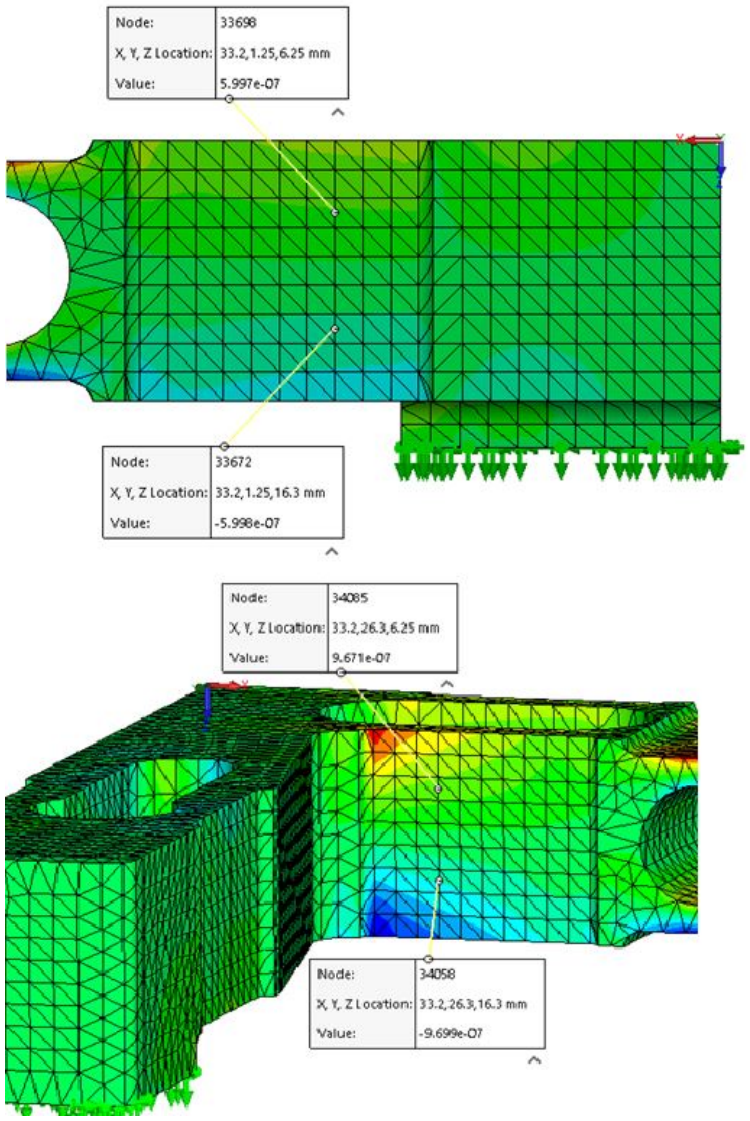

Figure 5.27: FEA Results under z-Load in Channel-3

The results on channel-1 came out to be also non-symmetric. Hence, relocation of the gages were done. In Figure 5.28 the original and the modified gage loacations and the strain values are indicated. The former strain values were (-5.162 e-7), (3.298 e-7), (-2.138 e-7) and (1.634 e-7). Later, the values become (-5.162 e-7), (5.200 e-7), (-2.138 e-7) and (-2.424 e-7).

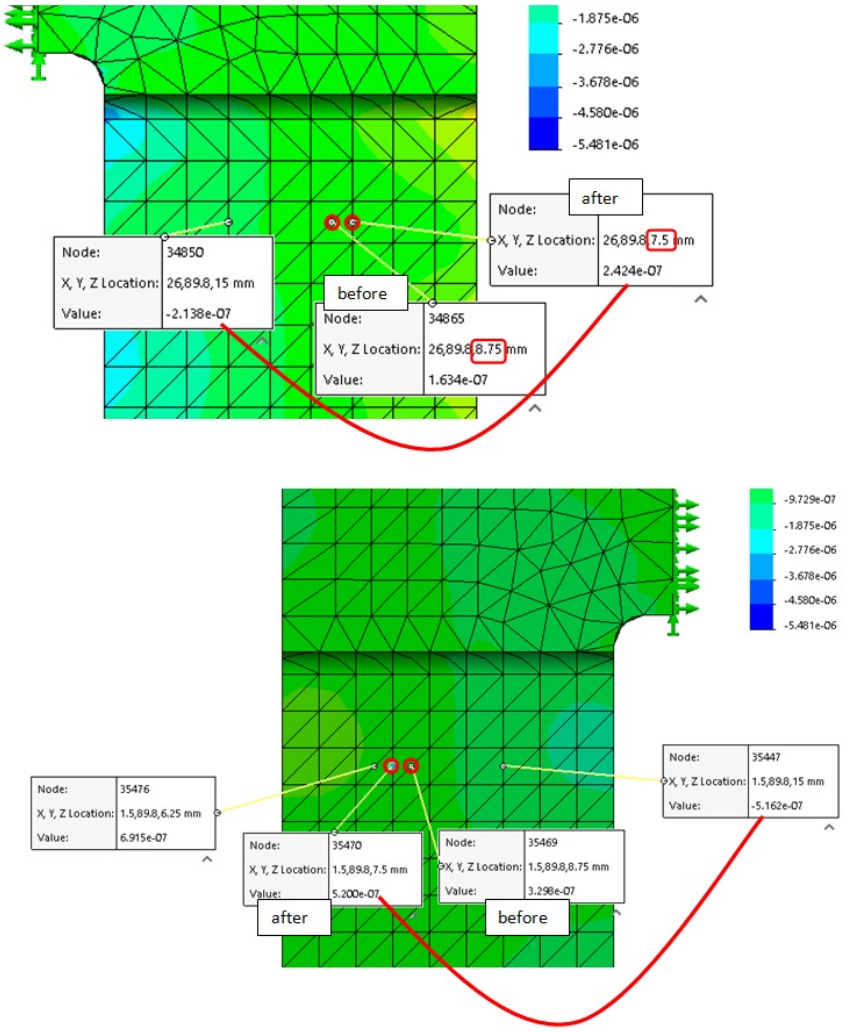

Figure 5.28: FEA Results under z-Load in Channel-1

5.3.1.2 Applying 1 N Force in Horizontal x-Direction

Finite element analysis was also done by applying a unit load in x-direction. With the relocation of the gages on channel-1 the straining state is shown in Figure 5.29. The strain values for Channel-1 changed from (1.322 e-6), (1.261 e-6), (-1.340 e-6) and (-1.280 e-6) to (1.322 e-6), (1.252 e-6), (-1.340 e-6) and (-1.273 e-6). The results show that also the gage positions were changed due to the cross-senstivity under the loading in z-direction, it did not affect the channel in its sensitive direction.

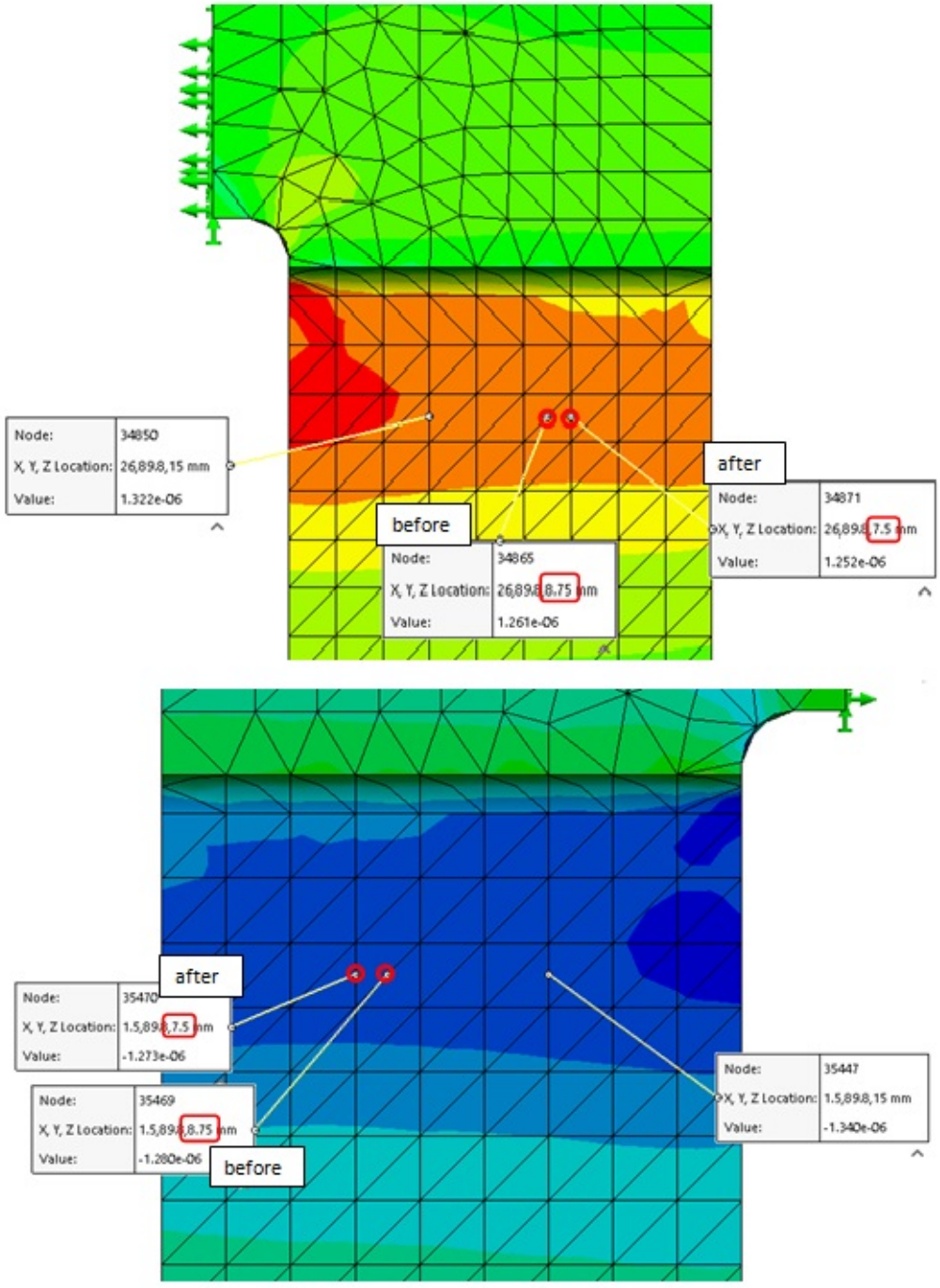

Figure 5.29: Results under x-Load for New Gage Locations of Channel-1

Under the load applied in x-direction the strain values in channel-2 came out to be as in Figure 5.30. The strain values for Channel-2 changed from (-5.089 e-8),

(-5.359 e-8), (-5.167 e-8) and (-5.077 e-8) to (-5.089 e-8), (-4.411 e-8), (-5.167 e-8) and (-4.302 e-8). The results show that the change in the gage positions due to the cross-senstivity has decreased the sensitivity in x-direction.

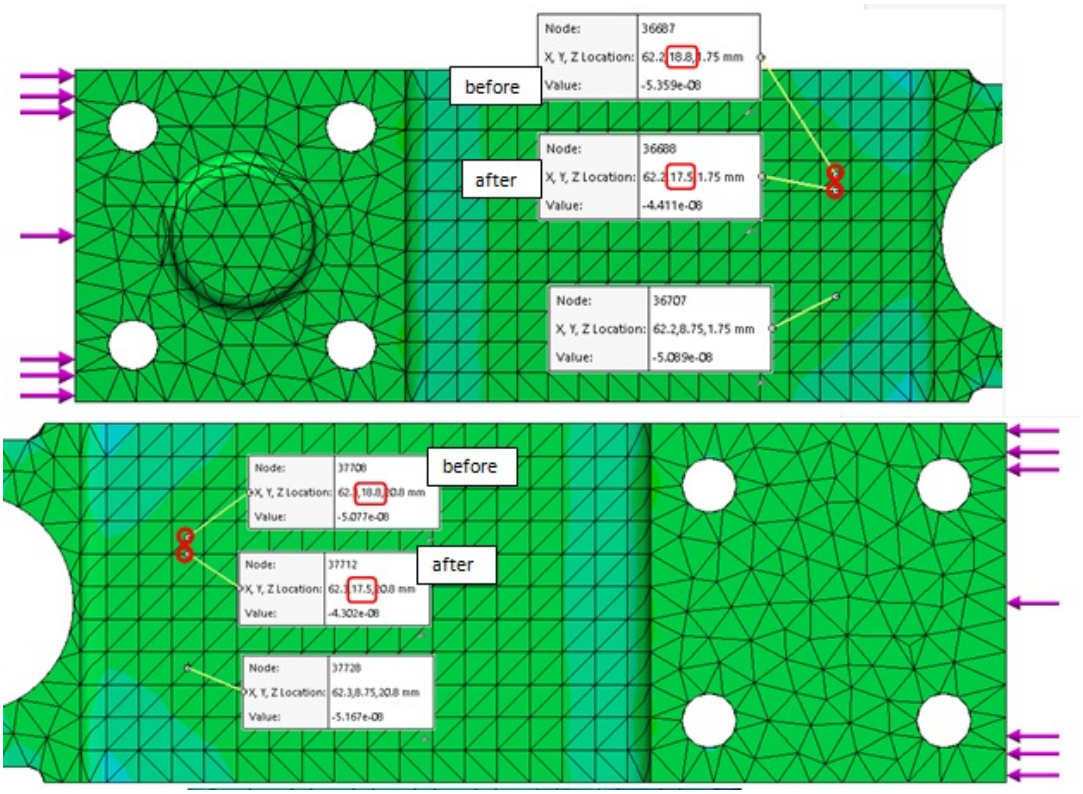

Figure 5.30: Results under x-Load for New Gage Locations of Channel-2

5.3.1.3 Applying 1 N Force in Horizontal y-Direction

Finally, finite element analysis was performed by applying a unit load in y-direction. The channel-3 strain values came out to be (-1.339 e-6), (-1.331 e-6), (8.683 e-7) and (8.686 e-7).

The strain values in channel-2 have changed from (2.890 e-7), (-3.580 e-7), (2.901 e-7) and (-3.444 e-7) to (2.890 e-7), (-2.837 e-7), (2.901 e-7) and (-2.765 e-7) under the applied load in y-direction as given in Figure 5.31.

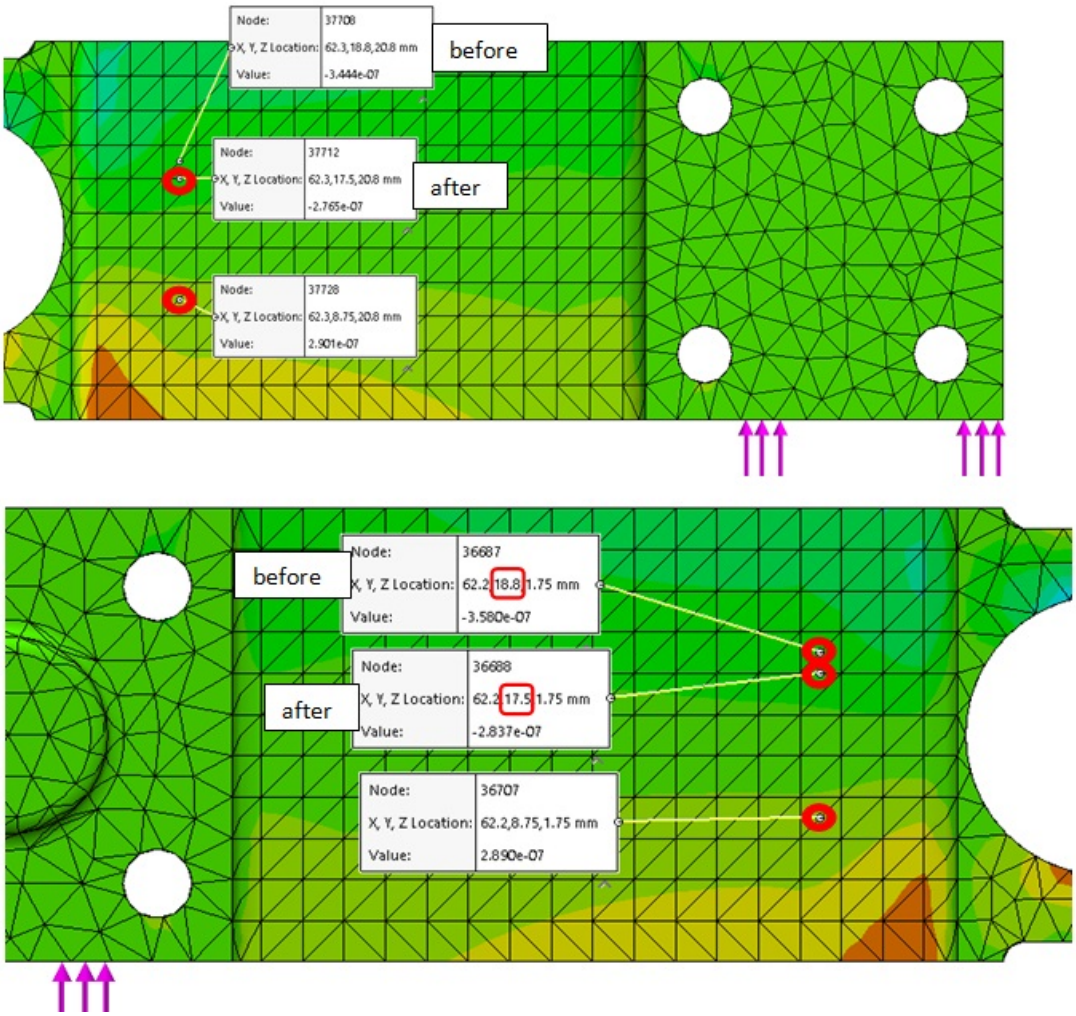

Figure 5.31: Results under y-Load for New Gage Locations of Channel-2

Similarly, the strain values in channel-1 have changed from (-8.553 e-7), (-7.838 e-7), (4.562 e-7) and (-3.444 e-7) to (-8.553 e-7), (-7.816 e-7), (4.458 e-7) and (-2.765 e-7) under the applied load in y-direction as given in Figure 5.32.

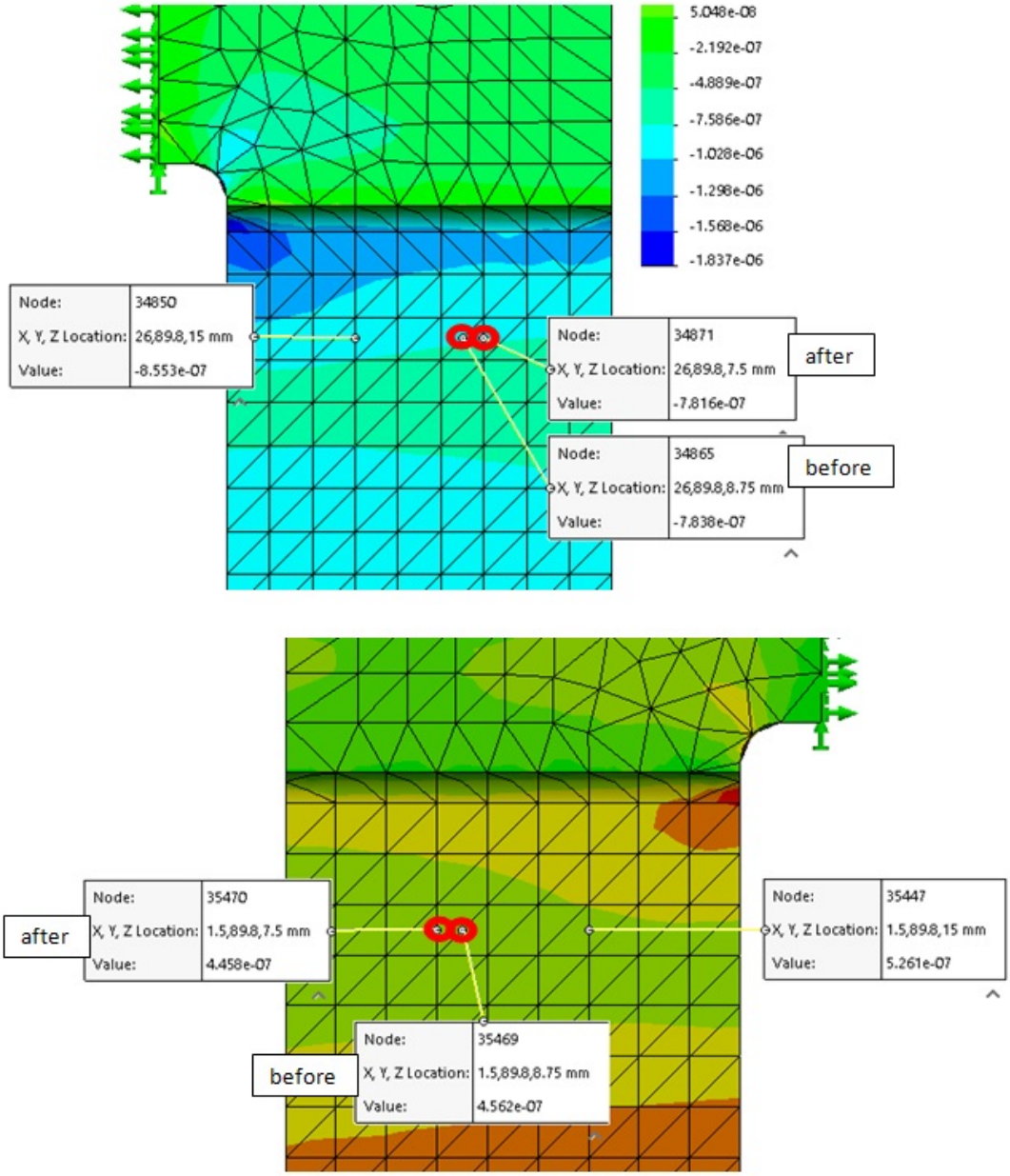

Figure 5.32: Results under y-Load for New Gage Locations of Channel-1

According to the finite element analysis, cross-sensitivity of the pylon was decreased. Then, the theoretically calculated calibration matrix became as given in Figure 5.33

Channel		1	3	2
K_corr_th	x-measr	12,842	-0,195	0,3327
	y-measr	6,0578	11,489	0,4521
	z-measr	0,0453	0,0314	22,856

Figure 5.33: Theoretically Calculted New Calibration Matrix

5.3.2 Pylon Measurements

After finding the new strain-gage application positions, the gages were bonded. All the pylons were instrumented with transducer-class gages which were bonded with a special adhesive (M-Bond 600) and cured in an oven for an hour at 130° C. The gaugwa were wired to full bridge, as presented in Figure 5.34. Here, by forming the circuit, the position of the gages were placed so that the gages under same loading condition have the same sign in the circuit.

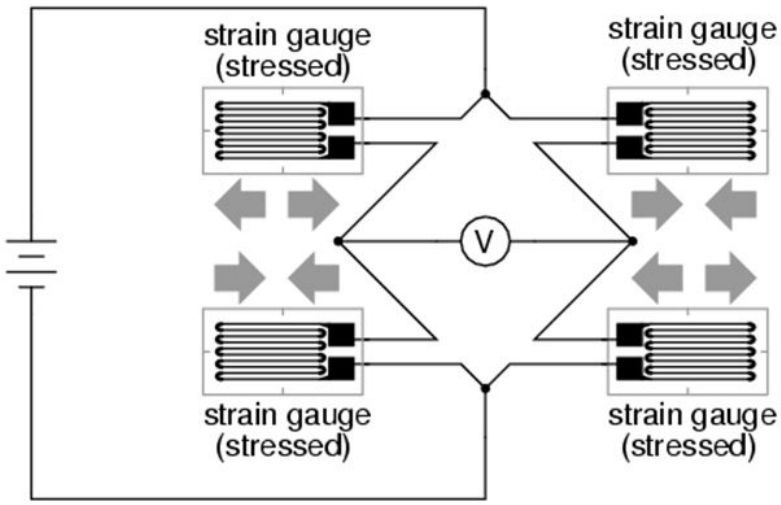

Figure 5.34: Wheatstone Bridge Full Bridge Configuration

After the instrumentation of all the four pylons, each was tested. Loads were applied from 0 to 6 kg in each x, y and z direction. For each loading direction, outputs of each pylon channels; x (series 1), y (series 2), z (series 3) were

recorded. As an example, the behaviour of Pylon #3 loaded in x-direction is presented in Figure 5.35. (All the measurement results are presented in the Appendix.)

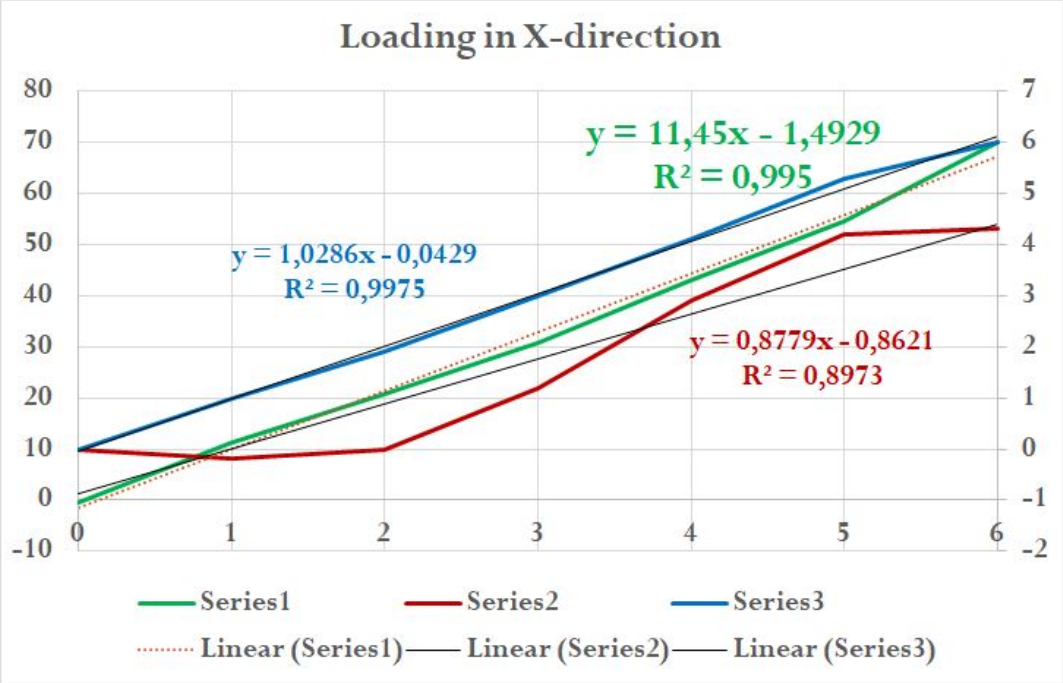

Figure 5.35: Loading of Pylon #3 in x-Direction

All the measurements are summarized in Figure 5.36. The results show that after the FEA, cross-sensitivity was reduced in X over Z and Y over Z. There is 1-3% cross-sensitivity in Z-direction. The cross-sensitivity of Y over Z is approximately 5%. Under Y-loading there is also signal on Channel-X as a result of the design. Finally, in x-direction 7% cross-sensitivity exists.

		Pylon # Test	Pylon # 1	Pylon # 2	Pylon # 3	Pylon # 4
Load-x	c_x	12.882	-	-7.3357 (4V)	11.45	13.036
	c_y	-0.195	-	-0.2207	0.8779	0.9896
	c_z	2.1893	-	-2.1643	1.0286	0.5357
Load-y	c_x	6.0871	-	-3.5714 (4V)	6.9107	6.56
	c_y	11.489	11.282	-11.593	-11.468	-12.032
	c_z	0.8007	-0.335	-0.4896	-0.5704	-0.8679
Load-z	c_x	0.2482	-	0.385 (4V)	0.8821	0.1568
	c_y	0.0314	0.3896	0.2914	-0.0207	-0.2232
	c_z	-23.239	24.257	23.93	24.029	23.475

Figure 5.36: Pylon Measurement Results

5.3.3 Platform Measurements

After assembling the whole structure, load was applied on the upper plate in vertical and horizontal directions. In Figure 5.37, the loading points are presented, through points 1 to 4 vertically and at the sides, horizontally.

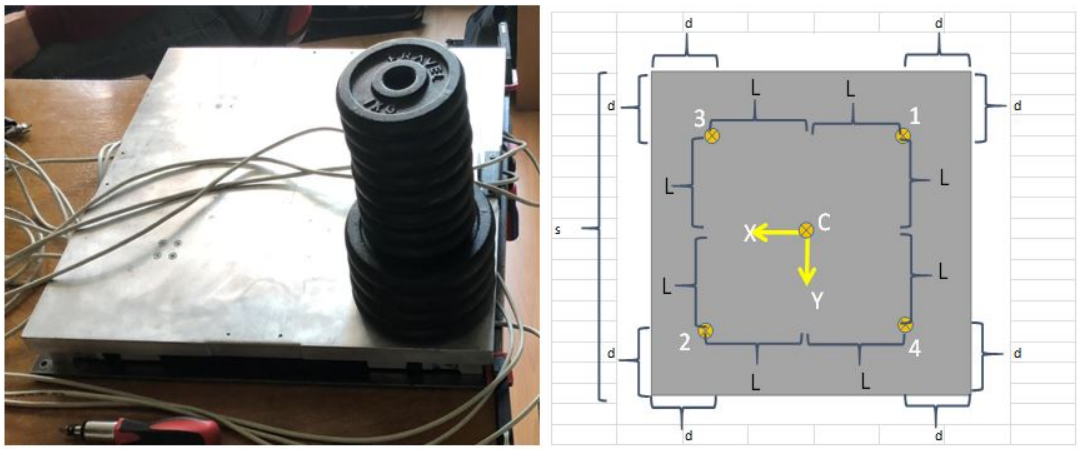

Figure 5.37: Platform Loading Points

Having total 12 channels, three for each pylon, all the axes of the pylons were connected to the data acquisition system given in Figure 5.38. Hence, all the signals in total 12 channels were measured at the same time. In vertical direction, loads were applied beginning from 2 kg up to 16 kg and in horizontal direction 1 kg up to 6 kg.

Figure 5.38: Data Acquisition System

For each loading point, data obtained from the 12 channels were recorded. All the measured data can be seen in the Appendix. Considering the signs according to Figure 5.37, moment signals were created by the following formulas:

For Point #1;

$$M_x = F \cdot L = C_{M,x} \cdot (S_{z1} + S_{z3} - S_{z2} - S_{z4}) \tag{5.1}$$

$$M_y = -F \cdot L = C_{M,y} \cdot (-S_{z1} + S_{z3} + S_{z2} - S_{z4}) \tag{5.2}$$

For Point #2;

$$M_x = -F \cdot L = C_{M,x} \cdot (S_{z1} + S_{z3} - S_{z2} - S_{z4}) \tag{5.3}$$

$$M_y = F \cdot L = C_{M,y} \cdot (-S_{z1} + S_{z3} + S_{z2} - S_{z4}) \tag{5.4}$$

For Point #3;

$$M_x = F \cdot L = C_{M,x} \cdot (S_{z1} + S_{z3} - S_{z2} - S_{z4}) \tag{5.5}$$

$$M_y = F \cdot L = C_{M,y} \cdot (-S_{z1} + S_{z3} + S_{z2} - S_{z4}) \tag{5.6}$$

For Point #4;

$$M_x = -F \cdot L = C_{M,x} \cdot (S_{z1} + S_{z3} - S_{z2} - S_{z4}) \tag{5.7}$$

$$M_y = -F \cdot L = C_{M,y} \cdot (-S_{z1} + S_{z3} + S_{z2} - S_{z4}) \tag{5.8}$$

In Figure 5.39 the outcome of all the measurements is presented.

Loading Reults.jpg

	Point	C_Mx	C_My	C_x	C_y	C_z
z-load	1	8,491	5,941	-3,085	-5,987	16,761
	2	8,289	6,348	-2,637	-0,997	16,415
	3	8,462	6,540	-2,243	-1,502	16,977
	4	7,809	5,488	-4,356	-6,315	16,130
	C	-	-	-4,079	-5,757	16,070
	ave	8,263	6,079	-3,280	-4,112	16,471
	std dev	0,315	0,467	0,911	2,626	0,394
x-load	Shear x	-	-	-1,329	-3,032	-0,166
y-load	Shear y	-	-	-0,438	3,197	-0,067

Figure 5.39: Platform Loading Reults

It can be said that as it is also for the pylon itself, the most sensitive direction is the Z-direction. The sensitivities in X and Y directions are similar. The linearity is also outstanding for most of the cases. However, crosstalk exists at a higher level than the pylon itself.

CHAPTER 6

RESULTS & DISCUSSION

A prototype of the proposed design was produced and the CDP tests were implemented. The selection of mechanism types, machine elements and sensors has satisfied the design requirements. As presented in the Verification Chapter, the sensitivity of the force plate as well as the servo controlled motion axes came out to be within the limits of the specified tolerances. All these outcomes encourage the device to be used in hospitals and physical therapy centers for the assessment and rehabilitation of balance disorders. On the other hand, the ML rotary motion axis has already attracted some medical doctors working in the field, audiology and balance problems. The device will enable the medical doctors to develop new standards on balance tests in ML direction.

Furthermore, for rehabilitation purposes some games have been developed. Here, the patient orients himself/herself on a rough country which is visualised on the LED screen and walks through the paths with the help of the force plate. At the same time the platform gets the corresponding inclination angle of the surface in pitch and roll directions (AP and ML rotations), so the patient will be exposed to a hardware supported virtual reality application. This would help the patients to overcome daily life balance problems.

For future work, new rehabilitation applications will be developed for different patients facing with different types and levels of balance disorders. Moreover, in order to obtain and evaluate more general responses of the patients on the force plate, the multi-axis force plate would be integrated on the device.

For the multiaxis force plate studies, the geometry of the pylon was the main parameter, obviously. Considering stress distributions on the parts and always seeking the elastic region was studied. However, although later it was tried to place the gages not on the geometrically symmetric points but to the strain symmetric locations on the pylons, still errors existed. Several factors like mis-positioning the gages, clamping pressure differences during curing, improper curing temperatures and durations might be the basic error sources for the pylons. Still within a limit, all the pylons gave similar outputs as indicated in the tables. For the assembled case, the platform had error factors like; distributing the applied force from the upper plate to the pylons, the interfaces between them was not ideal. This might cause a different channel to act instead of the real one. Moreover, especially for the shear loads where dead weights were hanging by a wire-pulley apparatus, the pulley frictions and the stability of the apparatus itself was a major error source. In short, pylon, platform, mechanical interface design optimizations can be studied for better sensitivity, linearity and less crosstalk.

REFERENCES

[1] NA, *Postural Sway.* https://cecs.anu.edu.au/research/student-research-projects/postural-sway-and-machine-learning, Retrieved April 2018.

[2] A. L. McDonough, *Balance and Posture.* www.nyu.edu/classes/mcdonough/Balance-and-Posture.ppt, Retrieved April 2018.

[3] A. L. McDonough, *Balance and Posture.* www.nyu.edu/classes/mcdonough/Balance-and-Posture.ppt, Retrieved April 2018.

[4] F. O. B. Marry Ann Watson, "The human balance system - a complex coordination of central and peripheral systems," *Vestibular Disorders Association*, vol. S-7, pp. 22–30, 2008.

[5] NA, "Sensory organization test," *resourcesonbalance.com/program/role/cdp/ protocols.aspx*, Retrieved April 2018.

[6] S. I. R. Thomas C. Adams, Derek G. Kamper, "A low-cost portable system for the assessment of the postural response of wheelchair users to perturbations," *IEEE Transactions on Rehabilitation Engineering*, vol. 7, no. 4, pp. 435–442, 1999.

[7] M. P. D Kamper, K Barin, "Preliminary investigation of the lateral postural stability of spinal cord-injured individuals subjected to dynamic perturbations," *Spinal Cord*, vol. 37, pp. 40–46, 1999.

[8] H. M. V. d. L. Patrick A. Forbes, Billy L. Luu and E. A. C. et al., "Transformation of vestibular signals for the control of standing in humans," *The Journal of Neuroscience*, vol. 36, no. 45, pp. 11510–11520, 2016.

[9] NA, "Neurocom smart equitest cdp," *www.natus.com*, Retrieved May 2018.

[10] NA, "Neurocom smart equitest cdp," *https://www.slapsale.com/1-neurocom-smart-equitest-system-x-121708*, Retrieved June 2018.

[11] NA, "Bertec balance advantage – dynamic cdp," *http://bertec.com/bertecbalance/our-products/dynamic/*, Retrieved May 2018.

[12] NA, "Synapsys posturography system – dynamic sps," *https://synapsys.fr/en/produit/dynamic-sps/*, Retrieved May 2018.

[13] NA, "Kistler force plate brochure," *https://www.kistler.com/en/applications/sensor-technology/biomechanics-and-force-plate/*, Retrieved June 2018.

[14] NA, "Straingage drawing," *https://www.mtiinstruments.com/wp-content/uploads/2018/03/Drawing-of-foil-type-strain-gauge.png*, Retrieved June 2018.

[15] NA, "Amti force plate brochure," *http://www.amti.biz*, Retrieved June 2018.

[16] NA, "A primer on the design and use of strain gage force sensors," *https://www.interfaceforce.com/*, Retrieved June 2018.

[17] J. K. N. Richard G. Budynas, *Shigley's Mechanical Engineering Design*. McGraw-Hill Education, 2015.

[18] N. A. Bernstein, *Dexterity and Its Development*. NA: Lawrence Erlbaum Associates, Inc., 1996.

[19] M. L. Latash and V. M. Zatsiorsky, *Biomechanics and Motor Control, Defining Central Concepts*. London: Elsevier, 2016.

[20] V. M. Zatsiorsky, *Kinamatics of Human Motion*. Champaign, IL: Human Kinetics, 1998.

[21] W. M. Shumway-Cook A, *Motor Control: Theory and Practical Applications*. Philadelphia: Lippincott: Williams and Wilkins, 2001.

[22] S. Rader, *A Systems Model of Balance*. NA: NA, 2016.

[23] H. H. S. Joseph C. Arezzo and P. S. Spencer, "Structure and function of the somatosensory system: A neurotoxicological perspective," *Environmental Health Perspectives*, vol. 44, pp. 22–30, 1982.

[24] P. Chieyeko Tsuchitani, "Somatosensory systems," *https://nba.uth.tmc.edu/neuroscience/s2/chapter02.html*, Retrieved April 2018.

[25] T. M. Lorenz Assländer, Georg Hettich, "Visual contribution to human standing balance during support surface tilts," *Human Movement Science*, vol. 41, pp. 147–164, 2015.

[26] A. P. N. S. Marialuisa Gandolfi, Christian Geroin and M. Bartolo, "Assessment of balance disorders," *Advanced Technologies for the Rehabilitation of Gait and Balance Disorders, Biosystems and Biorobotics*, vol. 19, pp. 47–67, 2018.

[27] F. B. Horak, "Clinical assessment of balance disorders," *Gait and Posture*, vol. 6, pp. 76–84, 1997.

[28] H. F. Shumway Cook A, "Rehabilitation strategies for patients with vestibular deficits," *Neurol Clin*, vol. 8, pp. 441–57, 1990.

[29] L. M. Nashner, "Sensory feedback in human posture control," *Doctor of Science Thesis, Department of Aeronautics and Astronautics, MIT*, p. 3, 1970.

[30] B. FO, "Clinical status of computerized dynamic posturography in neurotology," *urrent Opinion in Otolarynogol Head Neck Surg*, vol. 9, pp. 314–318, 2001.

[31] C. Harstall, *Dynamic Posturography in the rehabilitation of stroke, brain injured and amputee patients.* Edmonton, Alberta, CANADA: Alberta Heritage Foundation for Medical Research, 1998.

[32] F. B. H. Laurie A. King, "Lateral stepping for postural correction in parkinson's disease," *Arch Phys Med Rehabil*, vol. 89, pp. 492–499, 2008.

[33] E. T. Ahmet Ufuk Çuvalcı, "Design of a force plate for biomechanical usage," *Conference Proceeding book of the 8th National Biomechanical Congress, Turkey*, p. 114, 2016.

[34] M. R. Ramey, "Force plate designs and applications," *Exercise and Sport Sciences Reviews*, vol. 3, no. 1, pp. 303–320, 1975.

[35] S. Pugh, *Total Design: Integrated Methods for Successful Product Engineering.* Addison-Wesley Publishing Company, 1990.

[36] C. C. Martin Monteiro and A. C. Marti, "Acceleration measurements using smartphone sensors: Dealing with the equivalence principle," *Brazilian Journal of Physical Education*, vol. 37, no. 1303, March 2015.

APPENDIX A

A.1 Servo System

The servo system consists of the four servo motor drivers and a controller. The controller communicates over ethernet with the operating computer and with the drivers over EtherCat connected in series. The main scheme of the architecture is as presented in Figure A.1.

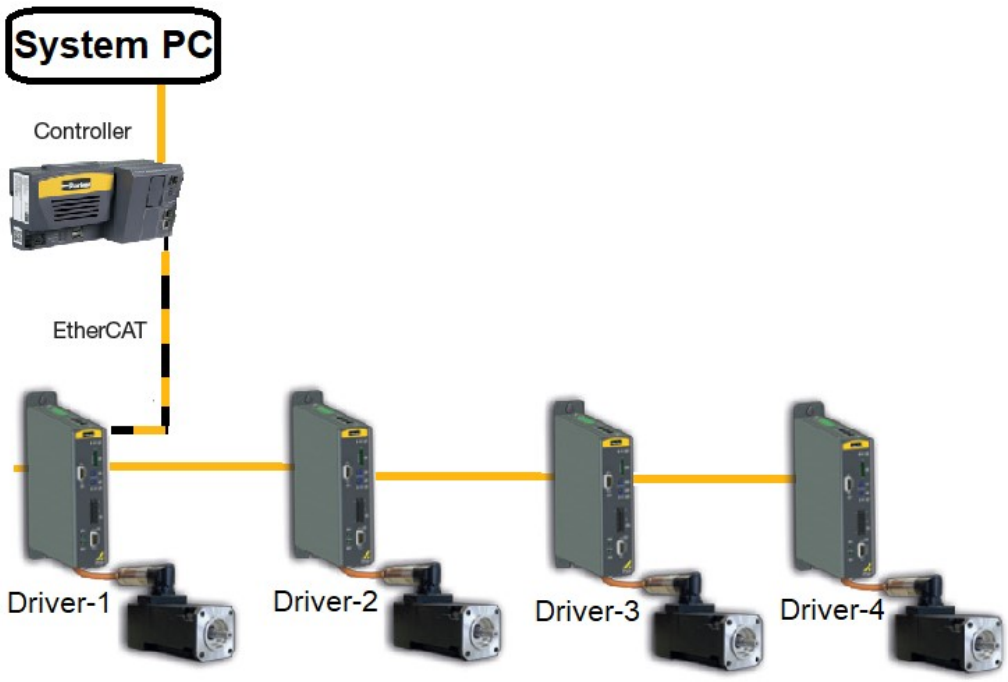

Figure A.1: Servo System Architecture

APPENDIX B

B.1 Arduino Code for Ultrasonic Sensor

The following script was embedded in Arduino for translation motion measurement with an ultrasonic sensor HC-SR04.

```
int trigPin = 12; // Trigger
int echoPin = 11; // Echo
long duration, mm, inches;
void setup() {
//Serial Port begin
Serial.begin (9600);
//Define inputs and outputs
pinMode(trigPin, OUTPUT);
pinMode(echoPin, INPUT);
}
void loop() {
// The sensor is triggered by a HIGH pulse of 10 or more microseconds.
// Give a short LOW pulse beforehand to ensure a clean HIGH pulse:
digitalWrite(trigPin, LOW);
delayMicroseconds(5);
digitalWrite(trigPin, HIGH);
delayMicroseconds(10);
digitalWrite(trigPin, LOW);
```

```
// Read the signal from the sensor: a HIGH pulse whose
// duration is the time (in microseconds) from the sending
// of the ping to the reception of its echo off of an object.
pinMode(echoPin, INPUT);
duration = pulseIn(echoPin, HIGH);

// Convert the time into a distance
mm = (duration/2) / 2.91; // Divide by 2.91 or multiply by 0.0343
//inches = (duration/2) / 74; // Divide by 74 or multiply by 0.0135

//Serial.print(inches);
//Serial.print("in, ");
Serial.print(mm);
//Serial.print("mm");
Serial.println();

delay(5);
}
```

APPENDIX C

C.1 Pylon & Platform Measurements

Pylon #1

Results of loading in Y-Direction is presented in Figure C.1

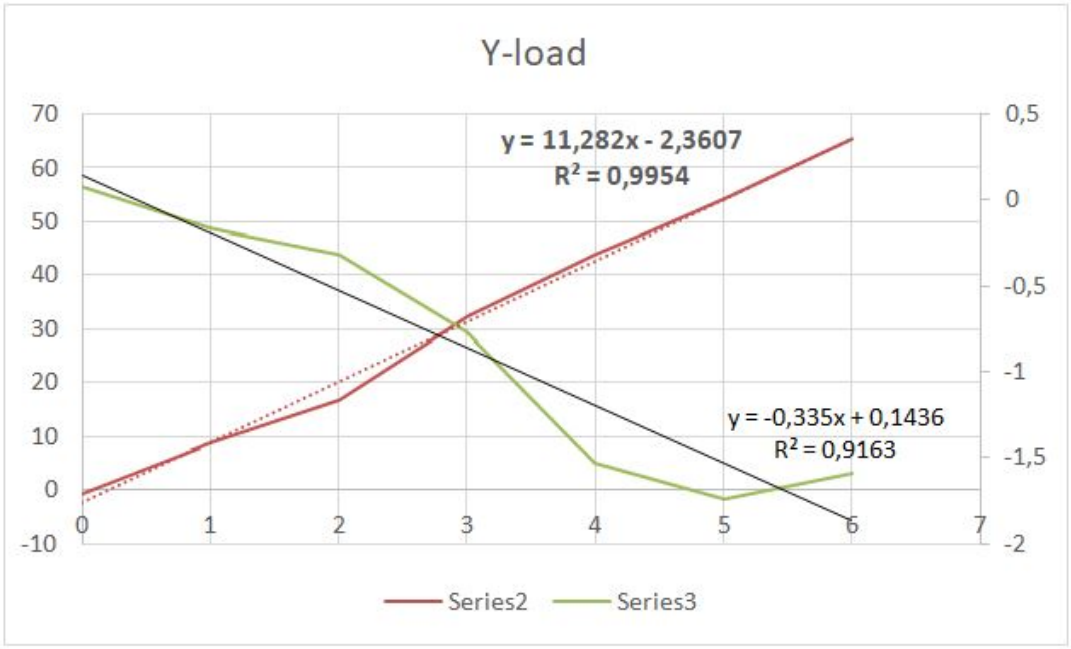

Figure C.1: Outputs Under Loading in Y-Direction

Pylon #1

Results of loading in Z-Direction is presented in Figure C.2

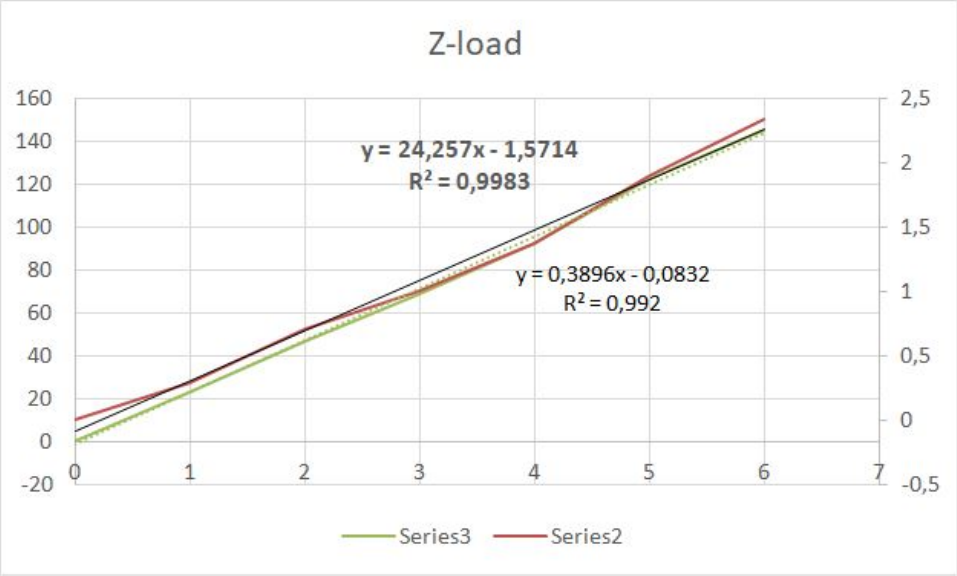

Figure C.2: Outputs Under Loading in Z-Direction

Pylon #2

Results of loading in X-Direction is presented in Figure C.3

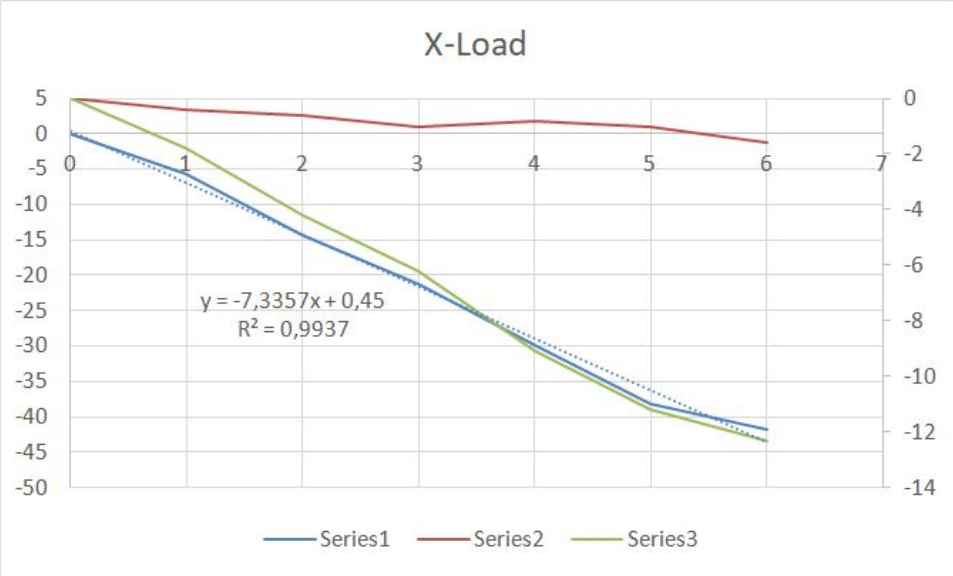

Figure C.3: Outputs Under Loading in X-Direction

Pylon #2

Results of loading in Y-Direction is presented in Figure C.4

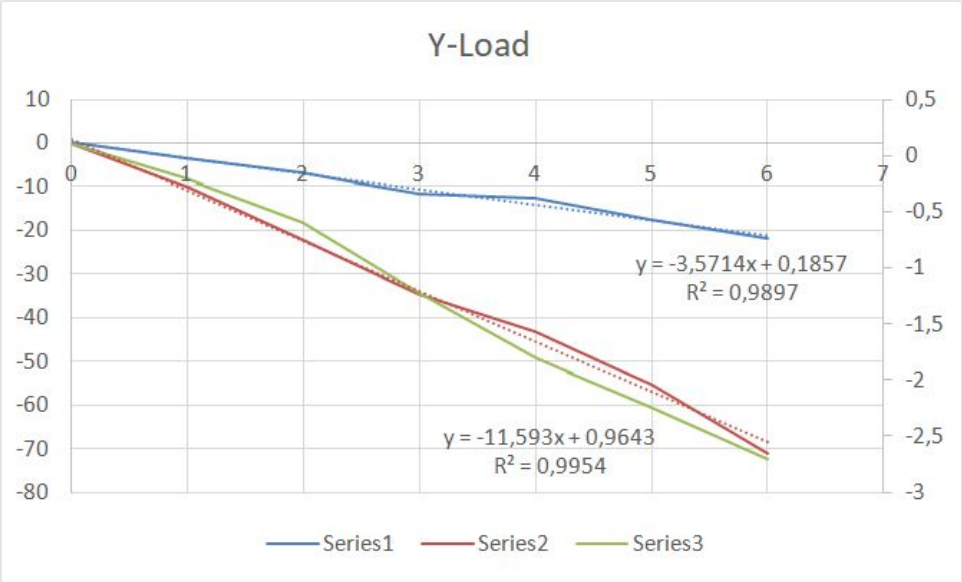

Figure C.4: Outputs Under Loading in Y-Direction

Pylon #2

Results of loading in Z-Direction is presented in Figure C.5

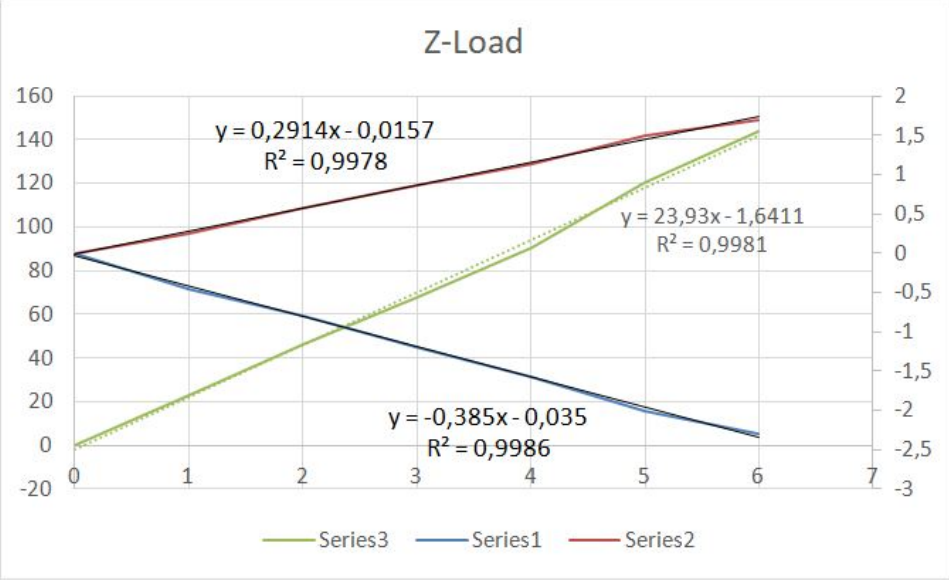

Figure C.5: Outputs Under Loading in Z-Direction

Pylon #3

Results of loading in X-Direction is presented in Figure C.6

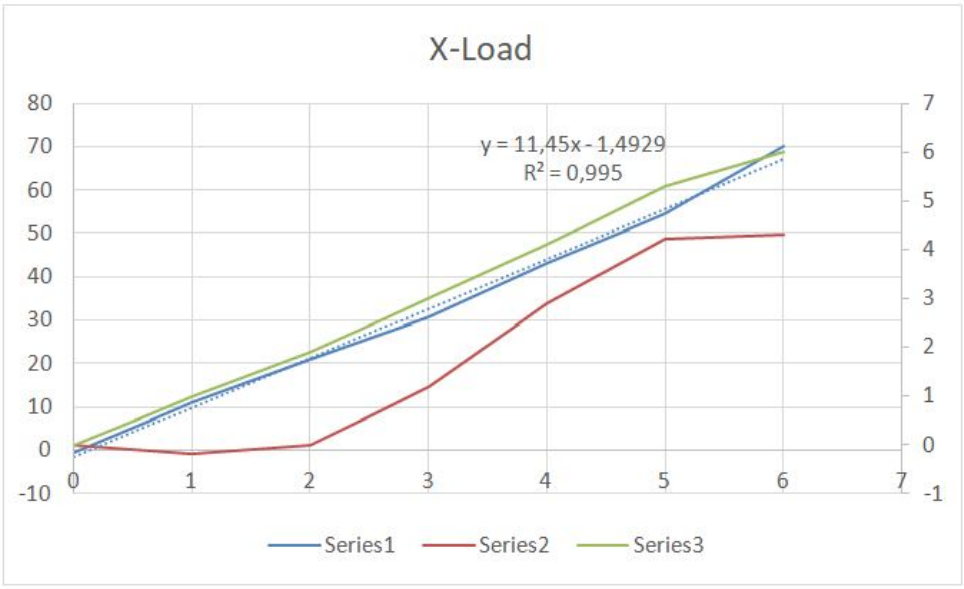

Figure C.6: Outputs Under Loading in X-Direction

Pylon #3

Results of loading in Y-Direction is presented in Figure C.7

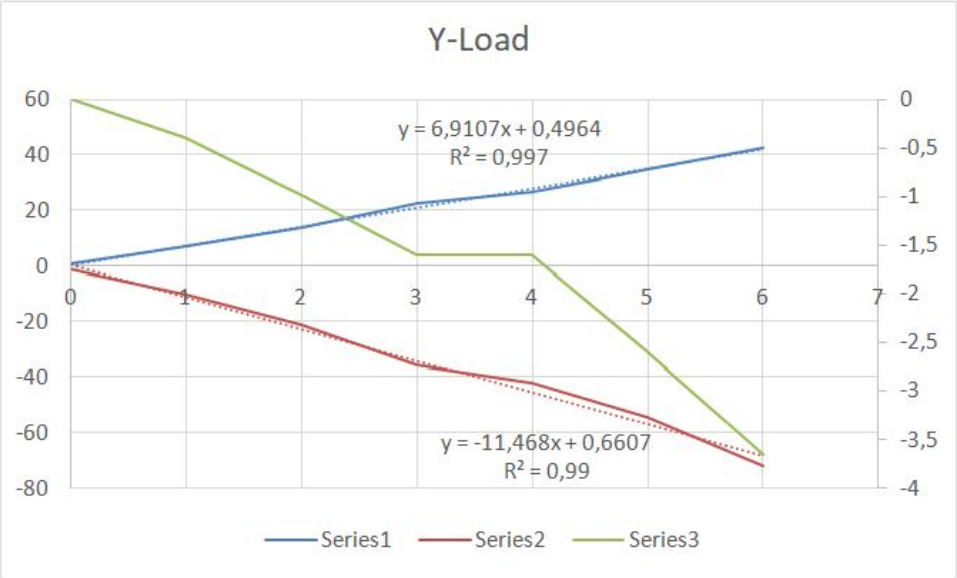

Figure C.7: Outputs Under Loading in Y-Direction

Pylon #3

Results of loading in Z-Direction is presented in Figure C.8

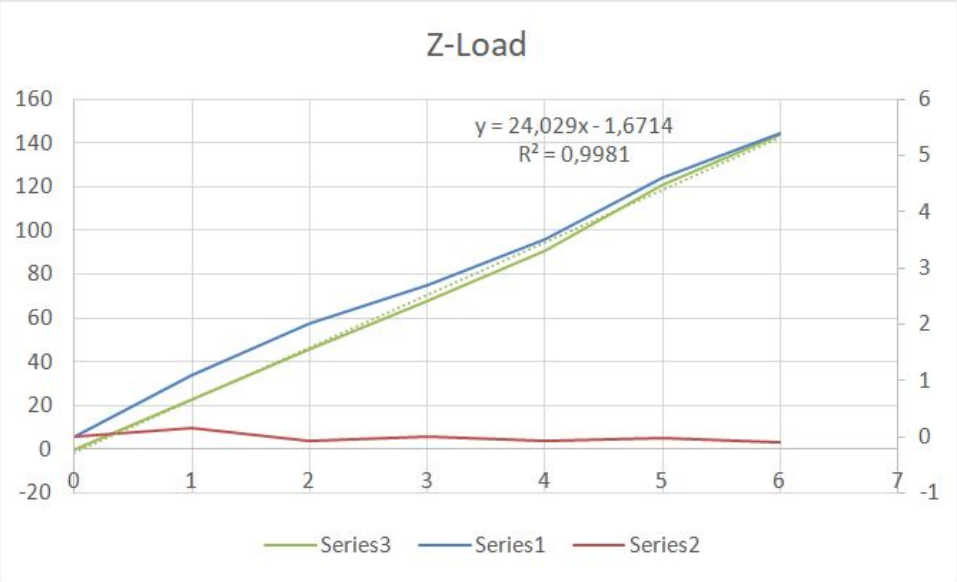

Figure C.8: Outputs Under Loading in Z-Direction

Pylon #4

Results of loading in X-Direction is presented in Figure C.9

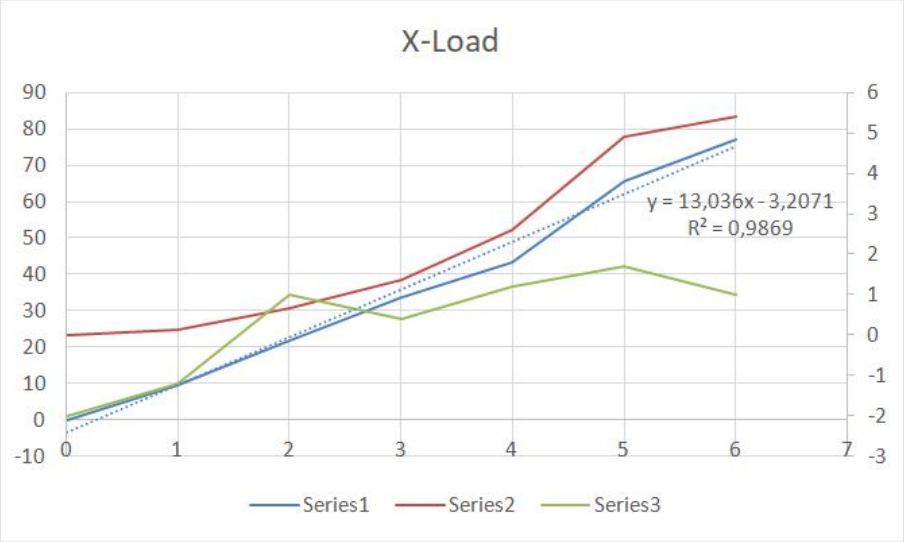

Figure C.9: Outputs Under Loading in X-Direction

Pylon #4

Results of loading in Y-Direction is presented in Figure C.10

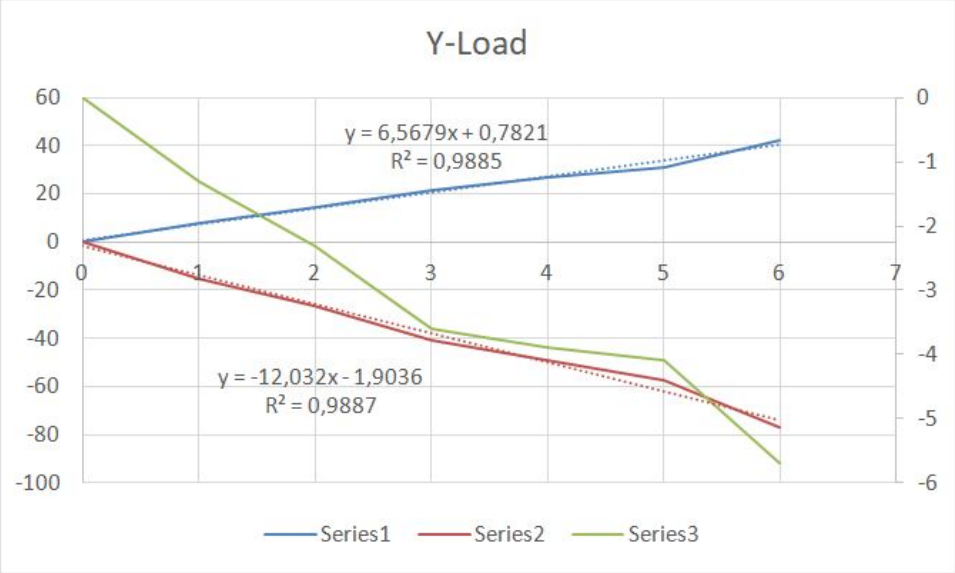

Figure C.10: Outputs Under Loading in Y-Direction

Pylon #4

Results of loading in Z-Direction is presented in Figure C.11

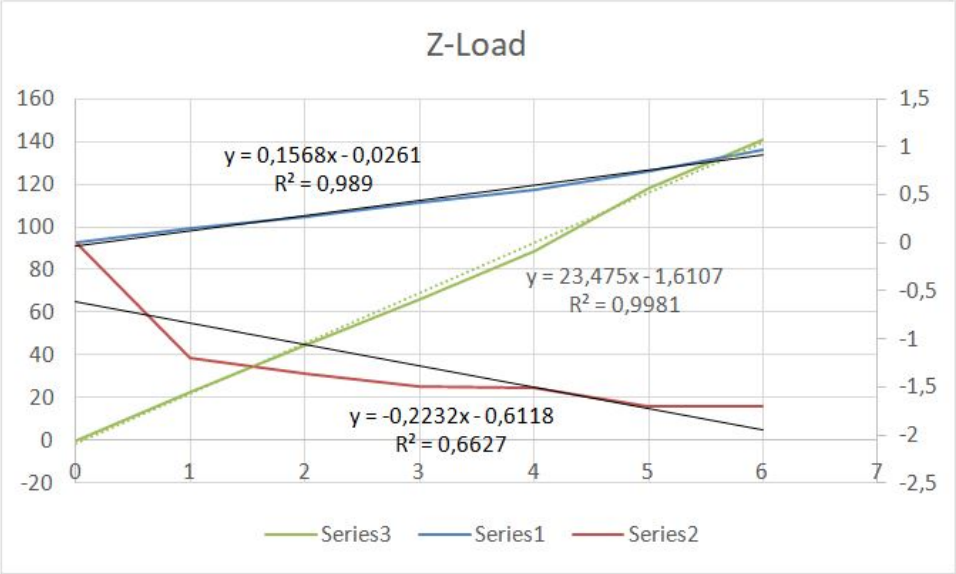

Figure C.11: Outputs Under Loading in Z-Direction

Point #1

Results of loading the platform in Z-Direction at Point-1 is presented in Figure C.12

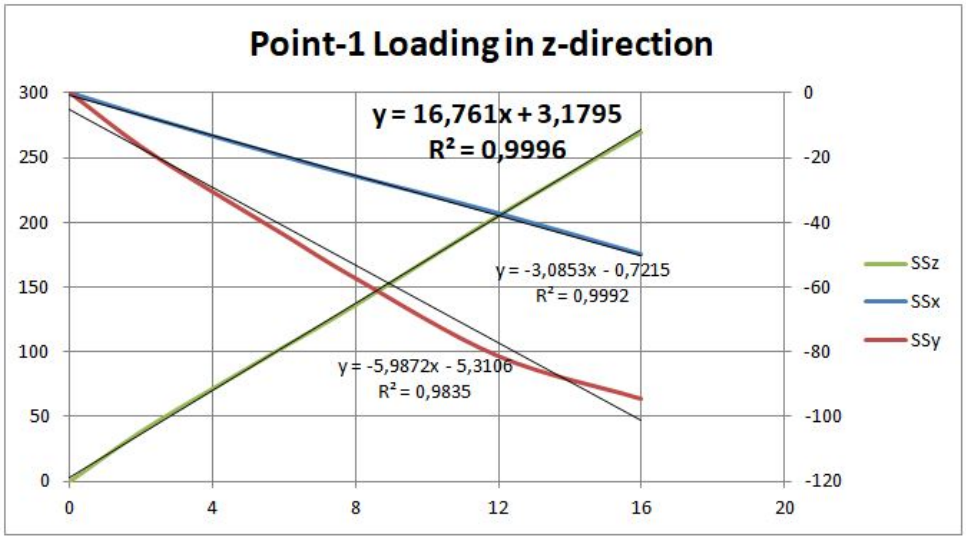

Figure C.12: Outputs Under Platform Loading in Z-Direction

Point #2

Results of loading the platform in Z-Direction at Point-2 is presented in Figure C.13

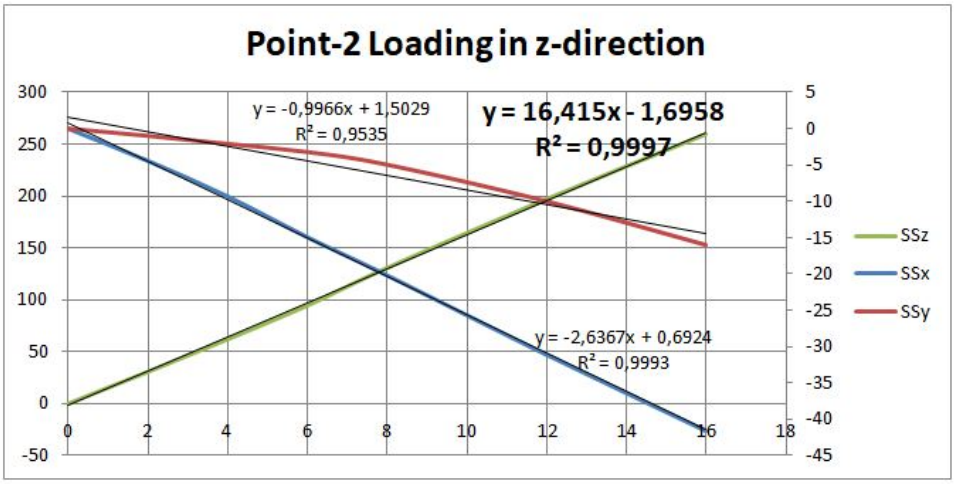

Figure C.13: Outputs Under Platform Loading in Z-Direction

Point #3

Results of loading the platform in Z-Direction at Point-3 is presented in Figure

C.14

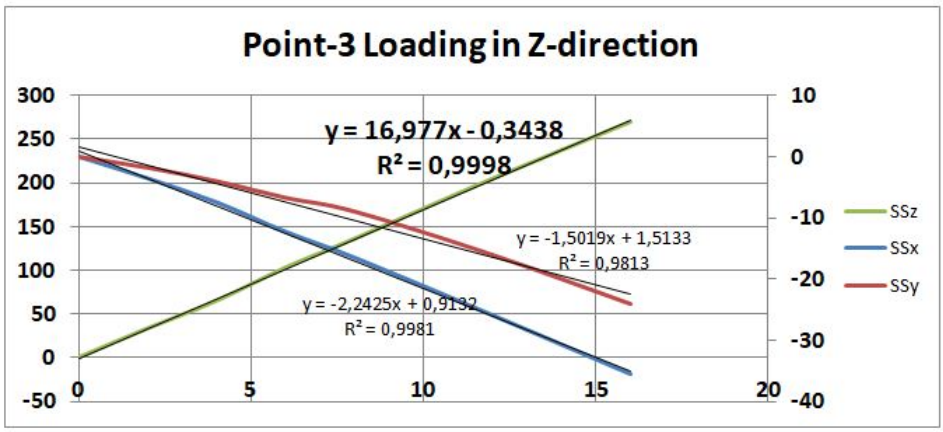

Figure C.14: Outputs Under Platform Loading in Z-Direction

Point #4

Results of loading the platform in Z-Direction at Point-4 is presented in Figure C.15

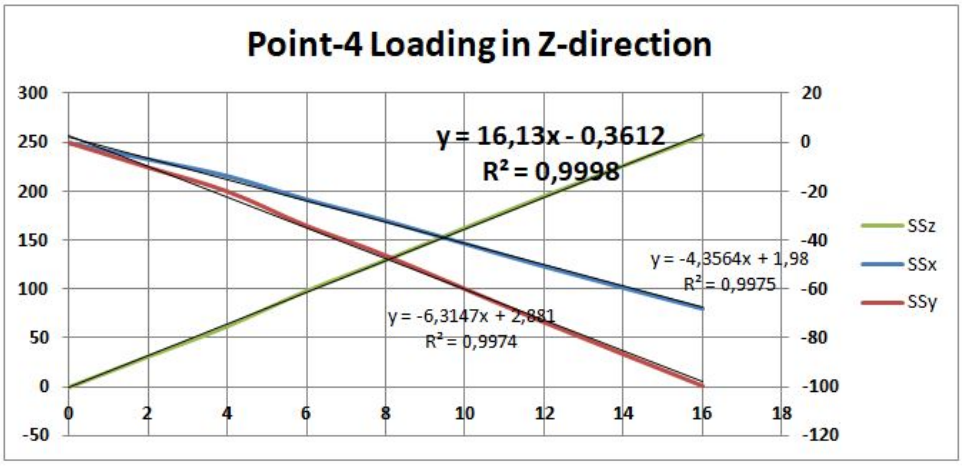

Figure C.15: Outputs Under Platform Loading in Z-Direction

Point #C

Results of loading the platform in Z-Direction at the center is presented in Figure C.16

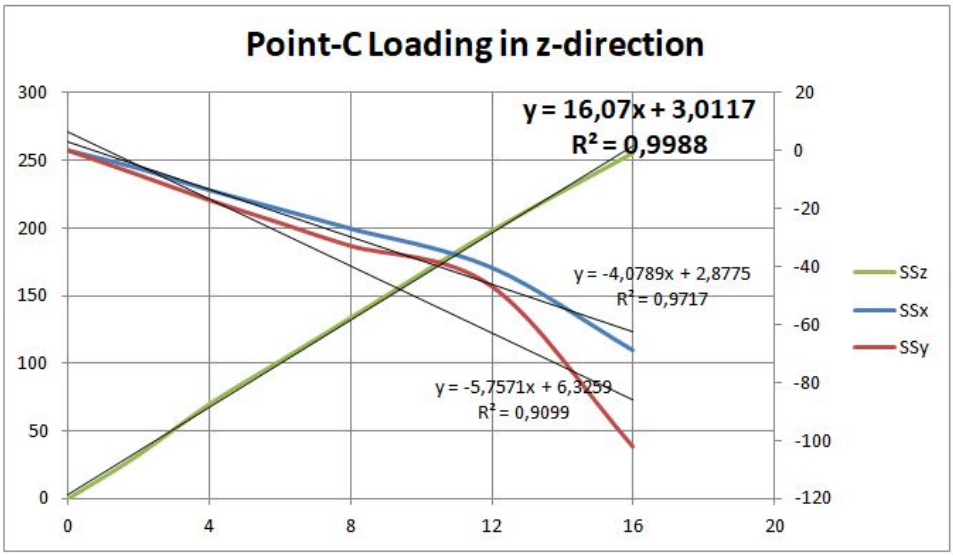

Figure C.16: Outputs Under Platform Loading in Z-Direction

Results of loading the platform in (shear) x-Direction is presented in Figure C.17

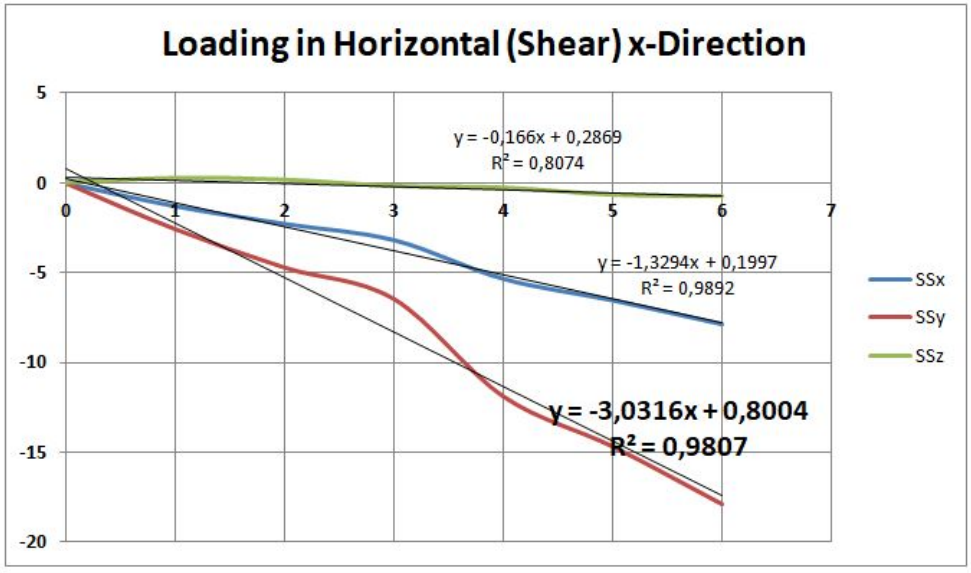

Figure C.17: Outputs Under Platform Loading in Shear X-Direction

Results of loading the platform in (shear) y-Direction is presented in Figure C.18

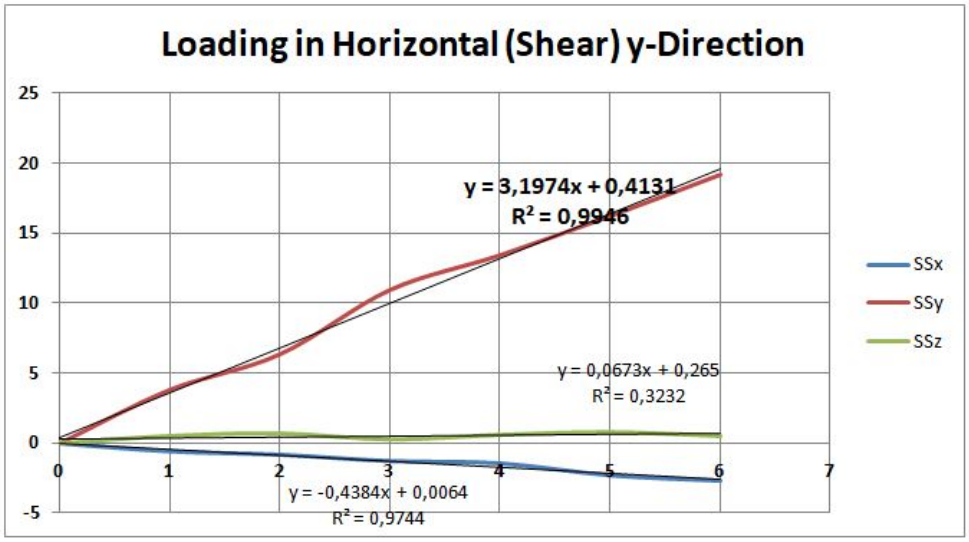

Figure C.18: Outputs Under Platform Loading in Shear y-Direction

Moment measurements at Point #1 under vertical loading is presented in Figure C.19

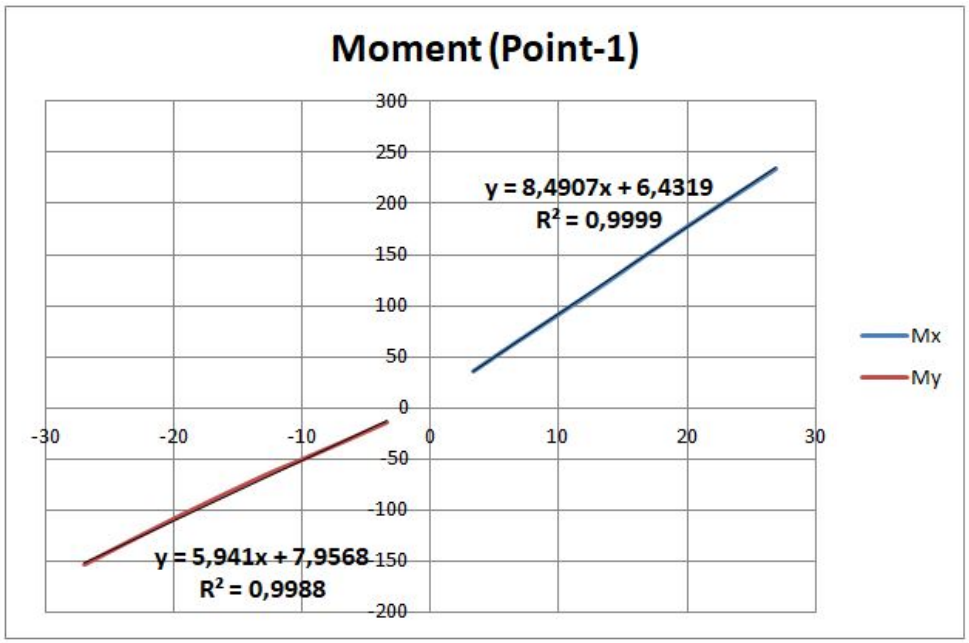

Figure C.19: Moment Output at Point #1

Moment measurements at Point #2 under vertical loading is presented in Figure

C.20

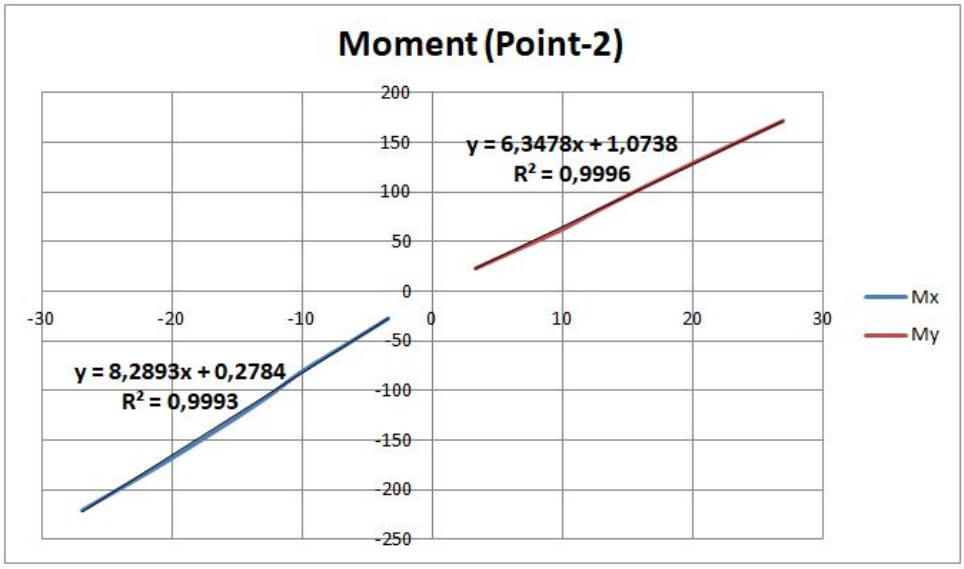

Figure C.20: Moment Output at Point #2

Moment measurements at Point #3 under vertical loading is presented in Figure C.21

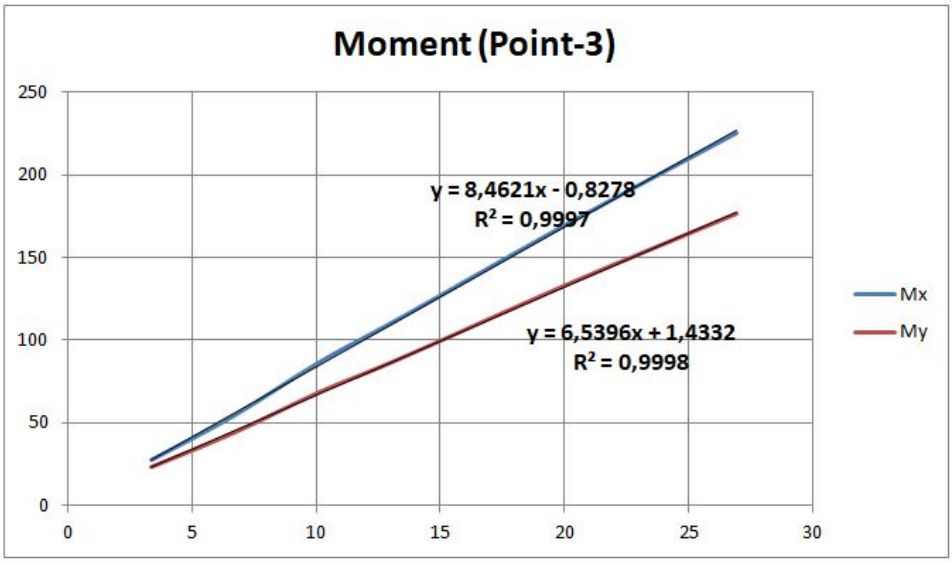

Figure C.21: Moment Output at Point #3

Moment measurements at Point #4 under vertical loading is presented in Figure

C.22

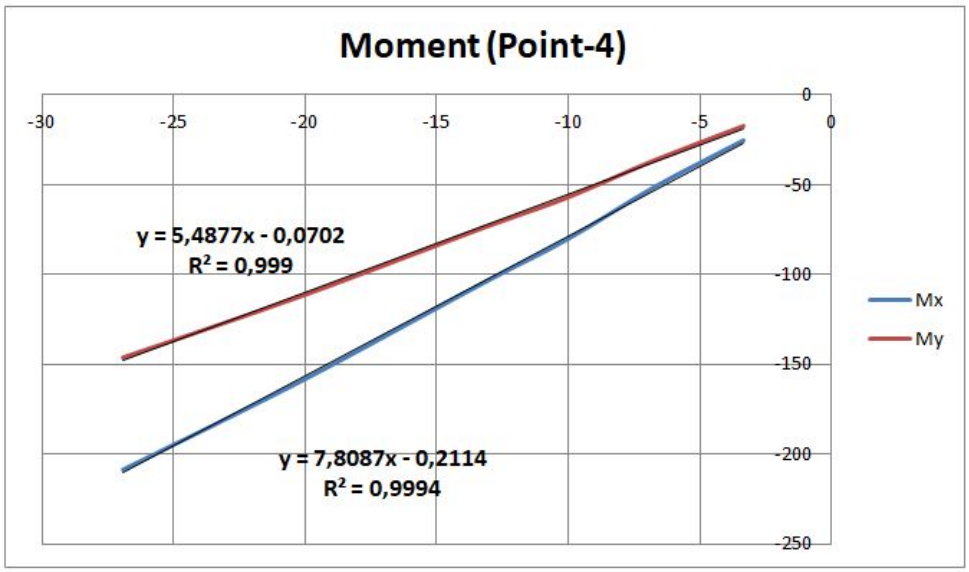

Figure C.22: Moment Output at Point #4